

Preparation of an ultra-cold
sample of ammonia molecules
for precision measurements

Marina Quintero Pérez

**Preparation of an ultra-cold sample of ammonia
molecules for precision measurements**

VRIJE UNIVERSITEIT

**Preparation of an ultra-cold sample of ammonia
molecules for precision measurements**

ACADEMISCH PROEFSCHRIFT

ter verkrijging van de graad Doctor aan
de Vrije Universiteit Amsterdam,
op gezag van de rector magnificus
prof.dr. F. A. van der Duyn Schouten,
in het openbaar te verdedigen
ten overstaan van de promotiecommissie
van de Faculteit der Exacte Wetenschappen
op maandag 8 september 2014 om 11.45 uur
in de aula van de universiteit,
De Boelelaan 1105

door

Marina Quintero Pérez

geboren te Granada, Spanje

promotor: prof.dr. W. M. G. Ubachs
copromotor: dr. H. L. Bethlem

*A mis padres,
por todo.*

This thesis was approved by the members of the reviewing committee:

dr. S. Hoekstra (Rijksuniversiteit Groningen)
prof.dr. A. Osterwalder (École Polytechnique Fédérale de Lausanne)
prof.dr. D.H. Parker (Radboud Universiteit Nijmegen)
prof.dr. F.E. Schreck (Universiteit van Amsterdam)
dr. T.E. Wall (University College London)



The work described in this thesis was carried out in the Institute for Lasers, Life and Biophotonics of the VU University Amsterdam and was supported by the Netherlands Organization for Scientific Research (NWO) via a VIDI grant and by the European Research Council (ERC) via a Starting grant.

The cover of this thesis is based on a watercolor painting of a mosaic of the Alhambra made by M. Quintero Fuentes. Digital design by T.D. Rotteveel and M. Quintero Pérez.

ISBN: 978-94-6259-292-6

Printed by: Ipskamp Drukkers B.V.

Contents

1	Introduction	1
1.1	High-precision measurements	2
1.1.1	Manipulation of neutral molecules	3
1.1.2	Ramsey's method of separated oscillatory fields	4
1.2	Atomic clocks	6
1.2.1	Evaluation of stability and accuracy	6
1.2.2	An atomic fountain clock	8
1.2.3	Optical clocks	11
1.3	A molecular fountain	12
1.4	Manipulation of polar molecules	14
1.4.1	The ammonia molecule	15
1.4.2	The Stark decelerator	17
1.5	Outline of this thesis	21
2	Detecting ammonia using VUV radiation	23
2.1	Introduction to nonlinear optics	23
2.1.1	Frequency mixing in krypton	26
2.2	Experimental setup	27
2.3	Results	29
2.3.1	Pressure dependence	29
2.3.2	1+1' REMPI spectrum of NH ₃	29
2.3.3	Comparing signals	30
2.4	Conclusions	32
3	Velocity Map Imaging of a slow beam of ammonia molecules	35
3.1	Introduction	35
3.2	Experimental setup	36
3.3	Characterizing the ion optics	39
3.4	Experimental results	40
3.5	Conclusions	46

4	Trapping in a traveling wave decelerator	47
4.1	Introduction	47
4.2	Experimental setup	48
4.3	Experimental results	51
4.4	Conclusions	55
5	Characterizing the traveling wave decelerator	57
5.1	Introduction	57
5.2	Experimental setup	58
5.3	Theory	60
5.4	Results	63
5.4.1	Guiding, deceleration and trapping	63
5.4.2	Phase jumps	67
5.4.3	Adiabatic cooling	69
5.5	Conclusions	71
6	Preparing an ultra-cold sample of molecules	73
6.1	Introduction	73
6.2	Experimental Setup	74
6.3	Experimental Results	76
6.4	Conclusion	82
	Bibliography	83
	Publications	93

Chapter 1

Introduction

The cover of this thesis is based on a mosaic located at the Alhambra, a 13th century moorish palace in Granada, the place where I was born and raised. It is inside the walls of this palace where geometric art reached its climax.

When we enter a room in the Alhambra, at first sight, an entire wall decorated with complex geometric figures calls for our attention. As we keep observing, we realize that these figures can be disentangled into smaller and simpler patterns. An even longer observation time is needed to comprehend that these patterns are based on a few simple geometric forms, which constitute the elementary pieces of the puzzle that is the whole design of the wall. Simple geometric figures combined to form interlocking repetitive patterns give rise to a much larger and richer complexity of structures. Therefore, these elementary shapes contain information about any complex design that can be found anywhere in the entire palace.

In Nature, similarly to geometric art, there are also elementary units that form every complex system we know. Atoms and molecules are the tiny pieces that compose the puzzle of the Universe we live in. Each atom and molecule encodes an unimaginable amount of information about how the whole Universe works and has worked since the beginning of times, 13.7 billion years ago. Atomic and molecular physicists deal with how to decipher the information encoded in atomic and molecular structure and dynamics.

For this goal, similarly to the observation of a mosaic in the Alhambra, a greater amount of information is obtained by increasing the time we spend interrogating an atom or molecule in an experiment. This thesis is about obtaining long interrogation times in a molecular beam experiment, in order to collect information as detailed as possible about the structure of molecules. Elongating this time to new limits allows us to interrogate molecules to such a level that questions that were not possible to ask or answer before can now

be addressed; questions about to what extent the fundamental laws of nature hold.

In order to obtain these long interrogation times we use electric fields to manipulate the motion of polar molecules. In the first years of this project, we have tested a scheme for a molecular fountain consisting of a Stark decelerator to decelerate molecules to velocities below 5 m/s, and a combination of two linear and one cylindrical electric quadrupole lenses to cool the molecules as they are launched upwards and focus them as they fall back under gravity. Unfortunately, we were not able to observe a signal of molecules falling back with this setup. This thesis describes our attempts to increase the signal in the fountain by implementing more elaborated detection schemes and by using an alternative design for the decelerator.

The remainder of this chapter starts with an overview of the concept, history and evolution of high-precision measurements. Subsequently, atomic clocks are explained, together with an evaluation of the stability and accuracy reached in these experiments. The merits of a molecular fountain for testing fundamental physics are explained, and a brief introduction is given on Stark deceleration. The chapter ends with a description of the initial scheme of the molecular fountain and the challenges encountered during testing this prototype.

1.1 High-precision measurements

The level of precision of a measurement is inversely proportional to the time that the atom or molecule spends interacting with the radiation that induces a transition between quantum states. Therefore, this time represents the ultimate limitation on the level of precision reached.

High-precision spectroscopic experiments are typically performed similarly to the situation depicted in figure 1.1. Atoms or molecules transit through a cavity that contains the interrogating radiation, and are detected afterwards. Particles in the gas phase at room temperature have a velocity v that is typically of the order of hundreds of meters per second, and the device to produce the desired radiation would typically have a length L of the order of a meter. The interaction time Δt derived from these values, following the relation $\Delta t = L/v$, is of the order of milliseconds. This means that the transition under study would have a linewidth $\Delta\nu$ of the order of kHz, as it is derived from the relation $\Delta\nu \propto 1/\Delta t$ (more details will follow in section 1.1.1). To diminish this width, the interaction time has to be increased. Elongating the dimensions of the device that contains the radiation will increase this time, but it presents technical issues related to the construction of such a cavity, and problems with the homogeneity of the radiation field throughout the device.

These factors will be ultimately translated into errors and overall decrease of the precision of the measurement. Therefore, a more straightforward solution to achieve long interaction times is the production of a very slow sample of atoms or molecules, such that they will spend a long time inside the interrogating device. Fig. 1.1 shows the dependence of the transit time of the particles through the cavity and the linewidth of the corresponding measurement.

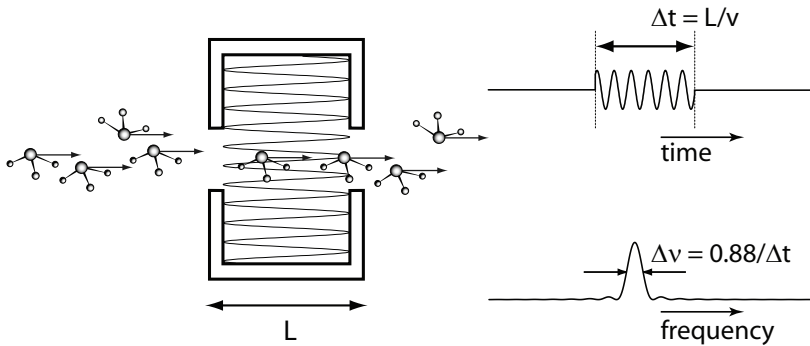


Figure 1.1 – Beam of molecules passing through a device that contains the interrogating radiation. Dependence of the width of the measured transition on the transit time of the molecules through the device.

For an ensemble of particles in equilibrium, temperature and velocity are related through the Maxwell distribution; therefore, referring to the velocity of particles is similar to considering their temperature. In the situations presented in this thesis, it is not completely correct to consider temperature in this strict sense because in most occasions we do not have thermal equilibrium. Furthermore, different temperatures can be associated to each of the degrees of freedom of the atom or molecule. The external degrees of freedom are the three directions in space in which the molecules can move, whereas the internal degrees of freedom refer to their rotation and vibration. In the case of the experiments presented here, the molecules are in a single state, and their internal temperature is zero. Therefore, only the temperature associated with the external degrees of freedom will be considered. The typical temperature of the ammonia molecules in our experiments is in the millikelvin regime.

1.1.1 Manipulation of neutral molecules and the Rabi experiment

The German physicist Otto Stern was the pioneer of manipulating neutral atoms and molecules by using their intrinsic magnetic or electric moments. In 1922, Otto Stern and Walter Gerlach published a paper about the experiment

that they had just performed at the University of Frankfurt [1]. The experiment consisted of the deflection of a beam of neutral silver atoms through the poles of an inhomogeneous magnet. Their results showed that particles possess an intrinsic angular momentum that is closely analogous to the angular momentum of a classically spinning object, but takes only certain quantized values. Stern's student, Isidor Rabi, studied his mentor's technique very carefully and was able to take it a step further. In 1938, he introduced a new way to measure nuclear magnetic moments; the molecular beam resonance method [2, 3]. A molecular-beam resonance setup consists of a beam of molecules traversing two inhomogeneous fields. These fields would be magnetic or electric depending on whether the purpose of the experiment is to study the magnetic or the electric dipole of a molecule. For the general case, a detector is placed on the molecular beam axis, after the molecules have passed the second inhomogeneous field region. The first field will deflect molecules in a particular quantum state in a certain way, and the second field will deflect the molecules in this state in exactly the opposite way, such that they will reach the detector. A typical molecular-beam resonance setup and the trajectories of the molecules through the experiment are depicted in the upper panel of Fig. 1.2. If a small oscillating field region of length L is placed between these two regions, molecules can be excited to another quantum state. If molecules are in a different state, the second inhomogeneous field region will not deflect them back to the detector and these molecules will be lost, resulting in a reduced signal. The amount of signal reaching the detector depends on the frequency of the oscillating field; if this frequency is very close to the molecule's eigenfrequency, the transition will be driven, resulting in signal loss. The function $P_{1 \rightarrow 2}(t, \nu)$ that describes the probability of undergoing the transition from state $|1\rangle$ to $|2\rangle$ is a distribution, the sharpness of which ultimately depends on the interaction time Δt of the molecules with the field in the form $\Delta\nu = 0.88/\Delta t$.

1.1.2 Ramsey's method of separated oscillatory fields

Norman F. Ramsey was a Ph.D. student under Rabi's supervision at Columbia University right at the time when Rabi invented the molecular-beam resonance method. Ramsey started working on a way to make Rabi measurements more precise. He realized that if the molecules, instead of interacting with a single oscillating field for a long period of time, interacted with two short oscillating regions, leaving a free flight time in between, the measurement would be equivalent to a Rabi measurement with an even narrower linewidth. The setup and the trajectory of the particles for a Ramsey experiment are shown in the lower panel of Fig. 1.2.

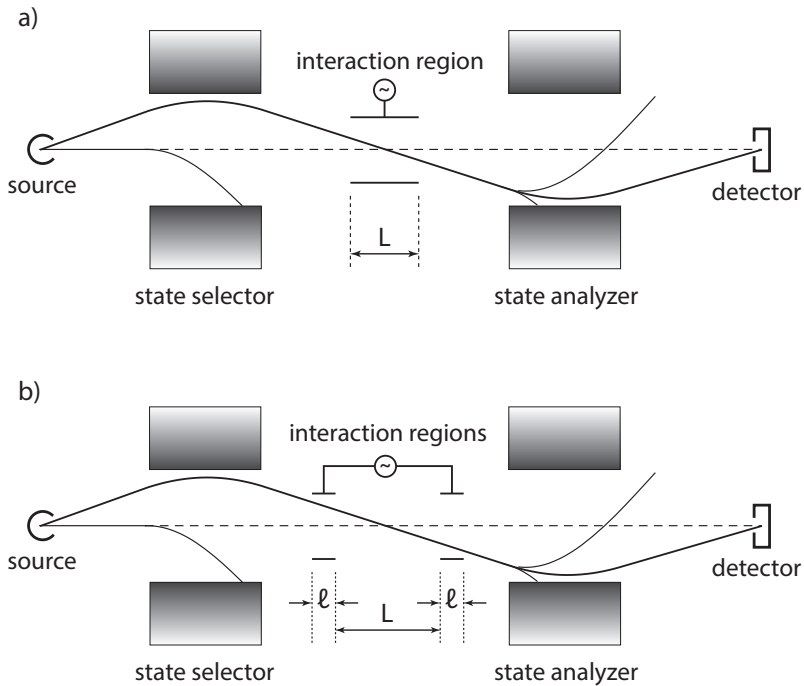


Figure 1.2 – (a) Diagram of a molecular-beam resonance experiment. Particles fly through a first inhomogeneous field that acts as a state selector, deflecting the ones that are in a certain quantum state $|1\rangle$ towards the interaction region. Afterwards, they enter the interaction region L , which contains the interrogating radiation. A second inhomogeneous field acts as a state analyzer, deflecting back to the detector the molecules that have undergone the transition. (b) Diagram for a separate oscillatory field apparatus. The working principle is the same as in (a), the difference being that the interaction region is divided into two small regions l with a field-free region L in between.

A $\pi/2$ pulse is used in the first interaction zone to create an equal superposition of the lower and upper levels. While the molecules are in free flight from the first to the second zone, the phase between the two coefficients that describe the superposition evolves at the transition frequency. In the second interaction zone, this phase is probed using another $\pi/2$ pulse. If the frequency of the interacting radiation is equal to the transition frequency, the second pulse will be in phase with the phase evolution of the superposition and all molecules will end up in the excited state. If the frequency is how-

ever slightly different, the second pulse will be out of phase with the phase evolution of the superposition, and only a fraction of the molecules will end up in the excited state. The so-called Ramsey fringes that appear when the frequency is scanned have a periodicity that is now given by v/L , where L is the distance between the two microwave zones.

As Ramsey states in his Nobel Lecture [4], a Ramsey measurement has several advantages compared to its Rabi counterpart. First of all, a measurement using separated oscillatory fields is less sensitive to non-uniformities of the constant field, since only the space average value along the path is important. Also, the full width at half maximum (FWHM) of the peak measured using Ramsey's method is reduced by 60% compared to the corresponding Rabi peak. Moreover, this method is more effective, and often essential, at very high frequencies where the wavelength of the radiation used is comparable or smaller than the length of the region in which the energy levels are studied.

1.2 Atomic clocks

In 1879, Lord Kelvin suggested that the frequency of an atomic transition could be used to measure time [5]. As opposed to frequency standards based on vibrations of macroscopic objects, atomic frequency standards have the advantage that the frequency-determining objects, e.g., atoms of a particular type are perfectly identical, so that two atomic frequency standards of the same type have the same frequency. The first prototype of this kind of clocks was actually based on molecules rather than on atoms; it consisted of an ammonia maser device built in 1949 at the U.S. the National Bureau of Standards. The accuracy was lower than state-of-the-art quartz clocks, but it served to demonstrate the concept. Nowadays, thanks to the improvement of cooling technologies allowing for the achievement of long interaction times and high densities, atomic clocks are the most precise way to measure time or frequency.

1.2.1 Evaluation of stability and accuracy

A frequency standard is characterized by its stability and its accuracy. The stability is a measure of the statistical uncertainty of a frequency measurement as function of measurement time. The accuracy describes how well the measured frequency agrees with the unperturbed molecular frequency.

Statistical uncertainty

In general, the fractional frequency instability of a clock after a certain measuring time τ is given by the Allan standard deviation $\sigma_y(\tau)$:

$$\sigma_y(\tau) = \frac{1}{Q} \sqrt{\frac{\tau_c}{\tau N}} \quad (1.1)$$

where $Q = \nu_o/\Delta\nu$ is the quality factor of the transition, with ν_o the frequency of the transition and $\Delta\nu \propto 1/\Delta t$ the width of the transition, with Δt being the time the molecules spend interacting with the interrogating radiation*; N is the number of atoms detected per cycle and τ_c is the duration of a cycle. From this formula it is clear that, in order to decrease the Allan deviation and therefore reach high accuracy, it is necessary to elongate the interaction time Δt , but it is as important to have a large number of detected molecules. The number of molecules that can be detected will depend on the density of molecules as well as on their temperature. To combine the density and temperature of an ensemble of particles in a unified property, it is convenient to define the concept of *phase-space density*.

Intermezzo: phase-space density

The phase space of a particle with no internal degrees of freedom is a six-dimensional space defined by the three spatial dimensions $\mathbf{q} := \{x, y, z\}$ and a momentum -or velocity- component in each direction $\mathbf{v}_\mathbf{q} := \{v_x, v_y, v_z\}$. A point in phase-space $\{\mathbf{q}, \mathbf{v}_\mathbf{q}\}$ can be associated with each particle in an ensemble. The number of particles per unit volume in phase space is known as the phase-space density. In quantum mechanics, the phase-space density is defined by the degeneracy parameter of a gas, D :

$$D = n\Lambda^3, \quad \text{with } \Lambda = \left(\frac{2\pi\hbar^2}{mkT}\right)^{1/2} \quad (1.2)$$

where n is the number density, Λ is the thermal de Broglie wavelength, \hbar is the reduced Plank constant, m is the mass of the particles, k is the Boltzmann constant and T the temperature of the ensemble. In the Boltzmann regime (far from quantum degeneracy, $D \ll 1$), the degeneracy parameter is equal to the number of molecules per space and velocity intervals, and thus equivalent to the definition of phase-space density in classical mechanics. In the opposite case, when D becomes of the order unity, the behavior of the system becomes significantly different from the classical one and is characterized by typical

*Note that it is implicitly assumed that the lifetime of the excited state is much longer than the interaction time.

quantum effects, like interference or zero-point energy and motion. A system like this brings up new phenomena unknown in classical statistics, like the observation of a new state of matter known as a Bose-Einstein condensate.

According to Liouville's theorem, the phase-space density is conserved for forces that can be derived from a potential. The experiments presented in this thesis are performed on a supersonic beam of molecules, where there are no collisions, and the forces are exerted by inhomogeneous electric fields. These forces can be derived from a potential, and Liouville's theorem applies [6]. As a consequence, the phase-space density does not change, and lowering the temperature (i.e., the velocity spread) of an ensemble is accomplished by a corresponding decrease in spatial density. This kind of manipulation of the molecules will be referred to as adiabatic cooling. In any spectroscopic experiment that aims for long interaction times, increasing the number of molecules N that will ultimately reach the detector is essential. In our experiments, the optimization of N is done by phase-space manipulation of the molecules.

Systematic effects

While Eq. 1.1 describes the statistical uncertainty, systematic effects have to be taken into account as well to calculate the total uncertainty budget of a measurement. They will contribute to the accuracy of the measurement as shifts, broadening or distortions of the linewidth. Such contributions are, among others, the Doppler shift, black body radiation, the Zeeman and Stark shifts and collisional shifts. They have to be minimized or very accurately measured to be able to reach the desired high precision.

In general, systematic shifts increase with the linewidth of the transition under study [7]. Let us consider two experiments with the same Allan uncertainty value; one of them is based on long interaction times and modest N , and the other is a dense beam of fast molecules, therefore large N but short interaction times. The reason the former is better than the latter for determining frequency shifts is that the systematic effects are more difficult to identify in the case of a broad linewidth. A broader linewidth makes the systematic uncertainties more difficult to estimate because systematic effects are merged or hidden in the line shape, and therefore difficult to disentangle from it. Consequently, a measurement with a narrow linewidth is often more reliable and accurate than a measurement with a broad linewidth, even if Eq. 1.1 predicts the same statistical uncertainty.

1.2.2 An atomic fountain clock

If the velocity of the particles under study is really small, the gravitational pull of the earth will become important. A very elegant way of achieving long

interaction times is to take advantage of this effect by using a fountain configuration. The first attempt to explore the fountain clock idea with cesium atoms was carried out by one of Rabi's colleagues, Jerrold Zacharias, in 1950 [8]. Zacharias' aim was to perform a Ramsey measurement; atoms will fly upwards, interact with the interrogating radiation, and subsequently fall back under gravity, interacting for a second time. A thermal atomic beam directed upwards was used in the experiment. Most atoms in the beam would be too fast to fall under gravity in the atomic beam machine; however, Zacharias concluded that, if the velocity distribution of the atomic beam follows a Maxwell distribution, the number of atoms at very low velocities would be enough to see them falling back.

Unfortunately, the desired selection of the very slowest atoms from the thermal distribution did not work because collisions near the nozzle of the oven practically eliminated this velocity class. Some years after, one of the most efficient methods for cooling atoms, laser cooling, was first proposed [9, 10] and then demonstrated [11, 12]. This process consists of making atoms interact with one or several resonant laser beams. Atoms will undergo many cycles of excitation and consequent relaxation, giving rise to a significant net momentum transfer from the laser beam to the atoms. The invention of laser cooling and trapping techniques allowed for the production of a slow and dense beam of atoms, making possible the achievement of the first cesium fountain clock in 1989 [13]. Fig. 1.3 shows a typical atomic fountain setup. It consists of a gas of cesium atoms that is introduced into the clock's vacuum chamber and six infrared laser beams directed at right angles to each other at the center of the chamber. The lasers will gently push the cesium atoms together, slowing down their movement and cooling them to temperatures near absolute zero. The cloud of atoms is tossed upward by two vertical lasers; after this operation, all of the lasers are turned off. The atoms will fly about a meter high through a microwave-filled cavity and interact with the radiation. Under the influence of gravity, the ball then falls back down through the microwave cavity, interacting with the radiation for a second time. Nowadays, atomic fountain clocks routinely achieve a precision of 10^{-16} [14, 15].

Since 1967, the International System of Units (SI) has defined the second as the duration of 9 192 631 770 cycles of radiation corresponding to the transition between two energy levels of the cesium-133 atom. International Atomic Time (TAI, from the French name *Temps Atomique International*), crucial for modern-day communication and navigation technology, is a weighted average of the time kept by over 200 atomic clocks in over 50 national laboratories worldwide, largely determined by the fountain clocks operated in the US, France, Germany, UK, Switzerland and Japan.

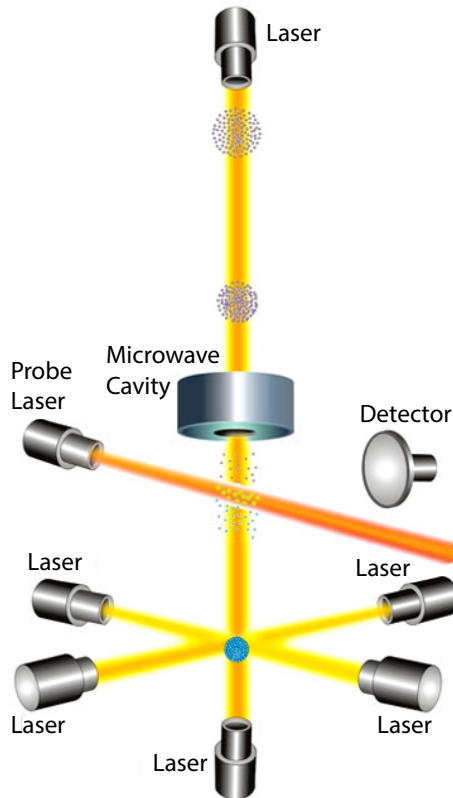


Figure 1.3 – Schematics of the cesium atomic fountain clock. A gas of cesium atoms is introduced into the clock's vacuum chamber. Six infrared laser beams are directed at right angles to each other at the center of the chamber. The lasers gently push the cesium atoms together into a ball. During this process, the lasers slow down the movement of the atoms and cool them to temperatures near absolute zero. Two vertical lasers are used to gently toss the ball upward, and then all of the lasers are turned off. This little push is enough for the atoms to fly about a meter high through a microwave-filled cavity. Under the influence of gravity, the ball then falls back down through the microwave cavity [16].

1.2.3 Optical clocks

Optical transitions are beneficial for use in clocks because they have a high Q factor. Optical clocks are achieved by trapping neutral atoms or ions and making them interact with radiation in the optical range. Methods for trapping atoms and ions have been improving over the years and are now able to reach very low temperatures, high densities and low perturbation of the clock frequency by the trap field, which greatly minimizes the systematic effects and uncertainty of the measured transition.

Atoms can be trapped in different ways. In order to build a clock, a trap method that allows for very low temperatures and high densities is needed. Ultracold (below mK) atoms can be trapped in the focus of a laser whose frequency is far detuned from optical transitions in the atom. Optical excitation can be kept so low that this trap is not limited by light-induced mechanisms. The internal ground-state dynamics can thus be exploited for experiments, and time scales of many seconds are reached. In addition to this, a large variety of trap geometries is possible, like highly anisotropic or multi-well traps. Normally, the two states involved in the clock transition have different ac Stark shifts, and these may be of different signs. This problem introduces a significant dependence of the measured frequency of the clock transition upon the lattice wavelength. To reduce this systematic error, traps are operated at the so-called *magic* wavelength; at this wavelength, the ac stark shift of the levels is the same [17]. Recently, a strontium clock with with accuracy and stability at the 10^{-18} level has been built by Bloom *et al.* [18].

In the same way as atoms, ions can also be trapped by means of electric or magnetic fields and be used for high-precision measurements. The fields in ion traps act on the ions' overall charge and do not significantly perturb their internal structure, reducing systematic effects. The most accurate type of ion clock is the so-called *quantum logic clock*, built for the first time by Rosenband *et al.* [19, 20]. Using electron impact ionization, a single aluminum ion and a single beryllium ion were loaded simultaneously into a linear Paul trap. Aluminum has a transition with an extremely high Q factor but its properties are not easily manipulated or detected with lasers. Both ions were confined on the axis of the trap, coupled by their mutual Coulomb repulsion. This coupling allowed the beryllium ion to sympathetically cool the aluminum ion and also enabled mapping of the aluminum's electronic state onto the beryllium's hyperfine state, which can be measured with high fidelity. Some years later, they described a second, enhanced version of the quantum logic clock based on individual ions of aluminum and magnesium as a more efficient partner ion. With this new setup, the 10^{-18} level was reached [21]. Trapped ions can therefore also provide very accurate high-resolution clocks.

Thanks to the above mentioned techniques, optical clocks based on trapped atoms or ions have recently achieved a better *fractional* accuracy than fountain clocks. This puts aluminum ion or strontium atomic clocks in a position to replace the cesium fountain clock as the standard for time. While the *fractional* accuracy achieved in optical clocks is superior to that of microwave fountain clocks, the latter ones are able to detect a smaller *absolute* frequency shift. For comparison, the aluminum ion clock achieves a fractional accuracy of 8.6×10^{-18} at a frequency of 1.121 PHz, implying an absolute accuracy of around 10 mHz [21]. The cesium fountain clock, on the other hand, achieves a fractional accuracy of 2×10^{-16} at a frequency of 9.192 GHz, implying an absolute accuracy of approximately $2 \mu\text{Hz}$ [14], i.e., 5000 times more precise than the aluminum ion clock. We are interested in measuring small absolute shifts in molecules. Therefore, it makes sense to try to copy the technique that has been most successful in detecting absolute frequency shifts; the microwave fountain clock.

1.3 A molecular fountain

Due to the problems associated with molecules, molecular clocks are unlikely to ever achieve a fractional (or absolute) accuracy that is competitive with those of atomic and ion clocks. Their main virtue lies in the fact that their structure and symmetry makes them very suitable for tests of fundamental interactions that are not possible in atoms (for an extensive discussion on this topic, see for instance [22, 23]). High-precision measurements in molecules are used to search for the electron dipole moment [24, 25, 26], parity violation [27] and the variation of fundamental constants [28, 29, 30]. In the case of the ammonia molecule, NH_3 , the inversion splitting is very sensitive to the variation of the proton-to-electron mass ratio $\mu = m_p/m_e$, and even a small change of this constant would result in a frequency shift that could be detected with an ammonia fountain clock. More detail about the ammonia molecule and its inversion frequency will follow in section 1.4.1.

As was the case in atomic clocks, the Allan standard deviation of a measurement in a fountain configuration (Eq. 1.1) would depend strongly on the interaction time of the measurement and also on the amount of detected particles after the Ramsey process. To minimize this quantity and obtain a high level of precision, two steps are essential: (i) molecules need to be decelerated in order to be able to fall back under gravity, allowing for very long interaction times (in our case, of the order of 0.5 sec); (ii) phase-space manipulation has to be performed in order to obtain a beam of molecules that is cold enough and dense enough that it can undergo a long interaction time while allowing for the detection of a large number of molecules.

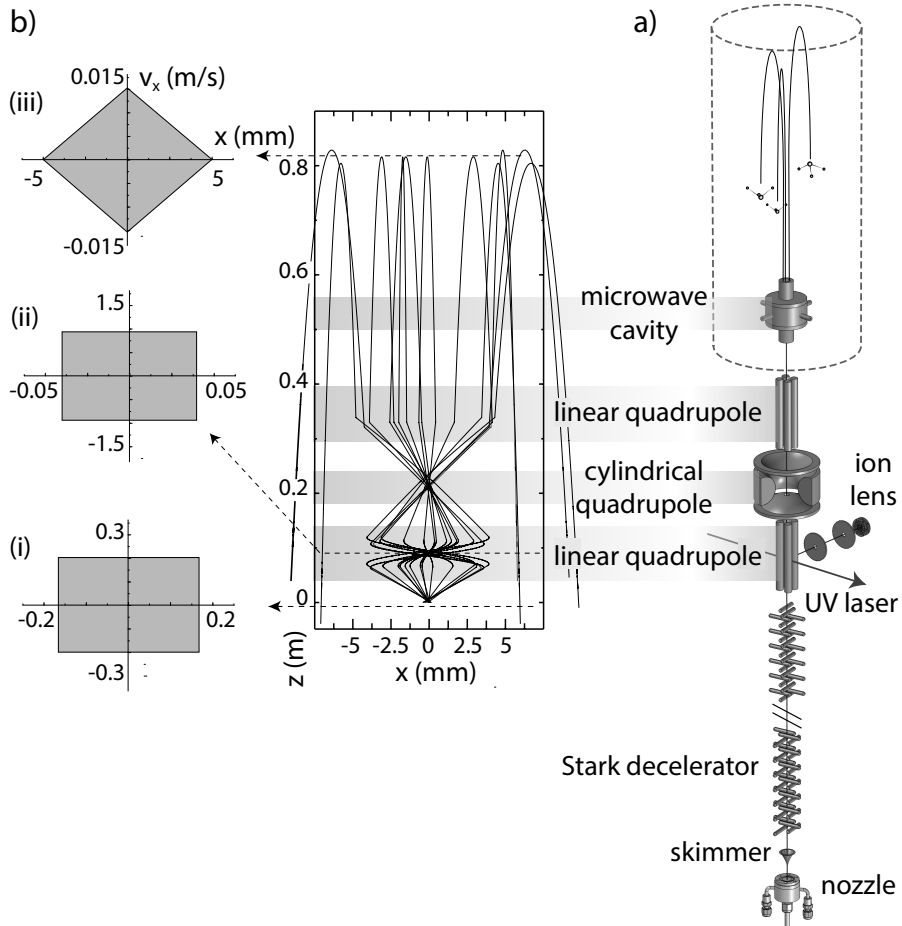


Figure 1.4 – (a) Schematics of a molecular fountain setup. Ammonia molecules seeded in xenon are released from a pulsed supersonic valve (General Valve series 99). Molecules have a velocity of around 300 m/s after undergoing supersonic expansion and subsequently passing through a skimmer. They enter a 101-stages Stark decelerator, where they are decelerated to around 5 m/s in order to be able to fall back under gravity. Two linear quadrupoles for transverse focusing and a cylindrical quadrupole for longitudinal focusing of the molecules are placed after the Stark decelerator in order to keep the density of molecules as high as possible. Molecules will afterwards pass through a microwave cavity that will drive the inversion transition. Subsequently, they will fall back under gravity, crossing the cavity for a second time and being detected. (b) Trajectories of the molecules on the xz plane as they travel through the fountain. The phase-space volume in the transverse plane is plotted on the left for three different situations; (i) after the molecules leave the decelerator, (ii) after focusing on the transverse direction, (iii) after focusing in both directions. Figure adapted from [30].

The experimental challenge of slowing down and manipulating molecules is that, given the complexity of the molecular level structure, laser cooling for most molecular species is either not possible or highly inefficient, even though it has been demonstrated for a few of them [31, 32, 33]. Therefore, other techniques for controlling the internal and external degrees of freedom of molecules have to be developed. In the case of the experiments presented here, deceleration and manipulation of the molecules will be performed with inhomogeneous electric fields.

A Stark decelerator and a series of quadrupole focusing lenses are used to decelerate and focus the molecules into the detection zone. The setup, the trajectories and the phase-space volume of the molecules in each stage of the fountain are shown in Fig. 1.4. In our setup, a mixture of ammonia and xenon expands through a pulsed valve into vacuum. During the expansion, internal energy is converted into forward velocity, resulting in a beam that has a narrow velocity spread centered at around 300 m/s with a low rotational and vibrational temperature. They enter a 101-stages Stark decelerator, where they are decelerated to around 5 m/s to be able to fall back under gravity. In order to keep the density of slow molecules as high as possible throughout the fountain, two linear quadrupoles for transverse focusing and a cylindrical quadrupole for longitudinal focusing are placed on top of the Stark decelerator. After being focused, the molecules pass through a microwave cavity that drives the inversion transition. Subsequently, they fall back under gravity, crossing the cavity for a second time, and they are detected.

Unfortunately, this first prototype of a molecular fountain did not prove efficient enough for keeping a high density of slow molecules, mainly due to large losses of the Stark decelerator at the velocities of interest. The next sections illustrate the working principle of Stark deceleration techniques and give more insight on the issues encountered while developing this molecular fountain scheme.

1.4 Manipulation of polar molecules with electric fields

Polar molecules, due to the asymmetric distribution of the charge over the molecules, have a body-fixed electric dipole moment. The interaction of this dipole moment with an external electric field gives rise to a shift of the energy levels that is known as the Stark effect. As a result of this interaction, a mechanical force acts on a polar molecule when placed in an inhomogeneous electric field. This way, the transverse and longitudinal velocity can be manipulated, similarly to how charged particles are manipulated by means of an electric field in particle accelerators. The difference is that in a charged-particle accelerator the force is a function of the particle's charge and the strength of

the field in the form $\mathbf{F} = q \mathbf{E}$, whereas in the case of polar molecules in inhomogeneous fields the force exerted on the molecules depends on the electric dipole moment of the molecules, μ_{eff} , and on the electric field gradient;

$$\mathbf{F}(\mathbf{r}) = -\nabla W = \mu_{\text{eff}}(|\mathbf{E}|) \nabla |\mathbf{E}(\mathbf{r})| \quad (1.3)$$

where W is the potential energy known as Stark shift. As a consequence, the forces exerted on molecules in inhomogeneous fields are typically eight orders of magnitude smaller than the forces obtained in charged-particle accelerators [34].

1.4.1 The ammonia molecule

Ammonia is the polar molecule that will be the protagonist of our experiments. NH_3 is a classic example of a symmetric top molecule [35]. It has a pyramidal shape, with the three hydrogen atoms forming the base and the nitrogen atom at its apex.

Inversion splitting

Figure 1.5 shows the potential energy of the nitrogen atom in the Coulomb field of the hydrogen atoms as a function of the umbrella angle, which is the angle between the molecular symmetry axis and a line connecting the nitrogen atom with one of the hydrogen atoms. Note that in the Born-Oppenheimer approximation this potential curve is identical for all isotopologues of ammonia. The horizontal lines show the energy of the ν_2 umbrella vibration in the double well. The two minima of the potential correspond to two equilibrium positions, $\rho_1 = 68^\circ$ and $\rho_2 = 112^\circ$. The ammonia molecule usually vibrates in either of the two potential wells around this equilibrium position at a frequency of 950 cm^{-1} . For an infinitely high barrier, tunneling would not be a possibility, and the two lowest vibrational levels would be degenerate; NH_3 at ρ_1 and NH_3 at ρ_2 would be similar to two different molecules in two different potential wells, since a molecule in ρ_1 has no probability of becoming a molecule in ρ_2 . The wavefunctions ψ_{ρ_1} and ψ_{ρ_2} would be eigenfunctions of this system, with identical energies associated. For a finite barrier, however, after some vibrations around ρ_1 the nitrogen atom may tunnel through the plane of the three hydrogen atoms, acquiring the equilibrium position ρ_2 and starting to vibrate around it. In this situation, ψ_{ρ_1} and ψ_{ρ_2} are no longer eigenfunctions of the system and, instead, linear combinations of them $\psi_s = \frac{1}{\sqrt{2}}(\psi_{\rho_1} + \psi_{\rho_2})$ and $\psi_a = \frac{1}{\sqrt{2}}(\psi_{\rho_1} - \psi_{\rho_2})$ have to be chosen. As a consequence, these two eigenfunctions are no longer degenerate in energy, but a splitting between the two energy levels corresponding to the two eigenfunctions arises. The vibronic

ground state is designated as $X(0)$ for the symmetric component and $X(1)$ for the antisymmetric.

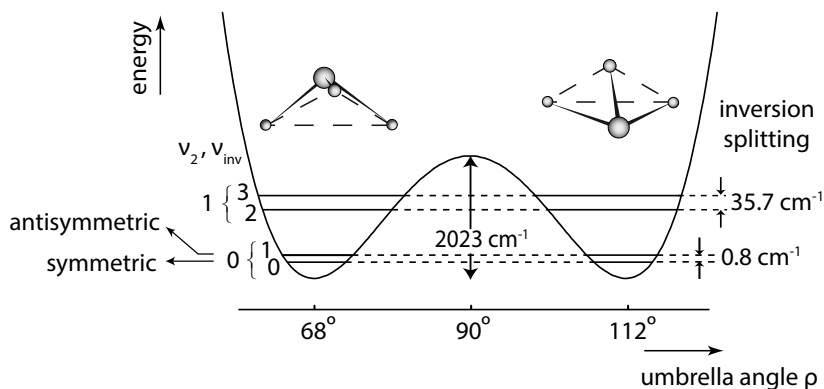


Figure 1.5 – Potential energy of the electronic ground state of ammonia as a function of the umbrella angle. The tunneling effect causes each vibrational level to split into a symmetric and antisymmetric component.

Theoretically, the inversion frequency dependence on the reduced mass m of the molecule follows the formula:

$$\nu_{inv} = \frac{a_0}{\sqrt{m}} e^{-a_1 \sqrt{m}} \quad (1.4)$$

where a_0 and a_1 are constants [36]. The exponential dependence of this frequency with the mass gives rise to a very high sensitivity of this system to variations of the effective mass of the particle that tunnels. As an example, if the hydrogen atoms are replaced by deuterium atoms, which increases the reduced mass by almost a factor of two -as it is the case for ND_3 -, the splitting frequency of ammonia is reduced from 23.8 GHz to 1.56 GHz. This great sensitivity can be used to probe a variation of the proton-to-electron mass ratio, μ , with time; if μ changes with time the effective mass tunneling in ammonia will be different, resulting in a frequency shift. The sensitivity of a given transition to a variation in μ is described by the sensitivity coefficient, K_μ , defined via the expression

$$\frac{\Delta\nu}{\nu} = K_\mu \frac{\Delta\mu}{\mu} \quad (1.5)$$

where $\Delta\nu/\nu$ is the relative shift in frequency of the measured transition and $\Delta\mu/\mu$ is the relative change of the proton-to-electron mass ratio. The calculated sensitivity coefficients to a variation of μ for the inversion frequencies of NH_3 and ND_3 are $K_\mu = -4.2$ and $K_\mu = -5.6$, respectively [30, 37].

The Stark effect in ammonia

As the energy level structure and the Stark shift of ammonia has been extensively studied in many theses and papers [35, 38, 39], here I will only discuss the aspects that are relevant for this work. The rotational structure of NH_3 and ND_3 is best described by the quantum numbers J , the total angular momentum, M , the projection of the total angular momentum on the space-fixed axis, and K , its projection onto the molecular axis. When an ammonia molecule is placed in an inhomogeneous electric field \mathbf{E} , the energy levels undergo a Stark shift W_{Stark} which to first order is given by:

$$W_{Stark} = \pm \sqrt{\left(\frac{W_{inv}}{2}\right)^2 + \left(\mu E \frac{MK}{J(J+1)}\right)^2} \mp \frac{W_{inv}}{2} \quad (1.6)$$

where W_{inv} is the inversion splitting, E is the magnitude of the electric field and μ is the permanent electric dipole moment, which for NH_3 and ND_3 is 1.47 Debye and 1.5 Debye, respectively.

The curves of the energy levels for the two inversion states of NH_3 and ND_3 as a function of electric field strength are shown in the upper panel of Fig. 1.6. Molecules in a quantum state with a negative Stark shift experience a force toward a region of higher electric field and are referred to as high-field seekers (see the case $MK = -1$), while molecules in a state with a positive Stark shift experience a force toward lower electric field regions and are known as low-field seekers (see $MK = 1$). The lower panel of Fig. 1.6 shows the effective dipole moments, μ_{eff} , for the two inversion states of NH_3 and ND_3 . It can be observed that, at a certain value of electric field, μ_{eff} reaches a nearly constant value; from this value onwards, the Stark shift is linear with electric field. As a result of the relatively small inversion splitting of ND_3 , the Stark shift becomes linear for electric field values much smaller than in the case of NH_3 . For NH_3 , the Stark shift depends quadratically on the electric field up to values around 20 kV/cm, becoming linear afterwards.

1.4.2 The Stark decelerator

A Stark decelerator is a device capable of changing the longitudinal velocity of polar molecules while keeping them confined in the transverse directions. It is operated using time-varying electric fields. Stark deceleration was first

demonstrated using metastable CO molecules [40], and since then it has been applied to many other polar molecules [22, 34].

A Stark decelerator consists of an array of pairs of electrodes that will be switched on at positive and negative high voltage (HV) as the molecules approach them (see Fig. 1.7). This generates an area of maximum electric field in the plane of the electrodes, creating a potential energy barrier for low-field-seeking states. Molecules in this quantum state will feel a force towards low electric field areas. Part of the initial kinetic energy of the molecules is transformed into potential Stark energy and the molecule's velocity decreases. The molecule would regain its initial kinetic energy as it leaves the region of high electric field, but this process can be avoided by abruptly switching off the field before the molecule has regained its initial velocity.

While decelerating the molecules longitudinally, transverse focusing is also achieved; since the minimum field in the transverse direction is situated in the middle between two electrodes, low-field seekers feel a force towards the centre. By orienting a decelerating stage orthogonally with respect to the previous one, alternating focusing in the two transverse directions is achieved

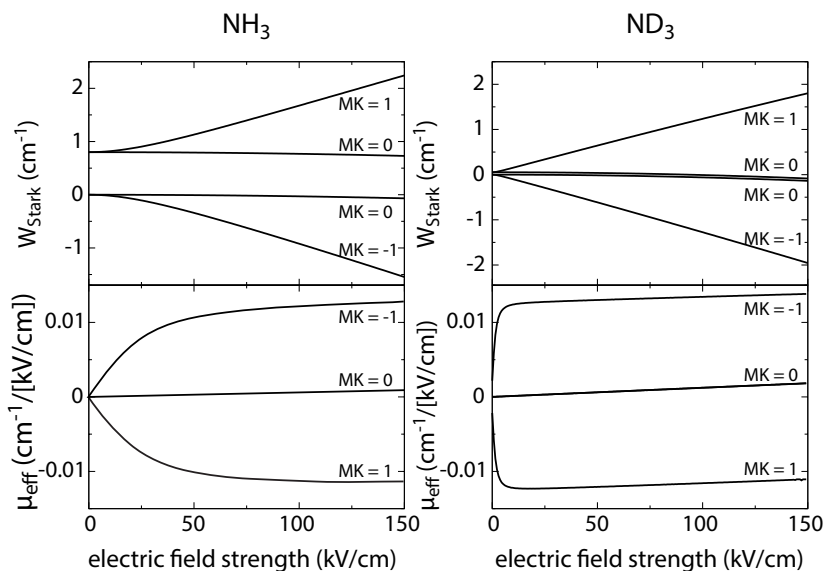


Figure 1.6 – Stark energy level diagrams and effective dipole moments for the $|J, K\rangle = |1, 1\rangle$ state of NH_3 (left-hand side) and ND_3 (right-hand side).

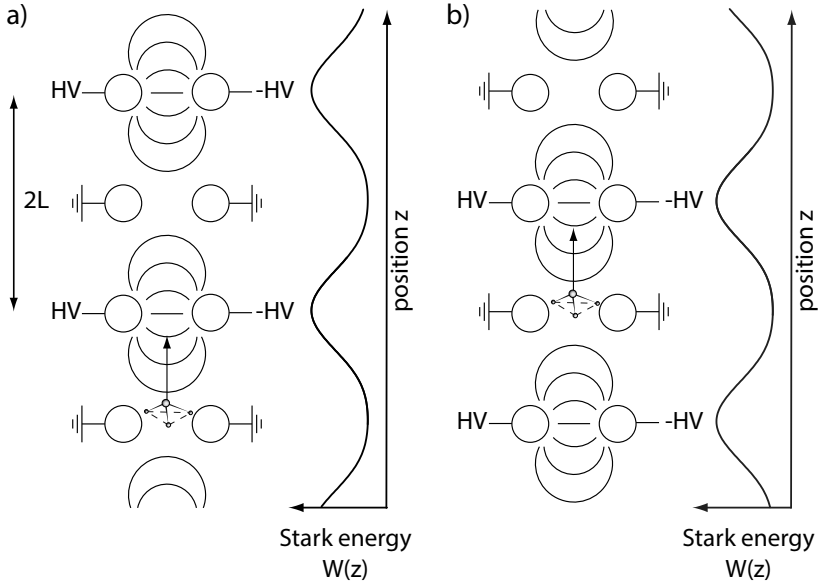


Figure 1.7 – *The operation principle of a Stark decelerator. Molecules lose kinetic energy upon repeated switching between two high-voltage configurations shown in panel (a) and (b).*

(note that in Fig. 1.7 the electrodes are represented on the same orientation for clarity).

In a molecular fountain, molecules with velocities of around 3 m/s are needed in order to be able to fall under gravity and allow for interaction times of the order of a second. According to previous experiments and simulations [41], a Stark decelerator should give a sufficient number of molecules for the fountain experiment. Unfortunately, it was later found that the phase-space density goes down rapidly for velocities lower than 50 m/s.

In Fig. 1.8, the density of molecules at the end of the decelerator was simulated as a function of the final velocity. Each data point is obtained by simulating the trajectories of typically 10^6 molecules with a randomly generated initial position and velocity [39]. It is observed that the number of molecules in the packet as well as its phase-space density drops at low velocities. This decrease is a direct consequence of the fact that the approximations used to

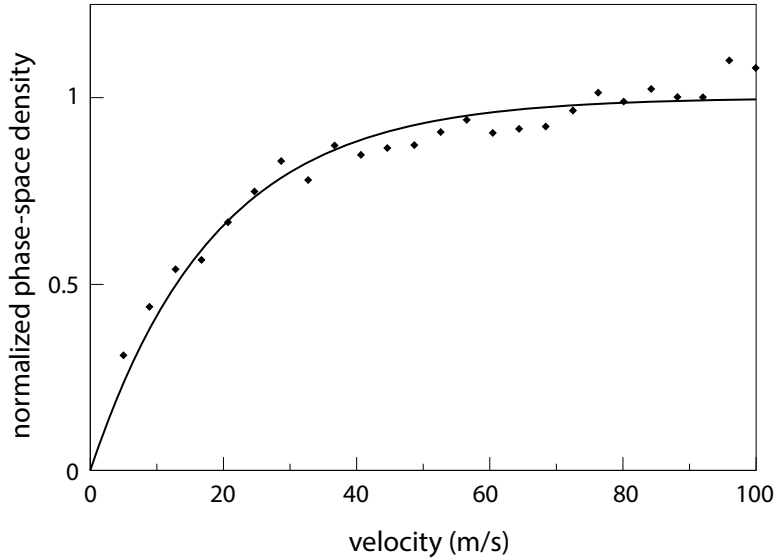


Figure 1.8 – Simulated three-dimensional phase-space density at the end of the decelerator as a function of the final velocity with a constant phase angle $\phi_0 = 60^\circ$. Diamonds represent the normalized number of molecules within a phase-space volume of $1 \text{ mm}^3 (\text{m/s})^3$ around the synchronous molecule. The solid line is intended to guide the eye. Each data point is obtained by simulating the trajectories of typically 10^6 molecules with a randomly generated initial position and velocity [39].

derive *phase stability* [38, 42] are valid at high velocity only, and break down at low velocities, where the characteristic wavelength of the longitudinal and transverse motion of the molecules becomes comparable to the periodicity of the decelerator. For more information about this loss mechanism, see [42]. As a result of this, even though a decent signal of slow molecules could be detected at the first quadrupole (see Fig.1.4), no molecules at the velocities of interest could be detected after the cylindrical quadrupole.

This thesis deals with different methods to compensate for this loss at low velocities, the most important of which is the implementation of an improved kind of Stark decelerator.

1.5 Outline of this thesis

This thesis focuses on the creation and detection of a slow beam of ammonia molecules in a vertical beam machine. If this beam is sufficiently slow and has sufficiently low temperature, ammonia molecules will fly through the experiment with minimum velocity spread, maintaining a density that is high enough and will allow us to detect the molecules after very long times. The long interaction times that could be achieved by a slow and dense molecular beam would make it possible to perform high-resolution spectroscopy.

The following chapters describe three different approaches to improve the signal of slow molecules at the detector; Chapter 2 explores the efficiency of a new detection scheme for the ammonia molecules via $1+1'$ REMPI using VUV light as a substitution of the $2+1$ REMPI detection used until then [39]. Chapter 3 is focused on improving the method for detecting slow molecules. A velocity map imaging lens system is designed to separate fast molecules from slow ones on a CCD camera, therefore reducing the background of fast molecules that contributes to noise on the signal of slow molecules. Chapters 4 and 5 describe the implementation of a new kind of Stark decelerator; a traveling wave decelerator. The traveling wave decelerator is proven to be an improved version of the conventional Stark decelerator, since it avoids the losses that the latter one had at low velocities by creating a true 3D trap that travels with the molecules. The high control over the voltages in the traveling wave decelerator allows not only for efficient deceleration, but also for different techniques of manipulation of molecules, i.e., trapping, adiabatic cooling and characterization of the frequencies of the molecules inside the trap. Results for trapping, cooling and characterization of the trap will be presented. After the experiments described in Chapters 4 and 5, we implemented various improvements to the molecular beam machine, the most notable being the realignment of the traveling wave decelerator and the improvement of its overlap with the conventional Stark decelerator. Thanks to these changes, the number of ions detected in the experiment increases by a factor of 20 and the losses inside the traveling wave decelerator are greatly reduced, allowing us to do a number of experiments that were not possible before. Chapter 6 describes the results of an experiment in which we create an ultra-cold sample of ammonia molecules that is released from the trap and recaptured after a variable time. By performing adiabatic cooling before releasing the molecules and adiabatic re-compression after they are recaptured, we are able to observe molecules even after more than 10 ms of free expansion. A coherent measurement performed during this time will have a statistical uncertainty that decreases approximately as the inverse of the square root of the expansion time. This offers interesting prospects for high-resolution spectroscopy and precision tests of fundamental physics theories.

Chapter 2

Detecting ammonia molecules using vacuum-ultraviolet radiation

In this chapter, a 1+1' Resonantly Enhanced Multi-Photon Ionisation (REMPI) scheme using tunable laser radiation around 160 nm is implemented to detect ammonia molecules. Because of its favorable properties, i.e., large dipole moment, relatively low mass and high vapor pressure, NH_3 [38, 43] and its deuterated isotopologue, ND_3 [41, 44], have been the prototype molecules in Stark deceleration and trapping experiments and are also obvious candidates for testing a molecular fountain. So far, detection of ammonia has been performed via the $X \rightarrow \tilde{B}^1E''$ transition using 2+1 REMPI with ultraviolet light around 320 nm (see left panel of Fig. 2.1). As the first step in this scheme requires two photons, it demands the laser beam to be tightly focused, thus limiting the detection volume and the number of molecules that are addressed. Here, we test whether a 1+1' REMPI scheme is a more sensitive detection method for ammonia molecules (see right panel of Fig. 2.1). Since this is a one-photon transition, a much larger volume can be probed. However, this scheme requires vacuum-ultraviolet (VUV) radiation, the production of which is highly inefficient and experimentally challenging. In essence, the question we want to address in this chapter is whether it is more efficient to generate the required frequency to make a one-photon transition or to let the ammonia molecules absorb two UV photons.

2.1 Introduction: Nonlinear optics and frequency mixing

The field of nonlinear optics describes the behavior of light in nonlinear media, that is, media in which the dielectric polarization responds nonlinearly to the electric field of the light. This nonlinearity is normally only observed at

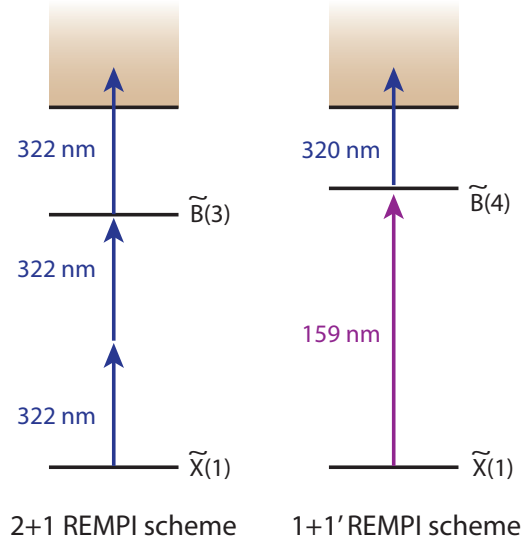


Figure 2.1 – The two different ionization methods employed in this experiment. The 2+1 REMPI scheme used so far requires two UV photons which excite the molecules to the $\tilde{B}(\nu_2 = 3)$ state, plus a third UV photon to ionize them. The new 1+1' REMPI scheme requires a VUV photon to excite the molecules to the $\tilde{B}(\nu_2 = 4)$ state and a UV photon for ionization.

very high intensities of the light (when the electric field of the light is comparable to the interatomic electric fields) such as those provided by pulsed lasers. Therefore, the concept and prospects of harmonic conversion of optical frequencies via nonlinear optical methods started being considered in the years immediately after the invention of the laser. In 1961, Franken *et al.* observed for the first time second harmonic generation of the light of a non-tunable ruby laser using crystalline quartz as the nonlinear medium [45]. In 1967, harmonic generation in gases was demonstrated [46]. This opened the rich field of VUV and XUV (extreme ultra-violet) spectroscopy, based on converted coherent laser radiation. For a review of the subject, see for instance [47].

Let us consider a medium that is irradiated by laser beams, represented by electric field vectors E_i and propagation vectors k_i . In this situation, a polarization \mathbf{P}_i is induced in the medium, which can be expressed as [47]:

$$\mathbf{P}_i = \epsilon_0 \left[\chi_{ij}^{(1)} \mathbf{E}_j + \frac{1}{2} \chi_{ijk}^{(2)} \mathbf{E}_j \mathbf{E}_k + \frac{1}{6} \chi_{ijkl}^{(3)} \mathbf{E}_j \mathbf{E}_k \mathbf{E}_l + O(E^4) \right], \quad (2.1)$$

where $\chi^{(1)}$ and $\chi^{(n)}$ are the linear susceptibility and the nonlinear susceptibilities of the medium respectively, which are properties of the material the medium is composed of. For a medium with inversion symmetry, such as an ensemble of gaseous particles, the even orders in the nonlinear polarization cancel and hence $\chi^{(2n)} = 0$ for integer n . The nonlinear susceptibilities $\chi^{(n)}$ depend on the frequency of the incoming fields and the generated light. For the production of VUV radiation with nanosecond pulsed lasers, which will be the case considered here, the third-order nonlinear susceptibility $\chi^{(3)}$ is the dominant term. Therefore, only this term will be taken into account in the following discussion.

The different aspects of the conversion process, i.e., the conversion efficiency, resonance enhancement effects, dependence on the focusing conditions, gas densities and polarization properties are related to two aspects of wave mixing. First of all, the phase matching; ensuring that a proper phase relationship between the interacting waves is maintained along the propagation direction for optimum nonlinear frequency conversion. Phase matching depends on the indices of refraction, dispersion properties and the geometry and focusing conditions of the three laser beams. Secondly, the microscopic (material) properties of the medium, information contained in $\chi^{(3)}$. The nonlinear polarization induced in the medium for the specific case described above is given by [47]:

$$\mathbf{P}_i^{(3)} = \chi_{ijkl}^{(3)} \mathbf{E}_j \mathbf{E}_k \mathbf{E}_l \quad (2.2)$$

Several wave-mixing processes can be considered. All the processes involving $\chi^{(3)}$ are known as *four-wave mixing*, which is one of the most commonly used frequency-mixing schemes. Noble gases (Xe, Ar, Kr and Ne) are generally employed as the nonlinear media because they have an appropriate level-structure and are experimentally convenient. The four possible wave-mixing processes in this case are:

$$\text{sum frequency mixing} \quad \omega_4 = \omega_1 + \omega_2 + \omega_3 \quad (2.3)$$

$$\text{sum-difference frequency mixing} \quad \omega_4 = \omega_1 + \omega_2 - \omega_3 \quad (2.4)$$

$$\text{difference frequency mixing} \quad \omega_4 = \omega_1 - \omega_2 - \omega_3 \quad (2.5)$$

2.1.1 Resonantly enhanced sum-difference frequency mixing in krypton

Sum-difference frequency mixing schemes allow for a widely tunable VUV output because the wave-vector mismatch, $\Delta k = k_{\text{VUV}} - (2k_R - k_T)$ -where k_T and k_R are the tunable and resonant light wave vectors, respectively-, has no restrictions on the sign for achieving optimal phase matching. Unfortunately, non-resonant sum-difference mixing schemes have low conversion efficiencies, typically in the range $\eta = 10^{-5} - 10^{-6}$ for input powers of 1–5 MW. A large enhancement of the conversion efficiencies can be obtained if the sum frequencies can be tuned to a two-photon resonance of the nonlinear medium used for conversion. This has been demonstrated using xenon [48] and krypton [49, 50], achieving conversion efficiencies of the order of 10^{-4} for input powers of a few hundred kilowatts.

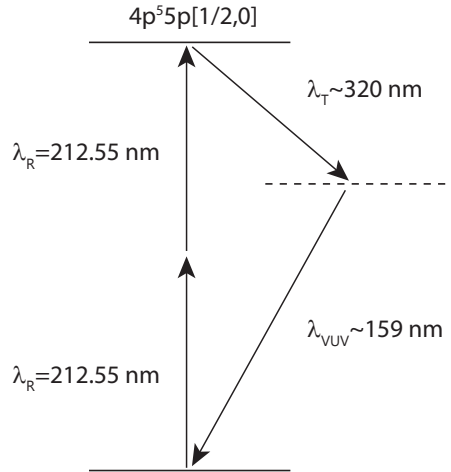


Figure 2.2 – The conversion scheme used in our experiment. To generate VUV radiation via sum-difference frequency mixing, krypton gas is used as a nonlinear medium and the sum-frequencies are tuned to the very strong two-photon transition $4p - 5p[1/2, 0]$, at $\lambda_R = 212.5 \text{ nm}$. The tunable light λ_T used is around 320 nm . In this way $\lambda_{\text{VUV}} \sim 159 \text{ nm}$ is generated.

In the experiment presented in this chapter, krypton is used as a nonlinear medium and, similarly to the experiment realized by Marangos *et al.* [50], the sum-frequencies are tuned to a very strong two-photon transition,

$4p - 5p[1/2, 0]$, at $\lambda_R = 212.5$ nm. The conversion scheme is shown in Fig. 2.2. To produce the necessary wavelengths for this process, two dye lasers running at around 640 nm are required, which is specially convenient for us since we already use this wavelength in the usual 2+1 REMPI scheme. Note that, if λ_R was tuned to the exact value of the krypton resonance, an excessive production of krypton ions might generate a plasma, which would partially destroy the VUV beam [48]. To avoid this effect, in our experiment we set λ_R slightly out of resonance, with a blue detuning of around 0.003 nm.

The sum-difference frequency mixing process that takes place to produce the VUV radiation is given by:

$$\omega_{\text{VUV}} = 2\omega_R - \omega_T, \quad (2.6)$$

where ω_{VUV} is the frequency of the VUV radiation, ω_R is the frequency of the UV light that is resonant with the two-photon transition in krypton and ω_T is the frequency of a tunable UV laser. The power of the VUV radiation produced in the krypton cell in this case can be expressed as [50]:

$$P_{\text{VUV}} \propto P_R^2 P_T N^2 \chi^2 F \quad (2.7)$$

where P_R and P_T are the powers of the resonant and tunable radiation respectively, N is the number density of atoms and χ is the third-order nonlinear susceptibility described in 2.1. F is the dimensionless phase-matching function, which is given by:

$$F(b_R) \propto \exp(-\alpha b_R \Delta k) \quad (2.8)$$

Here, Δk is the wave-vector mismatch, b_R is the confocal parameter of the resonant beam and α is a number close to unity [50]. The focusing conditions also play a role in the final expression of F . Equation 2.8 gives the dependence of F for a Gaussian beam in the tight-focusing limit [50].

If the phase mismatch per krypton atom is defined as $C = \Delta k/N$, the generated VUV power is given by:

$$P_{\text{VUV}} \propto N^2 \exp(-\alpha b_R C N) \quad (2.9)$$

This function has a maximum when the number of krypton atoms fulfill the condition $N = \frac{2}{b_R C}$. Therefore, by modifying the gas pressure to achieve the optimal N , the output of VUV light can be maximized for any given b_R [50].

2.2 Experimental setup

In this experiment, ammonia molecules are produced in our vertical beam machine and guided at 300 m/s through the Stark decelerator. After exiting the

decelerator, the molecular beam passes through the quadrupoles, where it is crossed with the VUV and UV laser beams that will ionize the molecules. The ions are extracted by applying a voltage of +500 V to two of the quadrupole rods and 0 V to the two remaining rods. A time-of-flight setup with a micro-channel plate allows for mass selection of the ions.

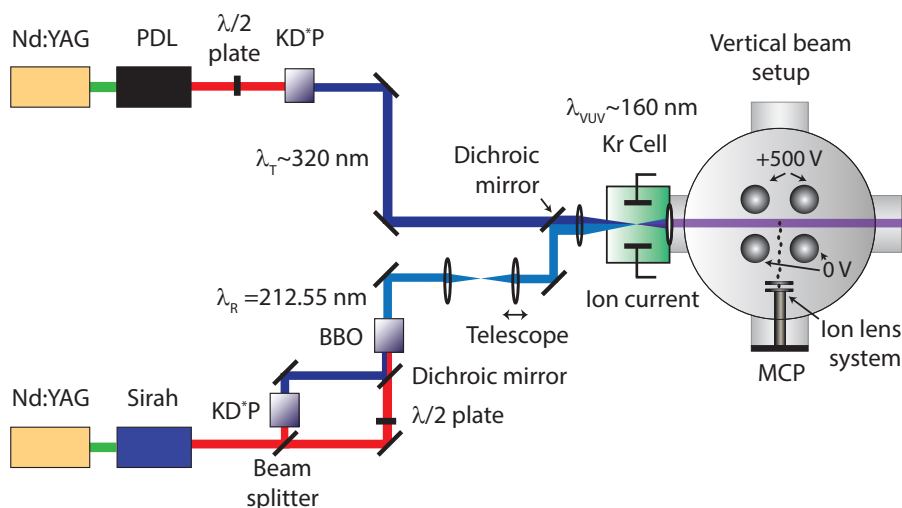


Figure 2.3 – Setup used for the production of VUV light. A laser beam resonant with the $4p - 5p[1/2, 0]$ two-photon transition in krypton is produced by doubling the frequency of the light of a Sirah Cobra pulsed dye laser in a KD*P crystal and subsequently passing it through a BBO crystal, where the fundamental and the double modes mix and generate $\lambda_R = 212.5 \text{ nm}$. A tunable light beam, $\lambda_T \sim 320 \text{ nm}$, is produced by doubling the light of a pulsed dye laser (PDL3, Spectra Physics) in a KD*P crystal. The foci of both laser beams are spatially and temporally overlaid in a cell filled with krypton gas, where the four-wave mixing takes place. VUV light, $\lambda_{\text{VUV}} = 159 \text{ nm}$, is produced, being afterwards directed through our vertical molecular beam machine, where it ionizes the ammonia molecules. Ions are extracted by applying a voltage difference between the rods of the quadrupole and detected on a micro-channel plate (MCP).

The setup constructed for the production of VUV light is shown in Fig. 2.3. The wavelength resonant with the $4p - 5p[1/2, 0]$ two-photon transition in krypton is generated by passing the 637.5 nm light of a Sirah Cobra pulsed dye laser first through a KD*P crystal, where it is doubled, and subsequently

through a BBO crystal. Inside the BBO crystal, the fundamental mode and the second harmonic undergo frequency mixing, generating a laserbeam with $\lambda_R = 212.5$ nm. The tunable light beam, $\lambda_T \sim 320$ nm, is created by doubling the light of a pulsed dye laser in a KD*P crystal. Both light beams are redirected through a cell filled with krypton gas, where the four-wave mixing takes place. A very good and stable overlap between the two laser foci is essential for optimal VUV production. For this, both beams are carefully aligned through the cell to make sure they are co-propagating and a movable telescope is implemented in one of the beams such that the overlap of the two UV foci can be optimized. In order to make sure that the laser wavelength is resonant with the two-photon transition in krypton, the number of ions produced in the krypton cell is monitored. VUV light with a wavelength of around 160 nm is produced in the cell and subsequently enters the vertical beam machine through a CaF₂ lens (a material transparent to light in this wavelength region). The VUV is created very close to the CaF₂ lens to minimize the VUV reabsorption by the krypton gas. The lens has a short focal length, $f = 50$ mm, to ensure that the VUV beam that enters the machine is nearly collimated. The beam waist at the detection zone is in the sub-mm range. The UV used for the ionization step enters the machine as a slightly divergent beam. Together, the VUV and the 320 nm UV light will excite and ionize the ammonia molecules via 1+1' REMPI. Switching from this VUV scheme to the usual 2+1 REMPI scheme is very easy in this setup, making the comparison between the two detection methods very reliable.

2.3 Results

2.3.1 Pressure dependence

Figure 2.4 shows experimental data for the intensity of the ammonia signal as a function of the pressure in the krypton chamber. The number of ammonia ions detected can be considered proportional to the power of the VUV light. The dashed line fits the points according to Eq. 2.9. It can be observed that the experimental data is in very good correspondence with the expected behavior.

2.3.2 1+1' REMPI spectrum of NH₃

Spectra of NH₃ and ND₃ have been obtained by scanning the wavelength of the PDL laser, thereby varying the tunable UV wavelength λ_T . In Fig. 2.5, 1+1' REMPI spectra of NH₃ and ND₃ are shown in the upper and lower panels, respectively. Both spectra are shown with the same intensity scale, and are averaged over 20 shots. The \tilde{B}^1E'' , $\nu_2 = 4$ level is used as an intermediate (see right panel of Fig. 2.1). Via this level, only molecules in the up-

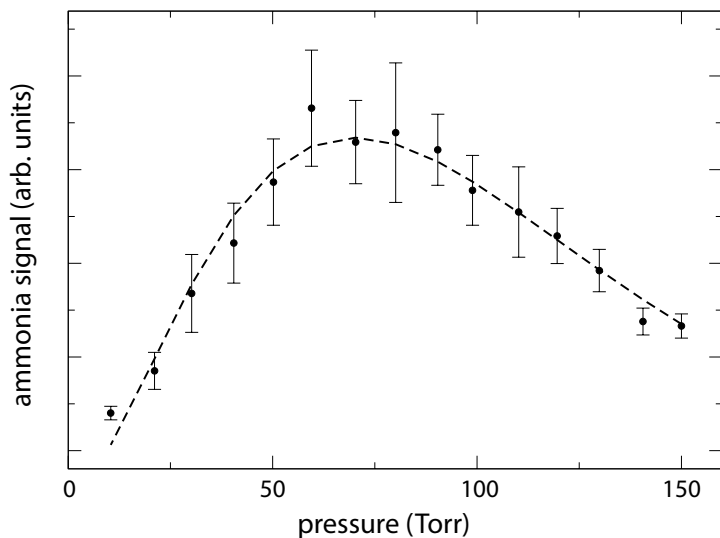


Figure 2.4 – Dependence of the intensity of the signal detected with the pressure of the krypton chamber. The points correspond to number of ions detected for different values of the pressure inside the krypton chamber. Note that the signal intensity can be considered proportional to the power of VUV light. The dashed line is a fit following the expression $P_{\text{VUV}} \propto N^2 \exp(-\alpha b_R C N)$, where N is the number of krypton atoms.

per inversion doublet level (vibrational a symmetry) in the electronic and vibrational ground state are detected. The $|JK\rangle$ rotational quantum numbers of the ground-state levels are indicated in the figure following the notation $\Delta^K \Delta J J_{K''}^{\epsilon''}$ [51].

2.3.3 Comparing signals

Fig. 2.6 shows two spectral lines. The blue curve represents the strongest line we can measure via the usual 2+1 REMPI scheme, and the red one is the signal obtained with 1+1' REMPI under optimal conditions. It can be observed, first of all, that the amplitude of both signals is similar, the two-photon transition being slightly better.

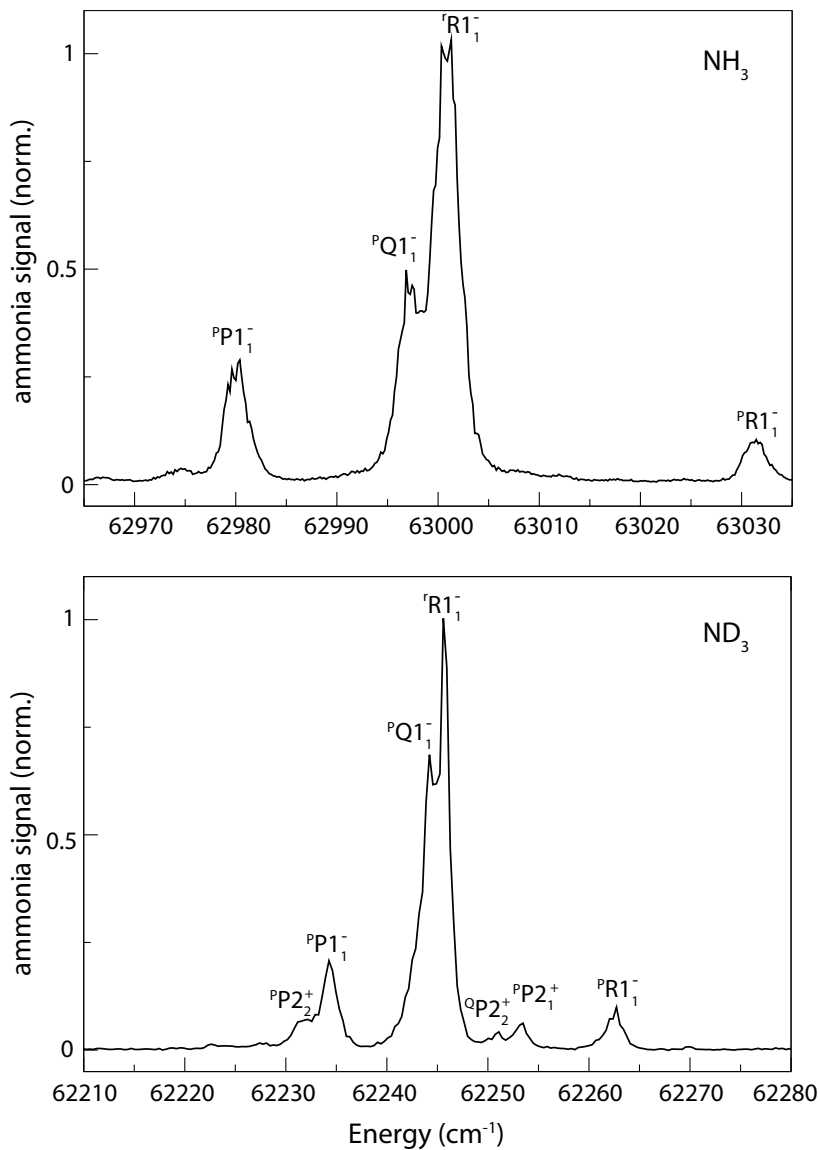


Figure 2.5 – $1+1'$ REMPI spectra recorded via the $\tilde{\text{B}}^1\text{E}''$, $\nu_2 = 4$ state in NH_3 (upper pannel) and ND_3 (lower pannel). The peaks are labeled according to the notation $\Delta K \Delta J J'' \epsilon'' K''$.

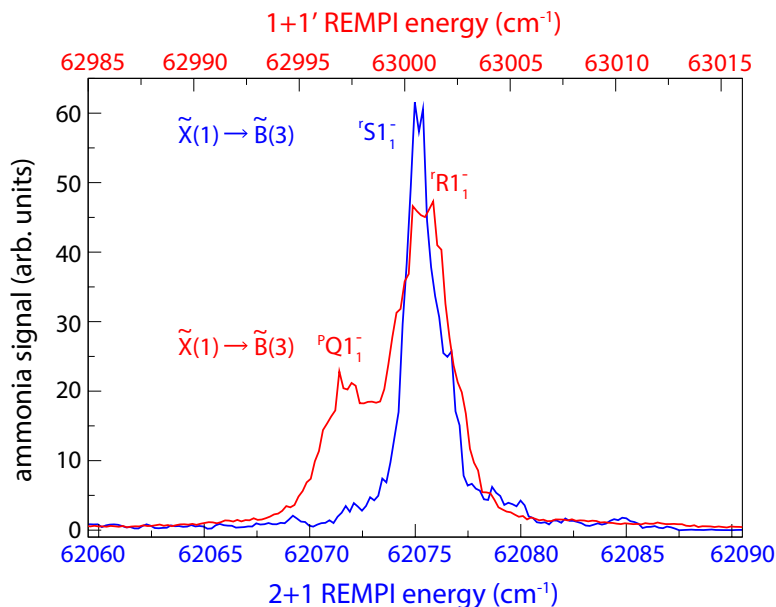


Figure 2.6 – Comparison between the most intense part of the NH_3 spectrum obtained via the usual 2+1 REMPI scheme (in blue) and the 1+1' REMPI scheme (in red).

2.4 Conclusions

In this chapter, we investigated a 1+1' REMPI scheme using VUV to detect ammonia molecules, and compared the detection efficiency of this scheme to the commonly used 2+1 REMPI scheme with UV light. The VUV was produced by four wave mixing in krypton gas taking advantage of the strong 2-photon transition at 212 nm, which is known to be the most efficient method for obtaining tunable VUV radiation. We have carefully optimized the overlap and the focal properties of the laser beams, the pressure of the krypton gas and the detuning from the krypton resonance. Unfortunately, under optimal conditions the signal resulting from the 1+1' REMPI scheme was of the same magnitude as the signal obtained with the 2+1 REMPI scheme, but not better. A possible explanation for this might be that the ionization step limits the number of detected molecules. In the 2+1 REMPI scheme, ionization occurs by absorbing a third UV photon of the same color. As the laser is already tightly focused to drive the 2-photon transition to the \tilde{B} -state, molecules that are excited to the \tilde{B} -state will be rapidly ionized. In the 1+1' REMPI scheme,

the molecules are excited with VUV light and subsequently ionized by absorbing a UV photon. Hence, it is crucial that the VUV and UV beams overlap properly. Experimentally, we do this by tilting the dichroic mirror in front of the setup and by changing the distance between the lenses of the telescope, thereby changing the alignment and focal properties of the 320 nm light. As the beam profile of the two lasers is far from ideal, the overlap will never be perfect. Another complication is that ammonia in the \tilde{B} -state rapidly pre-dissociates. In order to ionize the ammonia before it pre-dissociates, the intensity of the 320 nm light needs to be substantial. It might be that we find optimal signal when the 320 nm light is focused to a rather small volume, thereby ruining the main advantage offered by the VUV REMPI scheme. Note that, if this explanation is correct, we would expect to see a largely different behavior for NH_3 and ND_3 , since the pre-dissociation rate is much lower in the latter case. Although we did perform measurements with ND_3 , these were done after optimizing the signal of NH_3 . To observe the effect, we would need to optimize the focal properties on ND_3 signal.

The efficiency of the 2+1 REMPI scheme could perhaps be further improved by optimizing the overlap and focal properties of the laser beams at least for ND_3 . Nevertheless, we think these improvements will not result in a radical increase and, since the implementation of the 2+1 REMPI scheme is experimentally much simpler and more stable than that of the 1+1' REMPI scheme, the former is preferable.

Chapter 3

Velocity map imaging of a slow beam of ammonia molecules inside a quadrupole guide*

In this chapter, velocity map imaging inside an electrostatic quadrupole guide is demonstrated. By switching the voltages that are applied to the rods, the quadrupole can be used for guiding Stark-decelerated molecules and for extracting the ions. The extraction field is homogeneous along the axis of the quadrupole, while it defocuses the ions in the direction perpendicular to both the axis of the quadrupole and the axis of the ion optics. To compensate for this astigmatism, a series of planar electrodes with horizontal and vertical slits is used. A velocity resolution of 35 m/s is obtained. It is shown that signal due to thermal background can be eliminated, resulting in the detection of slow molecules with an increased signal-to-noise ratio. As an illustration of the resolving power we have used the velocity map imaging system to characterize the phase-space distribution of a Stark-decelerated ammonia beam.

3.1 Introduction

Techniques to decelerate and cool molecules increase the interaction time in spectroscopic experiments and promise to significantly enhance the precision of a number of experiments aimed at testing fundamental laws of physics [25, 26, 27, 52]. As a proof of principle, high-resolution microwave spectroscopy was carried out on Stark-decelerated molecular beams of ND₃ [37] and OH [53]. In these experiments, an interaction time on the order of a

*Based on M. Quintero-Pérez, P. Jansen, and H. L. Bethlem, *Phys. Chem. Chem. Phys.*, vol. 14, pp. 9630-9635, May 2012.

millisecond was achieved. In Chapter 1 we discussed the construction of a molecular fountain in our laboratory, in order to increase the interaction time further. Unfortunately, due to the limited efficiency of cooling techniques, the increased interaction time comes at the expense of a decreased signal-to-noise ratio. Techniques such as resonance-enhanced multiphoton ionization (REMPI) allow detection of very small numbers of molecules. However, if the signal of the decelerated molecules becomes too small, it will be obscured by the signal of the undecelerated part of the beam.

Here, we use velocity map imaging (VMI) to discriminate the signal of slow molecules from thermal background molecules. VMI is a technique that uses ion lenses to focus laser-produced ions onto a position sensitive ion detector [54]. By setting the voltages of the ion lenses correctly, molecules that have the same initial velocity but a different initial position are focused at the same position on the detector. In this way, all velocity information of the particles involved in the experiment is contained in a single image. Ion imaging techniques, such as VMI, have been used extensively for measuring the velocity of product molecules or atoms following a chemical reaction or the photodissociation of a parent molecule [54, 55, 56]. State-of-the-art velocity map imaging systems achieve a velocity resolution below 10 m/s [57].

The ion optics used in a conventional VMI setup consist of three or more electrodes with circular apertures. In this chapter, we demonstrate velocity map imaging inside an electrostatic quadrupole guide that is mounted directly behind a Stark decelerator. The main advantage of this configuration is that it allows for detection inside the guide, where the density of molecules is relatively high. As our detection scheme relies on multiphoton transitions using a focused laser beam, a high density of molecules is crucial. In our configuration, the ions are extracted from the guide by applying a small positive voltage to two of the quadrupole rods. This results in a field that is homogeneous along the axis of the quadrupole, while it defocuses the ions in the direction perpendicular to both the axis of the quadrupole and the axis of the ion optics. Here, we show how the astigmatism can be compensated by using a series of planar electrodes with horizontal and vertical slits.

3.2 Experimental setup

Our experiments have been performed in the vertical molecular beam machine that is described in Chapter 1. In brief, a pulsed ($\sim 100 \mu\text{s}$) ammonia beam is released into vacuum from a solenoid valve (GeneralValve series 99) at a 10 Hz repetition rate. By cooling the valve housing to -50°C and seeding the ammonia molecules in xenon, the mean velocity of the beam is lowered to 300 m/s. The ammonia beam is decelerated using a Stark decelerator

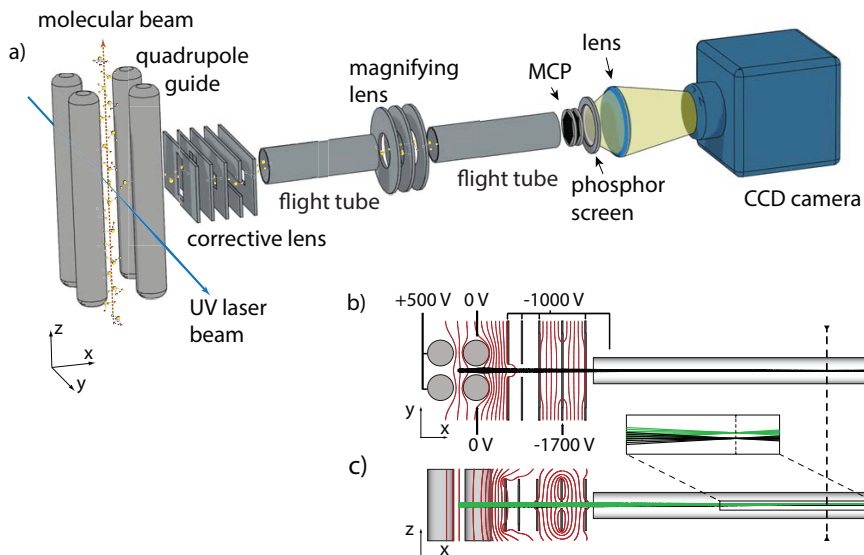


Figure 3.1 – (a) Schematic view of the ion optics used for performing velocity map imaging inside a quadrupole guide. A set of rectangular electrodes with horizontal and vertical slits (corrective lens) is used to make a position focus approximately 300 mm from the center of the quadrupole, indicated by the vertical dashed line in panels (b) and (c). Using an Einzel lens consisting of three cylindrical electrodes (magnifying lens), this image is mapped onto a Micro-Channel Plate detector mounted in front of a phosphor screen. The image is recorded using a CCD camera. (b) and (c) Equipotential lines in the lens system along the horizontal and vertical plane, respectively. The black and green lines show trajectories of ions starting with a velocity along the z axis of 0 and 300 m/s, respectively.

consisting of an array of 101 deceleration stages. Adjacent stages are 5.5 mm apart. Each deceleration stage is formed by two parallel 3 mm diameter cylindrical rods, spaced 2 mm apart. The two opposite rods are switched to +10 and -10 kV by four independent HV switches that are triggered by a programmable delay generator. The velocity of the molecular beam is controlled completely by the computer generated burst sequence (for details on Stark deceleration, see Refs. [22, 38, 58]). An electrostatic quadrupole, mounted 30 mm behind the decelerator, is used for focusing the slow molecules and to provide an extraction field for the velocity map imaging system. The chamber that houses the quadrupole guide is differentially pumped and kept at a pressure of 3×10^{-8} mbar when the pulsed valve is operating.

A schematic view of the quadrupole and ion optics is shown in Fig. 3.1(a). The quadrupole consists of four 20 mm diameter cylindrical rods that are placed on the outside of a 20 mm diameter circle. Alternating positive and negative voltages of up to 6 kV are applied to adjacent rods to focus decelerated ammonia molecules. The molecules are focused 90 mm downstream from the decelerator, where they are ionized using a (2+1) REMPI scheme. The laser radiation (~ 10 mJ in a 5 ns pulse @322 nm) is focused between the rods of the quadrupole using a lens with a focal length of 500 mm. In order to extract the ions, a positive voltage pulse is applied to the left-hand side quadrupole rods while the other two rods are grounded. In this way, ions are pushed towards the corrective lens consisting of five rectangular (80×40 mm²) electrodes, two of which have a vertical slit aperture (10×30 mm²) and three have a horizontal slit aperture (50×10 mm²). The fourth electrode is composed of two parts such that a voltage difference can be applied between the upper and lower part. The first electrode of the corrective lens is placed 40 mm away from the center of the quadrupole, while the next electrodes are separated by 15 mm. After a 220 mm long flight tube, the ions pass a magnifying lens that consists of three circular electrodes with 15 mm circular apertures [59]. Finally, after another 240 mm long flight tube, the ions impinge upon a double Multi-Channel Plate (MCP) mounted in front of a fast response ($1/e$ time ~ 10 ns) Phosphor Screen (Photonis P-47 MgO). The light of the phosphor screen is imaged onto a CCD camera (PCO 1300, 1392×1040 pixels). By applying a timed voltage pulse with a high-voltage switch (Behlke HTS 31-03-GSM), the gain of the front MCP can be gated to select ammonia ions, thus eliminating background signal due to oil and other residual molecules in the vacuum.

In Fig. 3.1(b and c), the equipotential lines in the lens system are shown along the horizontal and vertical plane, respectively. Also shown in the figure are the trajectories of ions, starting with a velocity along the z -axis of 0 (black lines) or 300 m/s (green lines). These calculations were performed using the SIMION package [60]. With voltages applied to the left-hand side rods of the quadrupole, the ions are defocused in the horizontal plane [Fig. 3.1(b)]. This is compensated by applying a voltage difference between the right-hand side rods of the quadrupole and the first electrode. If an extraction voltage of +500 V is applied, a voltage of -1000 V is required on the first electrode to create a focus slightly before the magnifying lens. From our simulations, molecules starting with a velocity of 300 m/s along the z -axis are displaced from the center by approximately 0.5 mm. The magnifying lens is used to map the image plane onto the position sensitive detector, magnifying the image by a factor of about 6. In the vertical direction (Fig. 3.1(c)), the divergence of the beam is not affected by the quadrupole or the first two electrodes. The ions are focused onto the image plane by applying a voltage of -1700 V to the fourth electrode while keeping the other electrodes and the flight tubes at a voltage

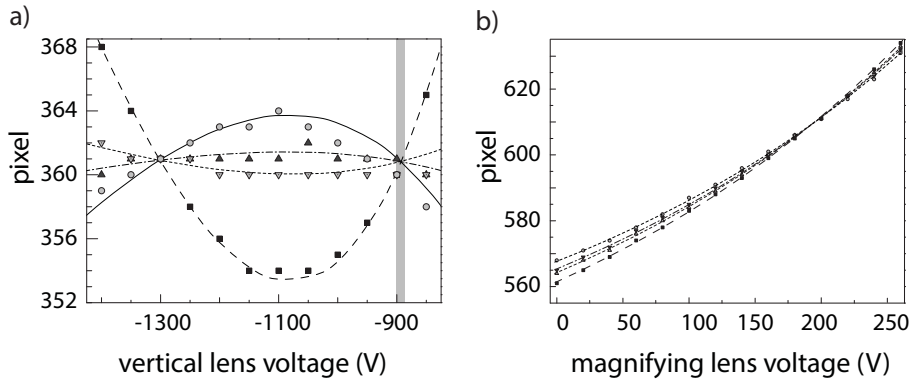


Figure 3.2 – (a) Measured vertical position of the ions as a function of the voltage applied to the fourth electrode of the corrective lens with the laser focused at four different vertical positions over a range of about 0.5 mm in the quadrupole. A voltage of -500 V is applied to the left-hand side quadrupole rods while a voltage of -1000 V is applied to all other electrodes. The gray-shaded area indicated which position focus had been used. (b) Measured vertical position of the ions as a function of the voltage applied to the magnifying lens. The fourth electrode is kept at -1700 V. The other voltages are set as in (a).

of -1000 V.

In our VMI system, the focusing properties along the horizontal plane are determined by the voltage difference between the first electrode and the left-hand side of the quadrupole, while the focusing properties along the vertical plane are determined by the voltage applied to the fourth electrode. Note that the second and third electrodes are kept at the same voltage to ensure that the vertical and horizontal focusing properties are fully uncoupled. In addition, the position of the beam can be steered in the horizontal and vertical plane by applying small voltage differences (typically about 30 V) between the two right-hand side quadrupole rods and between the upper and lower part of the fourth electrode, respectively.

3.3 Characterizing the ion optics

In order to have optimal velocity resolution, the voltages need to be applied such that ions with the same initial velocity but a different initial position are focused at the same position on the detector. In the y direction, ions are col-

lected over a range that is limited by the gap between the quadrupole rods. A position focus is found by changing the voltage applied to the left-hand side rods until the observed ion distribution in the horizontal direction is minimized. In the z direction, the optimal settings are found by scanning the voltage applied to the fourth electrode while the laser focus was located at different heights. In these measurements, shown as the symbols in Fig. 3.2, the beam is decelerated from 300 to 100 m/s and the height of the laser focus was changed over a range of about 0.5 mm. The curves in Fig. 3.2 are the result of trajectory simulations using SIMION [60]. For the measurement shown in Fig. 3.2(a) the magnifying lens was not used, i.e., it was set at the same voltage as the flight tubes. It is seen that for an applied voltage around -1100 V the beam is neither focused nor defocused and the vertical position at which the ions arrive at the detector directly reflects the height of the laser focus (under our experimental conditions, one pixel corresponds to about 0.05 mm). Note that -1100 V is slightly more negative than the expected -1000 V that is applied to the other electrodes. This is attributed to the finite size of the electrodes.

When the voltage applied to the fourth electrode is larger (more negative) than that of the surrounding electrodes, the ions are first accelerated and then decelerated as they pass the fourth electrode. At the same time, they experience a focusing, a defocusing and again a focusing force. As the ions are (on average) faster and closer to the axis when they experience a defocusing force and slower and further away from the axis when they experience a focusing force, the overall effect of the field is focusing. This is the basic operation principle of an Einzel lens [56]. The same argument holds for the situation when the voltage applied to the fourth electrode is smaller (less negative) than that applied to the surrounding electrodes. As a result of this effect, position foci are observed at voltages of -900 V and -1300 V. Either voltage setting can be used to perform velocity map imaging; we chose the lower voltage setting.

When the magnifying lens is used, the focal length of the first horizontal and vertical lens needs to be reduced. When a voltage of $+550$ V is applied to the left-hand side rods of the quadrupole and a voltage of -1730 V is applied to the fourth electrode, the focal plane is situated about 30 mm before the magnifying lens. It is seen from the measurements and simulations shown in Fig. 3.2(b) that the focal plane is imaged onto the detector when a voltage of $+200$ V is applied to the middle electrode of the magnifying lens.

3.4 Experimental results

In Fig. 3.3(a), a typical camera image is shown with the voltages set to obtain optimal velocity resolution. In this measurement, the decelerator is set

to decelerate ammonia molecules from 300 m/s to 10 m/s. The image is averaged over 256 shots. For each laser shot, pixels below a certain threshold are set to zero before adding up the images. The bright spot at the center of the image corresponds to the decelerated molecules, while the scattered spots result from thermal background ammonia molecules in the vacuum. Note that the ion distribution is clipped by the aperture of the magnifying lens. On the upper side and the right-hand side, the horizontal and vertical position is translated into horizontal and vertical velocity, respectively (*vide infra*).

In Fig. 3.3(b), the observed ion signal is shown as a function of time with respect to the start of the burst sequence applied to the decelerator. The lower trace is obtained by counting the ions over the area enclosed by the $100 \times 100 \text{ (m/s)}^2$ white square shown in Fig. 3.3(a), while the upper trace is obtained by counting the ions over the entire area of the camera. Ions are counted using the centroiding method introduced in Ref. [61]. Each data point is averaged over 32 shots. If ions are counted over the entire area of the camera, typically some 20 background ions are detected. By only counting ions within the selected area, this background is reduced by a factor of $550^2\pi/100^2 \approx 100$. Note that for a given voltage the quadrupole will focus molecules within a small velocity interval. As a result, the width of the time of flight profile does not reflect the velocity spread of the decelerated packet, but rather the position spread of the packet as it leaves the decelerator.

In Fig. 3.4, the longitudinal velocity of the molecular beam is shown as a function of time with respect to the start of the burst sequence applied to the decelerator. For this image, the decelerator was set to decelerate from 300 to 100 m/s. At every time delay, an image is averaged over 64 shots and the intensity is integrated over the horizontal direction of the camera. This results in 156 vertical lines which are combined to obtain Fig. 3.4(a). The observed signal follows a hyperbolic curve due to the inverse relation between velocity and time. The most intense part of the beam is observed at short times having an average velocity of 300 m/s. These are molecules that were not in sync with the time sequence and, as a result, they are on average neither decelerated nor accelerated but they do experience a focusing effect in the transverse directions. At later arrival times, four packets are seen that are offset from this hyperbola. The packet arriving at $3700 \mu\text{s}$ originates from molecules that were at the right position near the entrance of the decelerator at the start of the time sequence and that passed through all 101 deceleration stages in sync with the deceleration fields. These molecules entered the decelerator with a velocity of 300 m/s and exit the decelerator with a velocity of 100 m/s. The earlier peaks originate from molecules that were either one or two periods further inside the decelerator at the start of the time sequence. These molecules also entered the decelerator with a velocity of 300 m/s, but since they missed the last two or four deceleration stages they exit the decelerator with a velocity

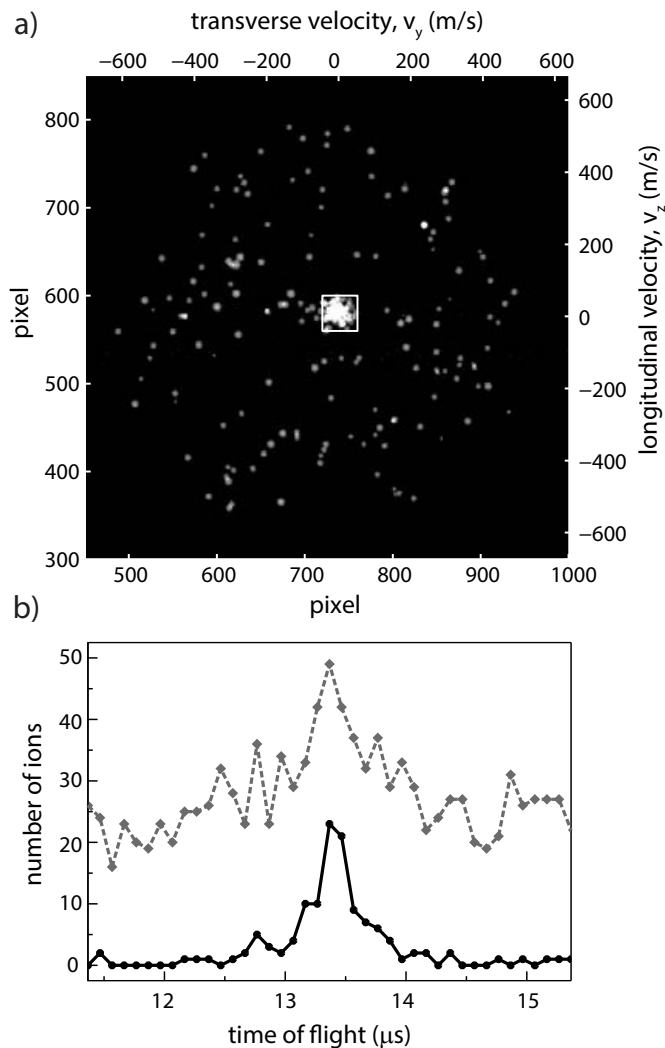


Figure 3.3 – (a) Camera image showing the distribution of ions. The MCP gate is set to detect ammonia ions only. The bright spot inside the square corresponds to ammonia molecules that are decelerated from 300 to 10 m/s. (b) Time-of-flight distributions for a molecular beam decelerated to 10 m/s. The dashed curve is obtained by counting ions over the entire area of the camera, while the solid curve is obtained by counting ions inside the white square depicted in (a).

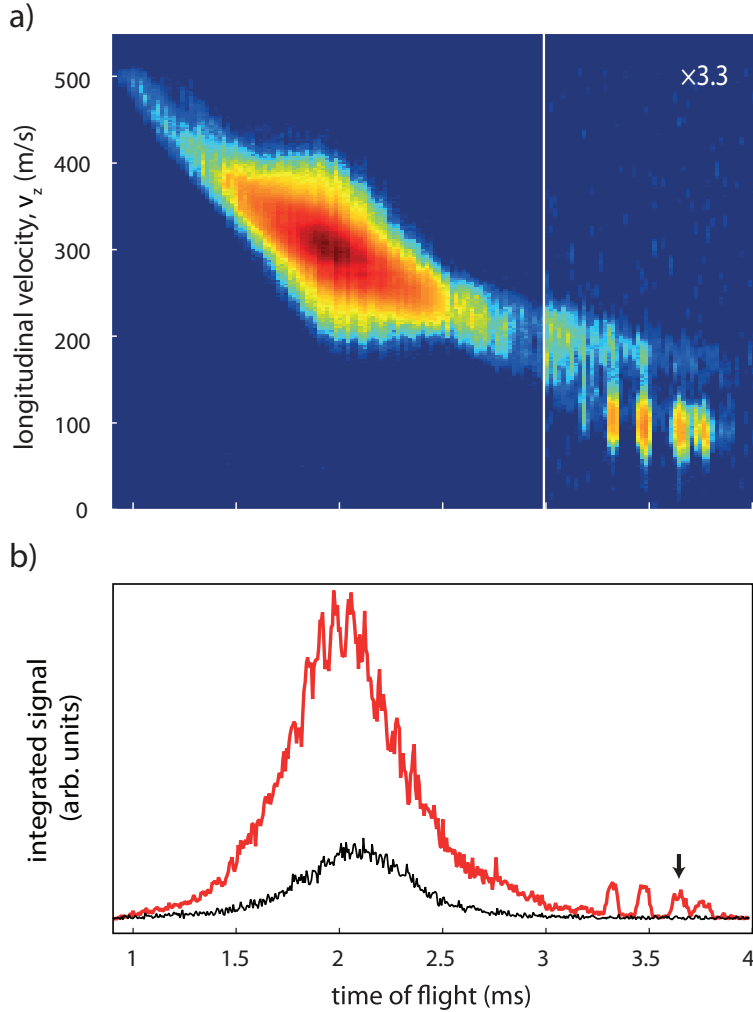


Figure 3.4 – (a) Longitudinal velocity of the ammonia beam as a function of time. The intensity of the right-hand side panel is scaled by a factor of 3.3 for clarity. (b) Integrated ion signal as a function of time with the decelerator on (thick red curve) and with the decelerator off (thin black curve). The arrow indicates the position of the synchronous packet of molecules.

of 108 or 115 m/s, respectively. The peak that appears at a later time in the time-of-flight distribution originates from molecules entering the decelerator with a lower initial velocity, catching up with the time sequence one period later. Throughout the decelerator, it trails the synchronous packet by 11 mm, exiting the decelerator with the same final velocity of 100 m/s. Although the resolution of our VMI system is insufficient to resolve the difference in velocity between the distinct packets, a small displacement between the first three packets can be observed. Note that the figure resembles the calculation presented in Fig. 2 of Heiner *et al.* [58], the main difference being that here we plot the longitudinal velocity as a function of time at the detection zone, whereas Heiner *et al.* plot the longitudinal velocity as a function of position in the decelerator at specific times.

In Fig. 3.4(b), the ion signal is integrated over the total area of the camera. The red curve shows the time-of-flight with the decelerator on, while the black curve shows the same measurement taken with the decelerator off. Note that the observed oscillations in the undecelerated part of the beam are due to velocity modulations, and are well reproduced in simulations [22].

In order to calibrate the velocity axis, we have recorded VMI images while the velocity of the beam was scanned from 150 to 5 m/s in steps of 1 m/s by changing the burst sequence applied to the Stark decelerator. At every velocity, an image is averaged over 64 shots and the intensity is integrated over the horizontal direction of the camera. This results in 145 vertical lines which are combined to obtain Fig. 3.5(a). Since molecules are ionized using a focused laser beam, the number of detected ions is proportional to the density of the decelerated beam. Due to the increasing time of flight, this density decreases rapidly when the velocity of the beam is lowered. In these measurements, the quadrupole is set to transversely focus molecules of 10 m/s at the position of the laser. As a result, a bright spot at this velocity is observed in Fig. 3.5(a) (shown enlarged in the inset). In Fig. 3.5(b), the ion signal is integrated over the total area of the camera. A peak is observed when molecules are decelerated to 10 m/s corresponding to molecules that are focused 90 mm downstream from the decelerator, where the molecular beam crosses the ionisation laser.

The straight line shown in Fig. 3.5(a) is used to translate the position at the camera into a vertical velocity. The FWHM velocity spread of the beam that is inferred from the camera images is 35 m/s (corresponding to 20 pixels on the camera). As, at the used settings of the decelerator, the longitudinal velocity spread of the beam is below 10 m/s [38], we conclude that the velocity resolution of the lens system is on the order of 35 m/s. The instrumental resolution of the system might be better than this as in our case the velocity resolution is limited by the recoil of the photoelectron during the ionization step. Ammonia molecules are ionized using a (2+1) REMPI scheme via the $B(\nu_2 = 3)$ state,

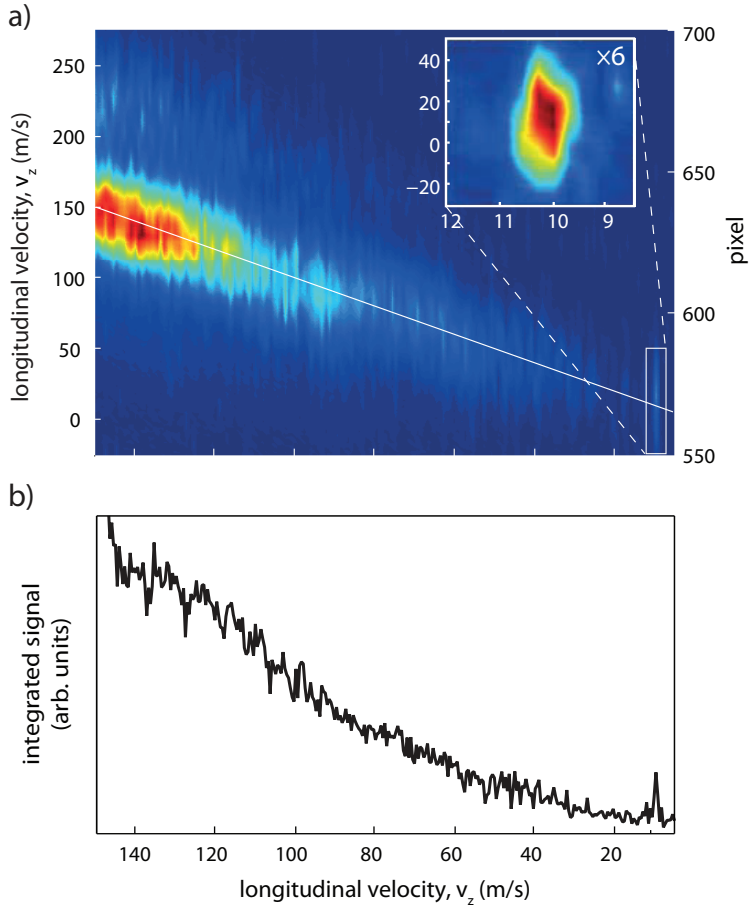


Figure 3.5 – (a) Longitudinal velocity of the ammonia beam as a function of the velocity set by the burst sequence applied to the decelerator. The quadrupole is set to focus molecules of 10 m/s at the position of the laser. The inset shows an enlarged view of molecules that are focused with the quadrupole. The intensity is scaled by a factor of 6 for clarity. (b) Integrated ion signal as a function of velocity with the burst sequence set to decelerate molecules to different velocities.

producing ions predominantly in the $\nu_2 = 3$ state [62].

Since the ionization potential of ammonia is 10.07 eV [63], a velocity of 20 m/s is imparted to the ion in either direction. Note that, in our experiment, the polarization of the laser was parallel to the molecular beam axis. A better velocity resolution may have been obtained if we had chosen the polarization perpendicular to the molecular beam. During the experiment we found that the exact arrival position of ions with a certain velocity changed from day to day which is attributed to charging effects of nearby isolators used for suspending the quadrupole and the ion optics. These charging effects might contribute to the observed velocity resolution.

3.5 Conclusions

A setup consisting of a series of planar electrodes is used for performing velocity map imaging inside an electrostatic quadrupole guide. We obtain a velocity resolution of 35 m/s, limited by recoil of the photoelectron and by the presence of isolators used for suspending the quadrupole. Our work demonstrates that velocity map imaging can be performed in unconventional electrode configurations while achieving a resolution that is sufficient for most purposes. This should be useful for studies in electrostatic traps [38], storage rings [64, 65] and molecular fountains [52]. An often quoted phrase in the ion imaging community is: “if you do not use VMI, you throw away information”. In this work, the information obtained from VMI is used to detect slow molecules free of any signal from thermal background gas.

Chapter 4

Static trapping of polar molecules in a traveling wave decelerator*

In this chapter, we present experiments on decelerating and trapping ammonia molecules using a combination of a Stark decelerator and a traveling wave decelerator. In the traveling wave decelerator a moving potential is created by a series of ring-shaped electrodes to which oscillating high voltages are applied. By lowering the frequency of the applied voltages, the molecules confined in the moving trap are decelerated and brought to a standstill. As the molecules are confined in a *true* 3D well, this kind of deceleration has practically no losses, resulting in a great improvement on the usual Stark deceleration techniques. The necessary voltages are generated by amplifying the output of an arbitrary wave generator using fast HV-amplifiers, giving us great control over the trapped molecules. We illustrate this by experiments in which we adiabatically cool trapped NH_3 and ND_3 molecules and resonantly excite their motion.

4.1 Introduction

Cold molecules offer fascinating prospects for precision tests of fundamental physics theories, cold chemistry and quantum computation (for recent review papers see [22, 66, 67, 68]). One of the methods that has been successful in producing samples of cold and trapped molecules is Stark deceleration. This technique uses a series of strong electric fields that are switched at the appropriate times to lower the velocity of a beam of molecules in a stepwise fashion. In conventional Stark decelerators the principle of phase stability

*Based on M. Quintero-Pérez, P. Jansen, T. E. Wall, J. E. van den Berg, S. Hoekstra, and H. L. Bethlem, *Phys. Rev. Lett.*, vol. 110, p. 133003, Mar 2013.

is employed, which ensures that molecules experience an *effective* 3D potential well that keeps them in a compact packet during the deceleration process [22, 38, 69]. Whereas the approximations used to derive this effective well are valid at high velocity, they no longer hold at low velocity, when the characteristic wavelength of the longitudinal and transverse motion of the molecules becomes comparable to the periodicity of the decelerator. As a result of this breakdown, the number of molecules in the packet as well as its phase-space density decrease at low velocities [39]. Further losses take place when the decelerated molecules are loaded into a trap [38, 70, 71].

Expanding on earlier work on chip-based Stark decelerators [72], Osterwalder and co-workers [73, 74] decelerated CO molecules from 288 m/s to 144 m/s using a series of ring electrodes to which a sinusoidal voltage was applied. In this traveling wave decelerator, the molecules experience a *genuine* rather than an *effective* potential well that moves continuously along with the molecules. The molecules are decelerated by slowly decreasing the velocity of the moving potential well by lowering the frequency of the applied voltages. Besides avoiding losses at low velocities, a traveling wave decelerator has the advantage that molecules can be brought to a complete standstill and trapped without the need to load them into a separate electrode geometry. Furthermore, as the molecules are always close to the zero-point of the electric field, they can be decelerated in states that become high-field seeking at relatively low electric fields. This makes it possible to decelerate heavy molecules such as YbF [75] and SrF [76].

In this chapter, we use a traveling wave decelerator to decelerate and trap ammonia molecules. Our main motivation for this research is the possibility to use the traveling wave decelerator as a source of cold molecules for a molecular fountain [30]. Previous attempts to create a fountain using a Stark decelerator were unsuccessful due to losses at low velocities and a complex lens-system for cooling and collimating the slow beam [39]. A traveling wave decelerator should solve both of these issues.

4.2 Experimental setup

Figure 4.1 shows a schematic view of the vertical molecular beam machine. A supersonic beam of ammonia molecules is decelerated to around 100 m/s using a conventional decelerator consisting of a series of 100 electrode pairs to which voltages of ± 10 kV are applied (for details of the beam machine and Stark deceleration of ammonia, see [30, 38] and Chapter 1). A traveling wave decelerator is mounted 24 mm above the last electrode pair. The design and dimensions of the decelerator are copied from Osterwalder and co-workers [73, 74]. The decelerator consists of 336 ring electrodes with an inner

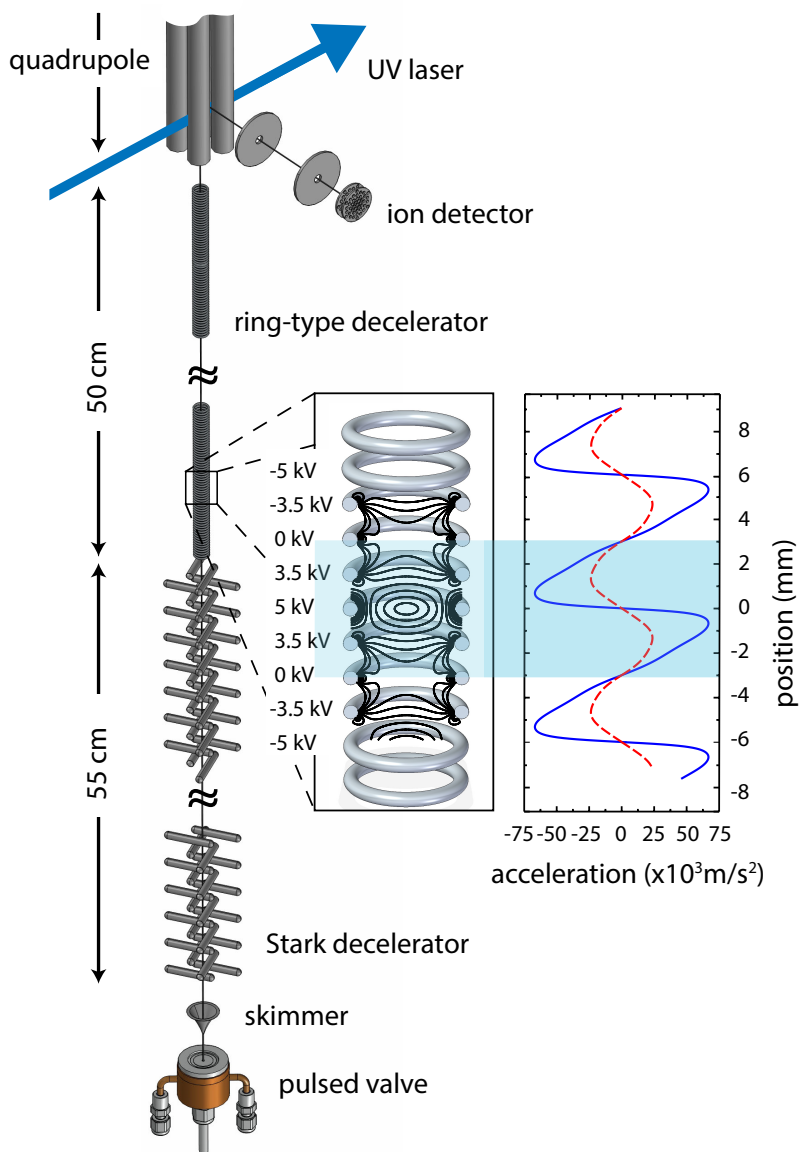


Figure 4.1 – Schematic view of the vertical molecular beam machine. The inset shows the electric field magnitude inside the ring-type decelerator with the voltages on the different electrodes as indicated. The electric field magnitude is shown in steps of 2.5 kV/cm. In the rightmost panel the longitudinal acceleration on NH_3 (dashed red curve) and ND_3 (solid blue curve) molecules is shown along the molecular beam axis.

diameter of 4 mm which are attached to one of eight supporting bars. Consecutive rings are separated by 1.5 mm (center to center), resulting in a periodic length, L , of 12 mm. The voltages applied to the eight support bars are generated by amplifying the output of an arbitrary wave generator (Wuntronic DA8150) using eight fast HV-amplifiers (Trek 5/80) up to ± 5 kV. A 50 cm long quadrupole is mounted 20 mm above the traveling wave decelerator. In the experiments described in this Letter, the quadrupole is used only to extract ions that are produced by a focused UV laser that crosses the molecular beam 40 mm above the last ring electrode. The ions are counted by an ion detector.

At any moment in time, the voltages applied to successive ring electrodes follow a sinusoidal pattern in z , where z is the position along the beam axis. These voltages create a minimum of electric field every 6 mm, representing a true 3D trap for weak-field seeking molecules. By modulating these voltages sinusoidally in time the traps can be moved along the decelerator. The velocity of the trap is given by $v_z(t) = f(t)L$, with f being the modulation frequency. A frequency that is constant in time results in a trap that moves with a constant positive velocity along the cylindrical axis. A constant acceleration or deceleration can be achieved by applying a linear chirp to the frequency [73, 74].

The inset of Fig. 4.1 shows the electric field magnitude inside the ring decelerator with the voltages on the different electrodes as indicated. The electric field near the center has a quadrupolar symmetry, i.e., the electric field magnitude increases linearly away from the center. It is essential to the operation of the decelerator that the trapping potential maintains a constant shape and depth while it is moved. In the chosen geometry, the electric field gradients in the bottom of the well, as well as the trap depth in the longitudinal direction are nearly independent of the position of the trap minimum. The trap depth in the transverse direction, however, is 40% deeper when the trap minimum is located in the plane of a ring compared to the situation when the trap minimum is located in the middle between two rings.

The panel on the right hand side of Fig. 4.1 shows the acceleration experienced by NH_3 (dashed red curve) and ND_3 (solid blue curve) molecules as a function of z . The inversion splitting in NH_3 is 23.8 GHz, while it is only 1.4 GHz in ND_3 . As a result, the Stark effect in NH_3 is quadratic up to electric fields of 20 kV/cm and NH_3 molecules experience an acceleration that increases linearly with the distance from the trap center. The Stark effect in ND_3 , on the other hand, becomes linear at much smaller fields and the ND_3 molecules experience a linearly increasing acceleration close to the trap center only. As a result of the different shape (and magnitude) of the force, the dynamics of these two ammonia isotopologues in the decelerator is markedly different, as will be seen in the experimental results.

4.3 Experimental results

Figure 4.2 shows the density of NH_3 (upper panel) and ND_3 molecules (lower panel) above the decelerator as a function of time when different waveforms are applied to the ring decelerator as shown in the inset. In all cases, a packet of molecules is decelerated to 90 m/s using the conventional Stark decelerator and injected into the traveling wave decelerator. The horizontal axis is always centered around the expected arrival time of the molecules. The black curves show the density when a sinusoidal voltage with an amplitude of 5 kV and a (constant) frequency of 7.5 kHz is applied to the ring decelerator. With these settings, molecules traveling at 90 m/s are guided through the ring decelerator, resulting in a Gaussian distribution around the origin. The width of the time-of-flight (TOF) profile mainly reflects the velocity spread of the guided molecules. As for ND_3 the moving trap is deeper than for NH_3 , its TOF profile is accordingly wider. Wings are observed at earlier and later arrival times, which are attributed to molecules that were preceding or trailing the synchronous molecule by 11 mm in the conventional Stark decelerator and that are captured at every other minimum of the traveling wave decelerator; i.e., 12 mm before or after the synchronous molecule.

The light blue, dark blue and green curves in Fig. 4.2 show the recorded TOF traces when the frequency is first decreased linearly with time to a value of 5, 0.83 and 0 kHz, respectively, and subsequently increased to its original value. With these settings, molecules are decelerated to 60, 10 and 0 m/s before being accelerated back to 90 m/s, using accelerations of ± 9.2 , ± 16.4 , and $\pm 16.6 \times 10^3 \text{ m/s}^2$, respectively.

The observed NH_3 and ND_3 density decrease at lower velocities is larger than expected from simulations. We attribute the loss mainly to mechanical misalignments that lead to parametric amplification of the motion of the trapped molecules at low velocities. On inspection, it was noticed that one of the suspension bars was slightly displaced from its original position, which must have happened when the decelerator was placed in the vacuum chamber. Another loss mechanism comes from the fact that the phase space distribution of the packet exiting the conventional Stark decelerator is not perfectly matched to the acceptance of the traveling wave decelerator. As a result, the trapped packet will perform a (damped) breathing motion. This oscillation explains why the observed TOF profile for deceleration to 60 m/s is wider and more intense than the TOF profile for guided molecules. Neither loss mechanism is fundamental, and we believe they can be eliminated in future work.

The red curves in Fig. 4.2 are recorded when, after the frequency of the applied voltages is decreased to 0 kHz, the voltages are kept at constant values for 50 ms before the frequency is increased to its original value of 7.5 kHz. The

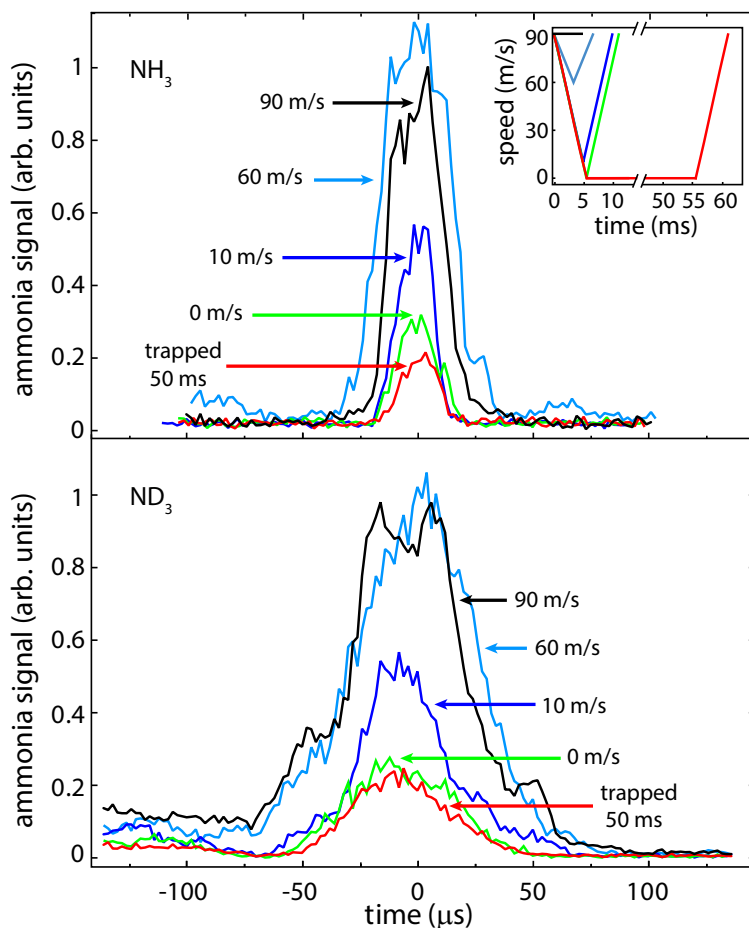


Figure 4.2 – Measured time-of-flight (TOF) profiles for NH_3 (upper panel) and ND_3 (lower panel) when molecules are guided at 90 m/s (black curve), decelerated to 60, 30 and 0 m/s (light blue, dark blue and green, respectively) and trapped for 50 ms (red curve) before being accelerated back to 90 m/s and detected. The time of flight traces have been centered around the expected arrival time. The inset shows the velocity of the electric field minimum as a function of time for the different recorded TOF profiles.

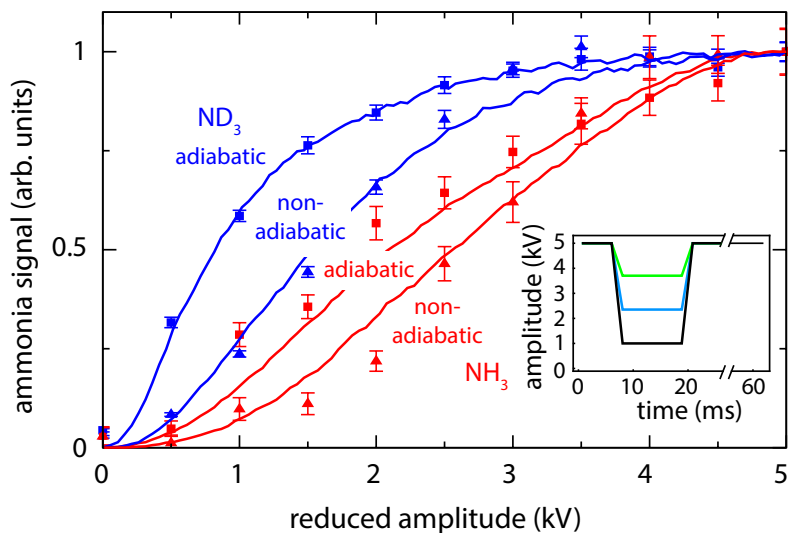


Figure 4.3 – Trapped NH_3 (red data points) and ND_3 (blue data points) signal as a function of the amplitude of the waveform when, after deceleration, the trap is slowly (squares) or abruptly (triangles) reduced. The solid lines are simulations that assume an initial temperature of 14 and 30 mK for NH_3 and ND_3 , respectively. The inset shows the amplitude of a number of typical waveforms as a function of time.

observed TOFs are almost identical to the ones recorded when the frequencies are immediately returned to their original value. This measurement demonstrates that molecules can be trapped in the laboratory frame without further losses.

As the voltages applied to the decelerator are generated by amplifying the output of an arbitrary wave generator using fast HV-amplifiers, we can change the depth (and shape) of the trap at will. This is illustrated in the measurements shown in Fig. 4.3. In these measurements NH_3 (red squares) and ND_3 (blue squares) molecules are again decelerated, trapped for a period of over 50 ms, and subsequently accelerated and detected. In this case, however, while the molecules are trapped, the voltages applied to the decelerator are ramped down (in 2 ms for ND_3 and 10 ms for NH_3), kept at a lower value for 10 ms and then ramped up to 5 kV. Typical waveform amplitudes as a function of time are shown in the inset. Lowering the voltages of the trap has two effects: (i) the trap frequency is lowered, adiabatically cooling the molecules; (ii) the trap depth is reduced, allowing the hottest molecules to escape the trap.

The solid lines show the result of a simulation assuming an (initial) temperature of 14 mK for NH_3 and 30 mK for ND_3 . Note that we use temperature here only as a convenient means to describe the distribution; the densities are too low to have thermalization on the timescales of the experiment. For comparison, the blue triangles show measurements when the trap voltages are abruptly ($10 \mu\text{s}$) lowered. In this case no adiabatic cooling occurs and as a result the signal decreases more rapidly when the voltages are ramped to lower voltages. The solid lines again show the result of a simulation. It is seen that, both in the adiabatic and in the nonadiabatic case, the NH_3 signal drops more rapidly than the ND_3 signal. This is mainly because the ratio of the temperature of the molecules to the trap depth at 5 kV is larger for NH_3 than for ND_3 , i.e., the NH_3 molecules initially fill the trap almost completely while the ND_3 molecules only occupy a fraction of the trap. We have also measured the number of molecules that remain trapped at 2 kV as a function of the time used for lowering the voltages (shown in Fig. 5.8). These measurements confirm that the ND_3 and NH_3 molecules follow the trap adiabatically when the ramping times are longer than 1 ms.

Figure 4.4 shows the normalized signal of trapped NH_3 (upper panel) and ND_3 molecules (lower panel) when the amplitude of the trapping voltages is modulated. If the frequency of the modulation matches a characteristic frequency of a trapped molecule, the amplitude of the motion of the molecule inside the trap is increased [77]. As a result, the density is decreased. The excitation scans are recorded in two situations. In the first case (red data points), molecules are decelerated and trapped for 30 ms before the excitation voltages are applied, after which they are accelerated and detected. In the second case (blue data points), the trap voltages are adiabatically lowered for a period of 10 ms before the excitation voltages are applied, allowing the hottest molecules to escape the trap. The amplitude of the waveform for both cases is shown in the inset.

For NH_3 , two strong resonances are seen around 0.9 and 1.4 kHz, assigned to $2f_r$ and $2f_z$, respectively, where f_r and f_z are the radial and longitudinal trap frequency, respectively. For ND_3 , a strong resonance is observed around 1.9 kHz and a weaker resonance around 3 kHz. These resonances are assigned to $2f_r$ and $f_r + f_z$, respectively. Due to the anharmonicity of the trap, the width of the observed resonances depends strongly on temperature. The solid curves show simulations that assume a thermal distribution with temperatures as indicated in the figure. Note that for the ND_3 measurements presented in Fig. 4.4, the Stark decelerator is set to decelerate from a lower initial velocity (i.e., operated at a lower phase angle [69]) than for the ND_3 measurements presented in Fig. 4.3. As a result, the velocity spread of the decelerated beam is larger and the temperature determined from these measurements is also larger. These data show the great control allowed by the decelerator, us-

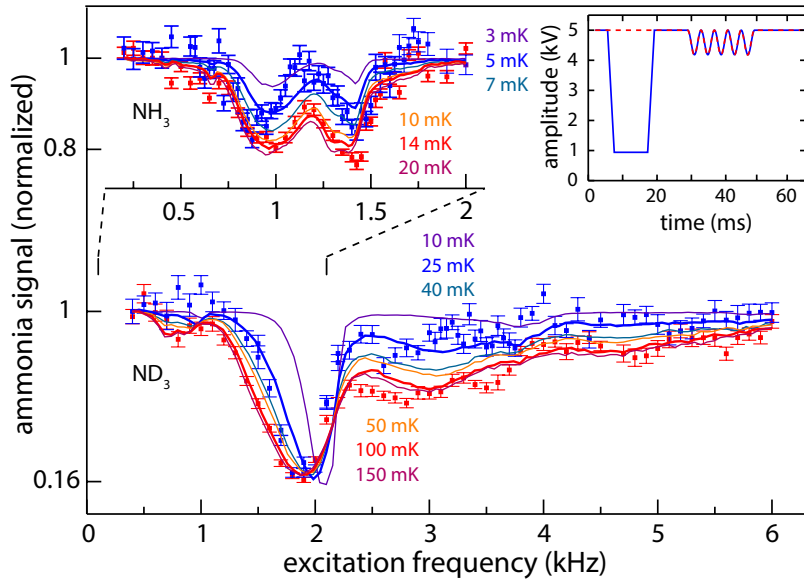


Figure 4.4 – Fractional trap loss as a function of excitation frequency for NH_3 (upper, offset for clarity) and ND_3 (lower) with (blue data points) and without (red data points) reducing the trap depth. In the inset, the amplitude of the waveform is shown as a function of time. The amplitude is modulated by 400 V for NH_3 , and by 800 V for ND_3 . The solid curves result from 3D simulations that assume a truncated thermal distribution with temperatures as indicated in the figure.

ing the molecules to map out the trapping potentials, and using this mapping as direct evidence of phase-space manipulation in the trap.

4.4 Conclusions

In conclusion, we have decelerated and trapped ammonia (NH_3 and ND_3) molecules using a combination of a Stark decelerator and a traveling wave decelerator. We take advantage of the strong acceleration of a conventional Stark decelerator to decelerate molecules to around 100 m/s, removing 90% of their kinetic energy. We then exploit the stability of a traveling wave decelerator to bring molecules to a standstill inside the decelerator. In this way, the voltages are varied over a frequency range that is covered by commercially available HV-amplifiers. We demonstrate that this setup can be used to change the position, shape and depth of the trap at will, giving us unique control over the

trapped molecules. This control will greatly facilitate the implementation of schemes to further cool the molecules, such as sisyphus cooling [78] and evaporative cooling [79].

Chapter 5

Characterizing the traveling wave decelerator*

In Chapter 4, we have demonstrated static trapping of ammonia isotopologues in a decelerator that consists of a series of ring-shaped electrodes to which oscillating high voltages are applied. In this chapter we provide further details about this traveling wave decelerator and present new experimental data that illustrate the control over molecules that it offers. We analyze the performance of our setup under different deceleration conditions and demonstrate phase-space manipulation of the trapped molecular sample.

5.1 Introduction

Cold molecules offer many exciting prospects in both chemistry and physics (for recent review papers see Refs. [22, 66, 67, 68]). The great control that can be exerted over cold molecules allows the study and manipulation of collisions and chemical reactions [80, 81]. The strong dipole-dipole interactions between cold molecules make them excellent systems for quantum simulation and computation [82, 83, 84]. With their rich structure, molecules can be useful systems for making precision tests of fundamental physics, such as the measurements of the electron EDM [24, 25] and the search for time-variation of fundamental constants [37, 53, 85, 86]. In particular this last application is of great interest to our group, and as a part of this research we are building a molecular fountain [52].

A fountain requires great control over the molecules, in our case slowing them from around 300 m/s to rest, cooling them, and then launching them

*Based on P. Jansen, M. Quintero-Pérez, T. E. Wall, J. E. van den Berg, S. Hoekstra, and H. L. Bethlem, *Phys. Rev. A*, vol. 88, p. 043424, Oct 2013.

upwards at around 3 m/s. A tool that has been successfully used to exert control over molecules is the Stark decelerator [22, 38, 40]. While excellent at removing kinetic energy, a Stark decelerator becomes lossy for low speeds (<100 m/s) because of its reliance on creating an effective 3D potential well. When the characteristic wavelength of the longitudinal and transverse motion becomes comparable to the periodicity of the decelerator, the approximations used to derive this effective well no longer apply and both the number of molecules and phase-space density decline with speed [39, 87]. To avoid these losses at low speeds we use a traveling wave decelerator.

Based on the design of Osterwalder et al [73, 74], this decelerator uses a sequence of ring-shaped electrodes to which a space- and time-varying voltage is applied. In this way the traveling wave decelerator creates a genuine rather than effective 3D trap that moves along the decelerator, co-propagating with the molecules. By reducing the speed of this co-moving trap the molecules are decelerated. The lowest speed reached by Osterwalder et al was 120 m/s, limited by the lowest frequency at which the voltage could be varied. The same decelerator was used to slow YbF molecules from a buffer gas source from 300 m/s to 276 m/s, limited by the deceleration that could be applied to these heavy molecules [75]. A 5 m long traveling wave decelerator is currently under construction at the KVI in order to decelerate SrF molecules [76].

We have recently been able to slow molecules to rest, and statically trap them inside the decelerator by using high voltage amplifiers that can sweep the high voltage from 15 kHz down to DC. We use a conventional Stark decelerator to slow ammonia molecules from 300 m/s to around 100 m/s, removing 90% of their initial kinetic energy over a length of only 50 cm. We then load the molecules into the traveling wave decelerator for the remaining deceleration to standstill (see Chapter 4).

This chapter will provide further details about the traveling wave decelerator, and present new experimental data that illustrate the great control over molecules that is offered by this decelerator.

5.2 Experimental setup

Figure 5.1 shows a schematic view of our vertical molecular beam machine. In brief, a pulsed ($\sim 100 \mu\text{s}$) ammonia beam is released into vacuum from a solenoid valve (General Valve series 99) at a 10 Hz repetition rate. By cooling the valve housing to typically -50°C and seeding the ammonia molecules in xenon, the mean velocity of the beam is lowered to 300 m/s. The ammonia beam is decelerated using a 101-stage Stark decelerator. Adjacent stages are 5.5 mm apart. Each deceleration stage is formed by two parallel 3 mm diameter cylindrical rods, spaced 2 mm apart. The two opposite rods are switched to

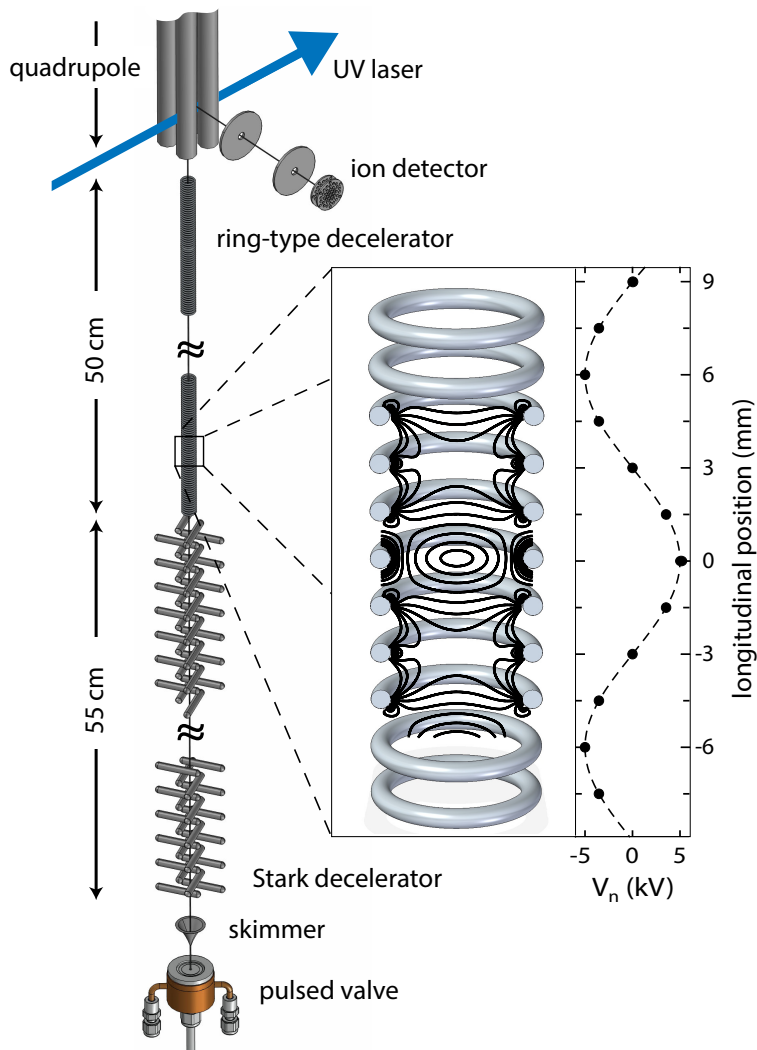


Figure 5.1 – Schematic view of the vertical molecular beam machine. The inset shows the electric field magnitude (in steps of 2.5 kV/cm) inside the traveling wave decelerator calculated using Simion [60]. The rightmost panel shows the sinusoidal waveform (dashed line) from which the potential that is applied to each electrode (solid circle) is sampled.

+10 and -10 kV by four independent HV switches that are triggered by a programmable delay generator. A traveling wave decelerator is mounted 24 mm above the last electrode pair. This decelerator consists of 336 ring electrodes, each of which is attached to one of eight 8 mm diameter stainless steel rods, resulting in a periodic array in which every ninth ring electrode is attached to the same rod. The rods are placed on a 26 mm diameter circle, forming a regular octagon. Each rod is mounted by two ceramic posts that are attached to the octagon via an adjustable aluminum bar that allows for fine-tuning of the alignment. The ring-shaped electrodes are made by bending 0.6 mm thick tantalum wire into the shape of a tennis racket with an inner diameter of 4 mm. Consecutive rings are separated by 1.5 mm (center to center) resulting in a periodic length of $L = 12$ mm. This combination of parameters is identical to the design of Osterwalder and co-workers [73, 74].

The voltages applied to the eight support bars are generated by amplifying the output of an arbitrary wave generator (Wuntronic DA8150) using eight fast HV-amplifiers (Trek 5/80) up to ± 5 kV. A 50 cm long quadrupole is mounted 20 mm above the traveling wave decelerator. The quadrupole can be used for focusing slow molecules and to provide an extraction field for a Wiley-McLaren type mass spectrometer setup. In the experiments described here, slow molecules are not focused and the quadrupole is used only to create the extraction field. The molecular beam overlaps with the focus of an UV laser 40 mm behind the last ring electrode of the decelerator to ionize the ammonia molecules. The nascent ions are counted by an ion detector. The chamber that houses the two decelerators and quadrupole guide is differentially pumped and kept at a pressure below 3×10^{-8} mbar when the pulsed valve is operating.

5.3 Theory

A detailed discussion of the operation principles of the traveling wave decelerator can be found elsewhere [22, 73, 74]. In this section we will summarize those results that are relevant for the current chapter.

In order to describe the operation of a traveling wave decelerator, it is useful to consider the electric field inside an infinitely long hollow conducting cylinder to which a voltage is applied that is periodic in z . As shown in Ref. [22], the electric potential on the beam axis will in this case follow the potential applied to the cylinder, but it is reduced by a factor that depends on the radius of the cylinder and the periodic length of the applied waveform. The electric field magnitude in the longitudinal direction is given by a fully-rectified sine wave, resulting in two minima per period at the positions where

the electric potential at the cylinder is maximal. At the position of these minima, the electric field magnitude in the radial direction is given by a first-order modified Bessel function of the first kind. Close to the minima the electric field increases linearly in both directions with the field gradient in the longitudinal direction being twice as large as the gradient in the radial direction. These minima will act as true 3D traps for weak-field seeking molecules. By modulating the waveform that is applied to the cylinder in time, the traps can be moved along the decelerator, while keeping a constant shape and depth.

In the actual implementation of the traveling wave decelerator, 8 ring-shaped electrodes are used to sample the infinite cylinder. The inset of Fig. 5.1 shows the electric field magnitude inside the traveling wave decelerator at a given time. The voltages applied to successive ring electrodes follow a sinusoidal pattern in z shown on the right-hand side of the figure. In order to move the traps, the sinusoidal waveform is modulated in time. As a consequence of using a finite number of electrodes, the trapping potential no longer maintains a constant shape and depth while it is moved. In the chosen geometry, the electric field gradients in the bottom of the well, as well as the trap depth in the longitudinal direction are nearly independent of the position of the trap minimum. The trap depth in the transverse direction, however, is 40% deeper when the trap minimum is located in the plane of a ring compared to the situation when the trap minimum is located directly between two rings.

The potential V_n applied to the n th electrode in the traveling wave decelerator can be expressed as [74]

$$V_n(t) = V_0 \sin \left(-\phi(t) + \frac{2\pi n}{8} \right), \quad (5.1)$$

where V_0 is the amplitude of the sine-modulated potential and ϕ is a time-dependent phase offset that governs the motion of the traps. For the electric field configuration that is shown in Fig. 5.1, the phase offset has a value of $\phi = 0 \pmod{\pi/4}$. The angular frequency of the wave is given by the time derivative of $\phi(t)$; $(d\phi/dt) = 2\pi f(t)$, where $f(t)$ is the frequency in Hz. Since one oscillation of the waveform moves the trap over one period, the velocity of the trap is given by $v_z(t) = f(t)L$. Integrating the angular frequency with respect to time results in the following expression for the phase

$$\phi(t) = \frac{2\pi}{L} \int_0^t v_z(\tau) d\tau, \quad \text{where } v_z(t) = \int_0^t a(\tau) d\tau. \quad (5.2)$$

A linear increase of ϕ with time results in a trap that moves with a constant positive velocity along the z axis. Acceleration or deceleration of the trap can be achieved by applying a chirp to the frequency.

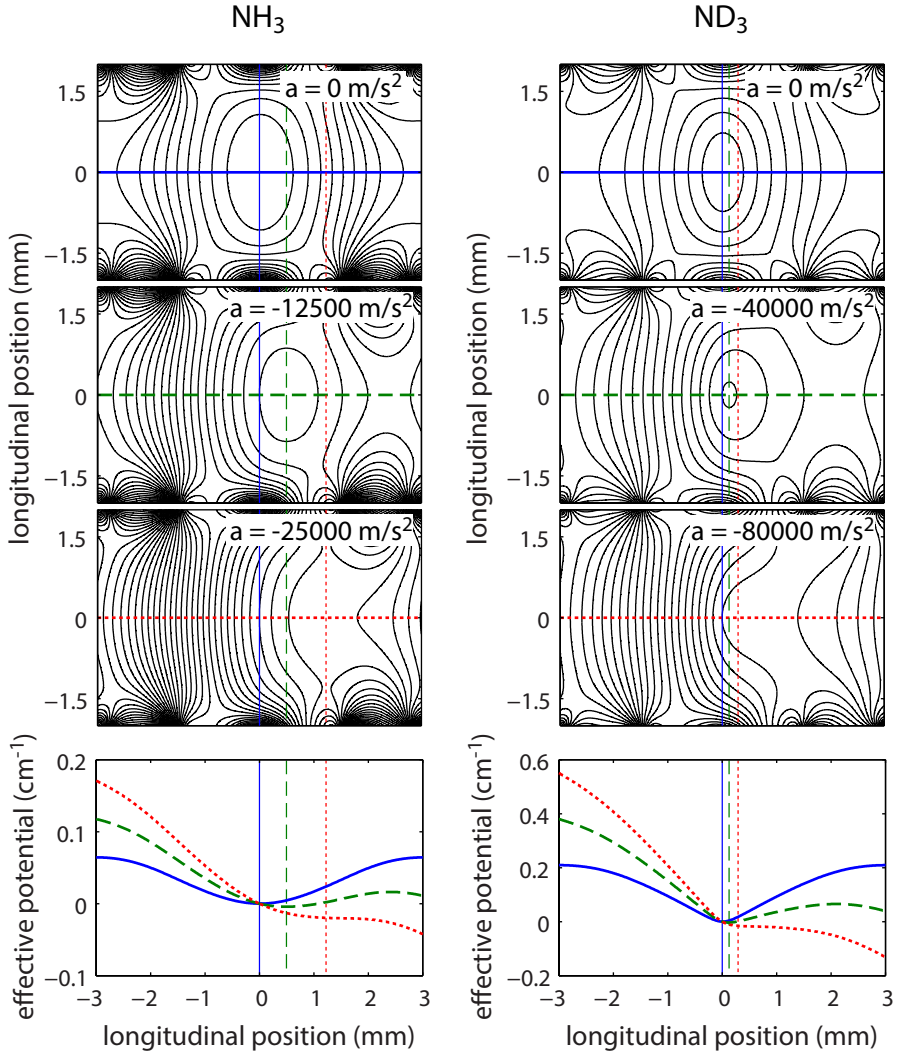


Figure 5.2 – Effective potentials for NH_3 (left) and ND_3 (right) for various accelerations and a waveform amplitude of 5 kV. Contour lines are separated by 10 mK for NH_3 and 40 mK for ND_3 . A constant acceleration produces a pseudoforce that distorts the Stark potential and reduces the trap volume and depth. Above a certain threshold the potential no longer contains a minimum and no molecules can be trapped. The lower panels show the longitudinal dependence of the effective trapping potential along the beam axis for the different accelerations (relative to $a = 0$ m/s). Note the difference in the position of the trap center between NH_3 and ND_3 for $a \neq 0$ m/s².

The acceleration or deceleration of the trap changes the effective longitudinal potential experienced by the molecules. In order to account for this pseudoforce, an additional term of the form $W_{\text{acc}} = maz$, with m the mass of the molecule and a the acceleration along the z axis, is added to the potential. In Fig. 5.2, the resulting potentials are shown for different waveforms corresponding to different accelerations as indicated. The panels on the left- and right-hand side show the potential experienced by NH_3 and ND_3 molecules, respectively. The lower panels show the effective potential along the z -axis. The inversion splitting in NH_3 is 23.8 GHz, while it is only 1.6 GHz in ND_3 . As a result, the Stark effect in NH_3 is quadratic up to electric fields of 20 kV/cm and the effective potential for NH_3 molecules is almost perfectly harmonic. The Stark effect in ND_3 , on the other hand, becomes linear at much smaller fields and the effective potential for ND_3 molecules is harmonic close to the trap center only. Note that in the figure the accelerations applied to ND_3 are about 3 times larger than those applied to NH_3 . As seen from the figure, acceleration of the trap reduces its phase-space acceptance and thus decreases the number of molecules that can be confined. Above a certain threshold value, the potential no longer contains a minimum and no molecules can be trapped at all. In addition to reducing the trap depth, acceleration of the trap results in a shift of the effective field minimum. This shift needs to be taken into account when the acceleration is not constant but a function of time, for instance, when the molecules are decelerated to a standstill and subsequently trapped at a certain position in the decelerator. We do this by rapidly ($< 20 \mu\text{s}$) sweeping the phase of the waveform. We will refer to this sweep as a “phase jump”.

5.4 Results

In this section we present data that demonstrate the versatility of the traveling wave decelerator and analyze the performance of the setup under different conditions. Results for guiding, deceleration and trapping of NH_3 and ND_3 molecules are presented in Section 5.4.1. Section 5.4.2 discusses the use of the phase jump for NH_3 and ND_3 .

5.4.1 Guiding, deceleration and trapping

In Fig. 5.3, time-of-flight (TOF) profiles of NH_3 molecules (upper panel) and ND_3 molecules (lower panel) are shown that were obtained by applying different waveforms to the traveling wave decelerator, as shown in the inset. Note that the horizontal axis is shifted in such a way that the origin corresponds to the expected arrival time of the molecules. For each measurement, a packet of molecules is decelerated to 90 m/s using the conventional Stark

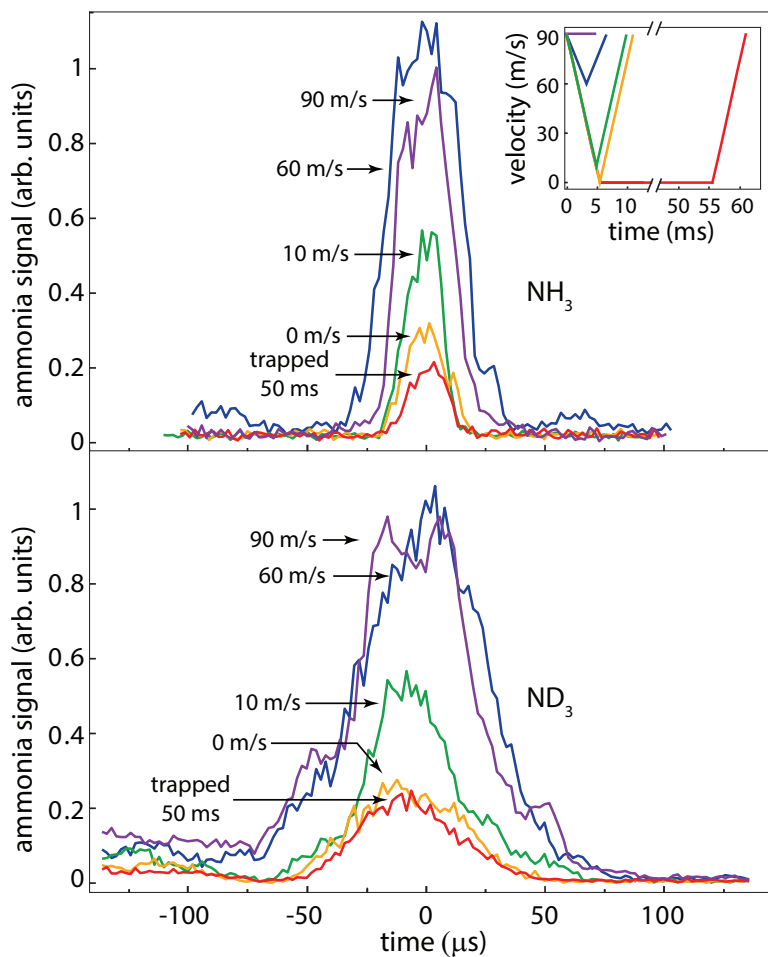


Figure 5.3 – Measured time-of-flight profiles for NH_3 (upper panel) and ND_3 (lower panel) molecules guided at 90 m/s (violet curve), decelerated to 60, 30 and 0 m/s (blue, green, and yellow curves respectively) and trapped for 50 ms (red curve) before being accelerated back to 90 m/s and detected. Each data point is the average of 90 laser shots. The time of flight traces have been centered around the expected arrival time. The inset shows the velocity of the traveling wave potential as a function of time for the different recorded TOF profiles.

decelerator and subsequently coupled into the traveling wave decelerator. The violet curves in Fig. 5.3 are TOF profiles for packets of NH_3 and ND_3 molecules that are guided through the traveling wave decelerator at the injection speed of 90 m/s by applying a waveform with a constant frequency of 7.5 kHz to the array of electrodes. The width of the TOF profile mainly reflects the velocity spread of the guided molecules. For ND_3 the moving trap is deeper than for NH_3 , and its TOF profile is accordingly wider. Wings are observed at earlier and later arrival times, which are attributed to molecules that are trapped in the electric-field minima that are located 12 mm above or below the synchronous one.

By adjusting the waveform that is applied to the traveling wave decelerator, the velocity of the molecules can be manipulated almost at will. The blue, green, and yellow traces in Fig. 5.3 are time-of-flight profiles for NH_3 and ND_3 molecules that are decelerated from 90 m/s to 60, 10 and 0 m/s and immediately reaccelerated to 90 m/s. This corresponds to chirping the applied waveform from 7.5 kHz to 5.0, 0.8, and 0 kHz and results in accelerations of ± 9.2 , ± 16.4 , and $\pm 16.6 \times 10^3 \text{ m/s}^2$, respectively.

The red curves in Fig. 5.3 show TOF profiles that are obtained under almost identical conditions as the yellow curves. However, after the velocity of the applied waveform is decreased to 0 m/s, the voltages are kept at a constant values for 50 ms before the velocity is increased to its original value of 90 m/s. It can be seen in the figure that the observed TOFs are indeed almost identical to the ones recorded when the velocities are immediately returned to their original value. This measurement demonstrates that molecules can be trapped in the laboratory frame without further losses.

The observed decrease in signal for NH_3 and ND_3 at higher accelerations is greater than expected from simulations. We attribute the loss mainly to mechanical misalignments that lead to parametric amplification of the motion of the trapped molecules at low velocities. On inspection, it was noticed that one of the suspension bars was slightly displaced from its original position, which must have happened when the decelerator was placed in the vacuum chamber. Another loss mechanism comes from the fact that the phase space distribution of the packet exiting the conventional Stark decelerator is not perfectly matched to the acceptance of the traveling wave decelerator, and the alignment of the axis of the traveling wave decelerator to the axis of the Stark decelerator is not perfect. As a result, the trapped packet as a whole will perform a (damped) breathing and sloshing motion. These oscillations explain why the observed NH_3 TOF profile for deceleration to 60 m/s is wider and more intense than the TOF profile for guided molecules. Neither loss mechanism is fundamental, and we believe they can be eliminated in future work.

As discussed in Sec. 5.3, the acceptance of the traveling wave decelerator depends on the chirp that is applied to the waveform. This is illustrated by

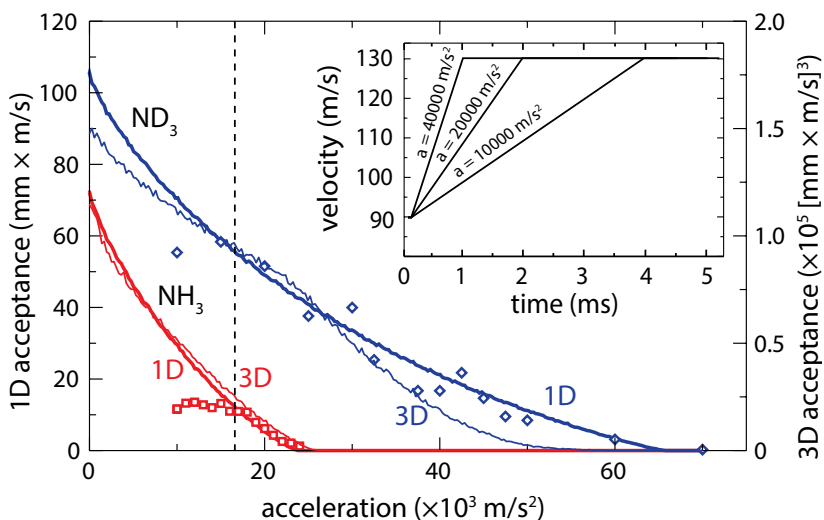


Figure 5.4 – Integrated time-of-flight distributions for NH_3 (squares) and ND_3 (diamonds) shown as a function of acceleration. The bold lines correspond to simulations of the 1D acceptance of the traveling wave decelerator, shown on the vertical axis on the left-hand side, while the thin lines correspond to simulations of the 3D acceptance of the traveling wave, shown on the vertical axis on the right-hand side. The NH_3 and ND_3 signals are scaled (by a different factor) to match the simulation. The inset displays the velocity of the traveling wave potential for three typical accelerations used in the experiment.

the measurements that are shown in Fig. 5.4. In this figure, the time-integrated signal of NH_3 (squares) and ND_3 (diamonds) molecules is plotted as a function of the applied acceleration. In these measurements, ammonia molecules are guided at 90 m/s for 5 mm before being accelerated to 130 m/s and then guided for the remaining length of the decelerator.

For comparison, the bold and thin solid lines shown in Fig. 5.4 correspond to simulations of the 1D and 3D acceptance of the traveling wave decelerator, respectively. The calculated acceptances are based on an average (i.e. static in the moving frame of the trap) potential well, rather than the true potential. The numbers on the right axis refer to the 3D acceptance, while the numbers on the left-hand axis refer to the 1D acceptance. The fact that the 1D and 3D simulations are almost the same, apart from a scaling factor, illustrates that the transverse acceptance is independent of the acceleration, i.e., the transverse motion of the molecules in the traveling wave decelerator is

largely decoupled from the longitudinal motion. The measurements for ND_3 and NH_3 have been scaled to match the simulations. As observed, at high acceleration the simulations predict the measurements quite well. At lower accelerations, however, the measurements are seen to reach a constant value which is consistent with the expected longitudinal acceptance of the conventional Stark decelerator at the used phase angle of 65 degrees [38]. At these accelerations the longitudinal acceptance of the traveling wave decelerator is larger than the longitudinal emittance of the packet exiting the Stark decelerator; i.e., all molecules exiting the conventional Stark decelerator are trapped in the traveling wave decelerator. Consequently, decelerations below roughly $18 \times 10^3 \text{ m/s}^2$ do not reduce the detected signal of NH_3 and ND_3 molecules. The dashed vertical line also shown in Fig. 5.4 indicates the maximum acceleration that was used in the measurements shown in Fig. 5.3. Note that, as in our measurements we do not determine an absolute value for the phase space acceptance of the decelerator, the similarity between the measurements and simulations should be considered as a consistency check only.

The position in the array of ring-shaped electrodes at which the molecules are brought to a standstill and statically trapped, is determined by the waveform and can be chosen at will. Figure 5.5 shows the NH_3 (squares) and ND_3 (diamonds) signal as a function of this position. The signal oscillates with a periodicity that corresponds to the spacing between adjacent rings; 1.5 mm equivalent to a phase difference of $\pi/4$. The signal is largest when the ammonia molecules are trapped in the plane of an electrode, and smallest when the trap center is located between two electrodes. The observed modulation is related to the variation in the radial confinement discussed in Sec. 5.3. For comparison, the solid lines in Fig. 5.5 show the trap depth for NH_3 and ND_3 in cm^{-1} (1 cm^{-1} corresponds to 1.4 K). The NH_3 and ND_3 signals are scaled (by different factors) to match the trap depth.

5.4.2 Phase jumps

As explained in Sec. 5.3, whenever the acceleration is changed, we rapidly sweep the phase of the waveform in order to correct for the resulting shift of the effective potential minimum. We refer to this sweep as a “phase jump”. In Fig. 5.6 we present measurements of molecules that are decelerated from 70 to 0 m/s using an acceleration of -15000 m/s^2 , trapped for 30 ms, and subsequently accelerated back to 70 m/s with the opposite acceleration and detected. The upper panel of Fig. 5.6 shows the NH_3 (squares) and ND_3 (diamonds) signal as a function of the (magnitude of the) phase jumps that are applied whenever the acceleration is changed. As expected, the required phase jump for optimal signal is much larger for NH_3 than for ND_3 . In fact, when no phase jump is applied almost no signal is observed for NH_3 , while for ND_3

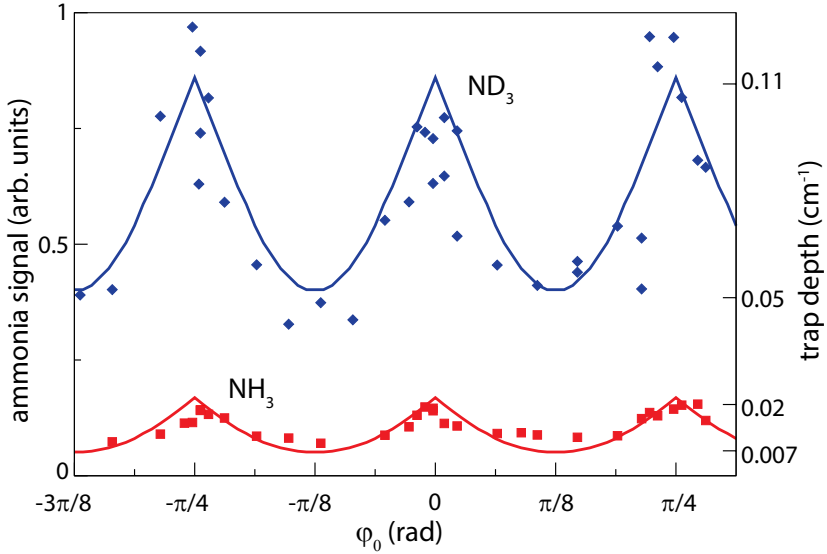


Figure 5.5 – NH_3 (squares) and ND_3 (diamonds) signal as a function of the position in the decelerator (expressed as a phase, ϕ_0) at which the molecules were trapped. When $\phi_0 = 0 \pmod{\pi/4}$, the center of the trap is located in the plane of a ring electrode while for $\phi_0 = \pi/8 \pmod{\pi/4}$ the trap minimum is located in the plane between two ring electrodes. The solid curves represent the trap depth for both species and are specified on the right axis. The NH_3 and ND_3 signals are scaled (by different factors) to match the trap depth.

the signal hardly changes. The solid curves in the upper panel of Fig. 5.6 show the result of 1D numerical simulations. Although the simulations seem to slightly overestimate the width of the observed peaks and predict slightly greater phase jumps, the maximum and overall shape match the experimental data fairly well. The discrepancies might be caused by the fact that the amplifiers are not able to follow the rapid sweep of the phase perfectly.

The lower panel of Fig. 5.6 shows the longitudinal acceleration as a function of the position along the beam axis for NH_3 and ND_3 molecules using a waveform amplitude of 5 kV. The electric field increases linearly away from the center of the trap resulting in a harmonic but shallow potential for NH_3 and a tight but very anharmonic potential for ND_3 . The horizontal line shows the acceleration that is used in the experiment. The crossings of this line with the acceleration curves, indicated by the dashed vertical lines, correspond to the positions of the minima of the effective potential.

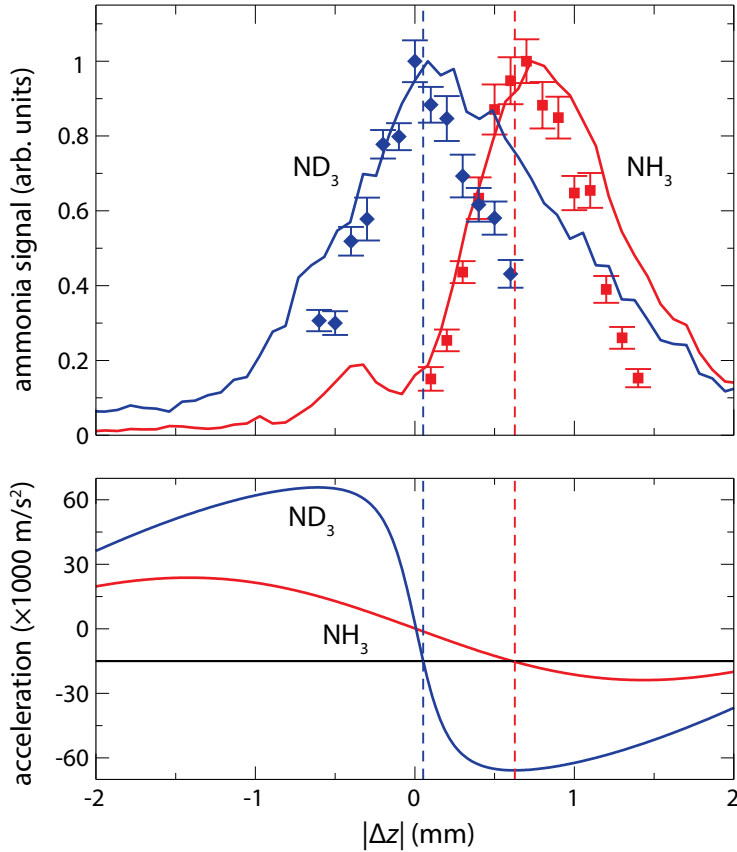


Figure 5.6 – The effect of phase jumps for an acceleration of $-15\,000 \text{ m/s}^2$ are illustrated in the upper panel for NH_3 (squares) and ND_3 (diamonds). Solid curves show the result of a 1D numerical simulation. The lower panel shows the longitudinal acceleration along the beam axis for NH_3 and ND_3 molecules using a waveform amplitude of 5 kV . The dashed vertical lines indicate the phase jumps that are derived from the acceleration curves in the lower panel.

5.4.3 Adiabatic cooling

As the voltages applied to the decelerator are generated by amplifying the output of an arbitrary wave generator using fast HV-amplifiers, we can change the depth (and shape) of the trap at will. This is illustrated by the measurements shown in Fig. 5.7. In these measurements, ND_3 molecules were decel-

erated using the conventional Stark decelerator at phase angles of 60 and 53 degrees and coupled into the traveling wave decelerator. The traveling wave decelerator is subsequently used to slow the ND_3 molecules to a standstill, trap them for a period of over 50 ms, accelerate them back to their initial velocity and launch them into the detection region. While the molecules are trapped, the voltages applied to the decelerator are ramped down in 2 ms, kept at a lower value for 10 ms and then ramped up again to 5 kV. Figure 5.7 shows the remaining ND_3 signal as a function of the reduced amplitude of the waveform for the two phase angles as indicated. Typical waveform amplitudes as a function of time are shown in the inset of Fig. 5.7. Lowering the voltages of the trap has two effects: (i) the trap frequency is lowered, adiabatically cooling the molecules; (ii) the trap depth is reduced, allowing the hottest molecules to escape the trap. The observed signal at a phase angle of 53 degrees is seen to drop more rapidly than that at a phase angle of 60 degrees. This is expected, as at lower phase angles a larger and hotter packet is loaded into the traveling wave decelerator. The hotter ensemble of ND_3 molecules initially fills the trap almost completely while the colder molecules occupy only a fraction of the trap. Consequently, the number of molecules in the hotter ensemble is reduced even when the voltages are lowered by a small amount. The solid and dashed lines also shown in Fig. 5.7 result from numerical simulations that assume initial temperatures of 30 mK or 100 mK respectively. Note that we use temperature here only as a convenient means to describe the distribution; the densities are too low to have thermalization on the timescales of the experiment. For comparison, Fig. 5.7 also shows measurements where the trap voltages are abruptly ($10 \mu\text{s}$) lowered. In this case no adiabatic cooling occurs and as a result the signal decreases more rapidly than when the voltages are ramped to lower voltages more slowly. The solid (30 mK) and dashed (100 mK) lines labeled as nonadiabatic show the results of a numerical simulation when the voltages are reduced abruptly. Similar measurements have been performed for NH_3 (not shown).

In Fig. 5.8, the number of molecules that remain trapped at 2 kV is shown as a function of the time used for lowering and increasing the voltages. The solid lines result from a 3D numerical simulation. The measurements confirm that the NH_3 and ND_3 molecules follow the trap adiabatically when the ramping times are longer than 1 ms. The time required for the molecules to follow the change in potential adiabatically is greater for NH_3 than it is for ND_3 due to the lower trap frequencies experienced by the former. Similar measurements have been performed on CH_3F molecules in a microstructured trap by Englert *et. al* [88].

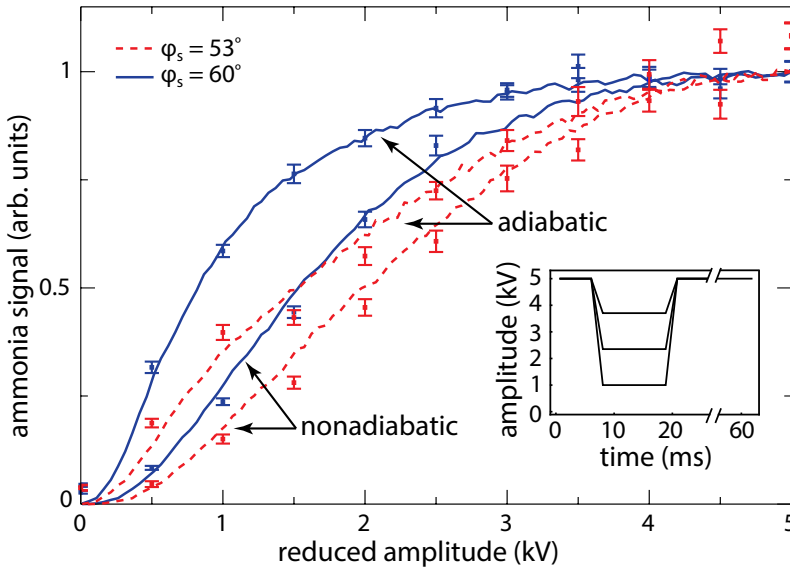


Figure 5.7 – Signal of trapped ND_3 molecules decelerated using a phase angle of 60 and 53 degrees as a function of the amplitude of the waveform when, after deceleration, the trap is slowly (labeled as adiabatic) or abruptly (labeled as nonadiabatic) reduced. The smooth curves also shown in the figure are simulations that assume an initial temperature of 30 (solid line) or 100 mK (dashed line) for the ensemble of trapped ND_3 molecules. The inset shows the amplitude of a number of typical waveforms as a function of time.

5.5 Conclusions

In this chapter we have demonstrated deceleration and trapping of NH_3 and ND_3 molecules in a traveling wave decelerator. The observed trapping times are limited to 100 ms by the current repetition rate of the experiment (10 Hz). The deceleration of a supersonic beam of ammonia molecules is performed in two steps; in the first step, the molecules are decelerated from 300 to 100 m/s using a conventional Stark decelerator, while in the second step, the traveling wave decelerator is used to remove the remaining kinetic energy from the molecules. The advantages of such a system are that the requirements imposed on the electronics of the traveling wave decelerator remain rather low, and that the combined length of both decelerators is only slightly above 1 m.

The motion of the molecules in the traveling wave decelerator is controlled completely by computer generated waveforms. As an example of the pos-

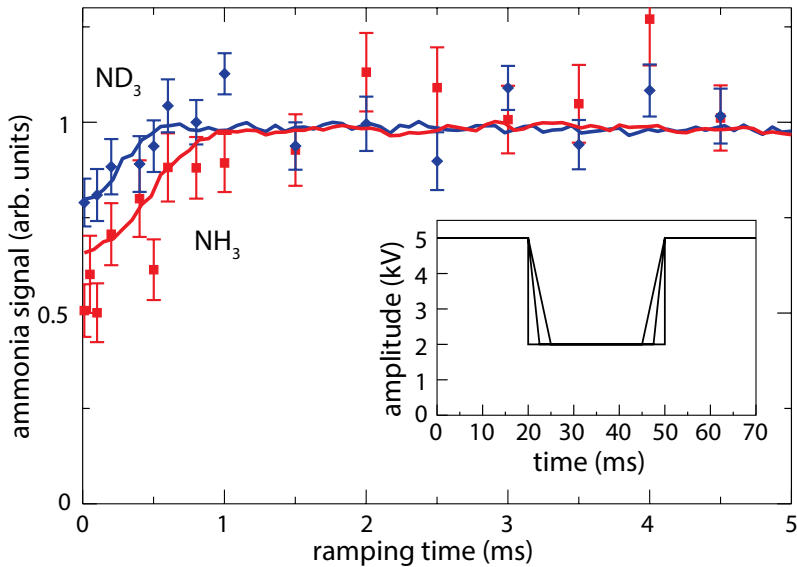


Figure 5.8 – Signal due to NH_3 (squares) and ND_3 (diamonds) molecules that remain trapped at 2 kV as a function of the time used for ramping the voltages. The solid lines show the result of a 3D numerical simulation that assumes a temperature of 30 or 100 mK for NH_3 and ND_3 , respectively. In the inset, typical waveform amplitudes are shown as a function of time.

sibilities offered by this control, we have adiabatically cooled the trapped molecules by lowering the amplitude of the waveforms. In Chapter 4, we demonstrated that the motion of the molecules in the trap can be excited by applying an small oscillatory force. The ability to control the voltages applied to the electrodes also offers the possibility to tailor the shape of the trap – for instance, changing it into a more box-like potential. This may prove useful for collisional and spectroscopic studies, as well as for the implementation of schemes to further cool the molecules such as sisyphus cooling [78] and evaporative cooling [79].

Chapter 6

Preparation of an ultra-cold sample of ammonia molecules for precision measurements*

We present experiments in which an ultra-cold sample of ammonia molecules is released from an electrostatic trap and recaptured after a variable time. It is shown that, by performing adiabatic cooling before releasing the molecules and adiabatic re-compression after they are recaptured, we are able to observe molecules even after more than 10 ms of free expansion. A coherent measurement performed during this time will have a statistical uncertainty that decreases approximately as the inverse of the square root of the expansion time. This offers interesting prospects for high-resolution spectroscopy and precision tests of fundamental physics theories.

6.1 Introduction

After eliminating more mundane broadening effects, the resolution of a spectroscopic measurement is ultimately limited by the time an atom or molecule interacts with the radiation field. In typical molecular beam experiments, this interaction time is limited to around 1 ms, resulting in a measured linewidth on the order of a kilohertz. The development of cooling techniques for atoms has led to a dramatic increase in the interaction times and hence the attained accuracy. Currently, atom and ion clocks reach accuracies on the order of 10^{-18} , allowing for tests of fundamental physics theories such as relativity [89], quantum electrodynamics [90] and the time-invariance of the fine-structure

*Based on M. Quintero-Pérez, T. E. Wall, S. Hoekstra, and H. L. Bethlem, *Journal of Molecular Spectroscopy*, vol. 300, pp. 112-115, Apr 2014.

constant [20] at an unprecedented level. It is anticipated that cooling techniques for molecules will lead to a similar increase in accuracy, allowing for more precise tests of time-reversal symmetry [24, 25] and the time-invariance of the proton-to-electron mass ratio [85], observation of parity violation [27] and weak interactions in chiral molecules [91]. Unfortunately, the cooling techniques for molecules demonstrated so far, such as Stark and Zeeman deceleration, buffer gas cooling, photo-association and laser cooling, have a poor efficiency (for recent review papers, see Refs. [22, 23, 66]). Therefore, although in proof-of-principle experiments prolonged interaction times have been achieved [37, 53], this was accomplished at the expense of a large decrease in signal. Hence, the Allan deviation – a measure of the statistical uncertainty of the experiment – was increased rather than decreased by using slow molecules. But the statistical uncertainty is not all that matters, usually the accuracy of experiments is limited by systematic effects rather than by the statistical uncertainty. As most systematic effects are proportional to the measured line-width [7], an experiment with a large Allan deviation but a small line-width is in some cases preferable over an experiment with a smaller Allan deviation but a large line-width. If the Allan deviation is too large, however, the required measurement times become unrealistically long.

Recently, our group has decelerated and trapped ammonia molecules using a series of rings to which oscillating voltages are applied (see Chapters 4 and 5). The advantage of such a traveling wave decelerator [72, 73, 74] is that molecules are confined in a genuine 3D trap throughout the deceleration process, which avoids the losses at low velocity that plague conventional Stark decelerators. The necessary voltages for the decelerator are generated by amplifying the output of an arbitrary wave generator using fast high voltage (HV) amplifiers, giving us great control over the trapping potential. In this chapter, we present measurements in which we adiabatically cool ND_3 molecules to sub-mK temperatures, release them by switching off the trap voltages completely, recapture them after a variable expansion time, re-compress and finally detect them. We discuss how this method could be used for obtaining high-resolution spectra.

6.2 Experimental Setup

Figure 6.1 shows a schematic view of our vertical molecular beam machine. A beam of ammonia molecules seeded in xenon is released into vacuum using a pulsed valve. This beam is decelerated from around 330 m/s to 90 m/s using a Stark decelerator consisting of 101 pairs of electrodes to which voltages of +10 and -10 kV are applied. The voltages are abruptly (< 100 ns) switched using four independent HV switches (Behlke HTS 151-03-GSM) that are trig-

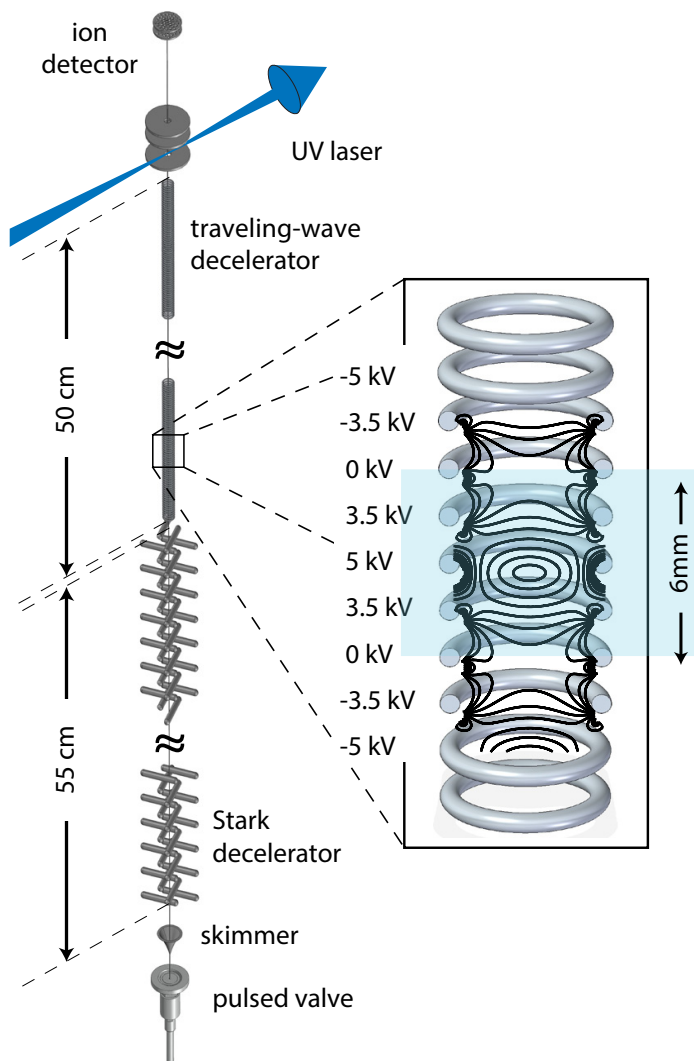


Figure 6.1 – Schematic view of the vertical molecular beam machine. A beam of molecules is decelerated and trapped using a combination of a Stark decelerator and a traveling wave decelerator. The inset shows the electric field magnitude inside the traveling wave decelerator (in steps of 2.5 kV/cm) with the voltages as indicated.

gered by a programmable delay generator. The traveling wave decelerator, which is mounted 24 mm above the last electrode pair of the first decelerator, consists of a series of 336 rings, each of which is attached to one of eight stainless steel rods to which voltages of up to ± 5 kV are applied. At any moment in time, the voltages applied to successive ring electrodes follow a sinusoidal pattern in z , where z is the position along the beam axis. These voltages create minima of electric field every 6 mm, which act as 3D traps for weak-field seeking molecules. By modulating the voltages sinusoidally in time, the traps are moved along the decelerator. A modulation frequency that is constant in time results in a trap that moves with a constant positive velocity along the molecular beam axis. A constant acceleration or deceleration can be achieved by applying a linear chirp to the frequency [73, 74]. The necessary voltages are generated by amplifying the output of an arbitrary wave generator (Wuntronic DA8150) using eight fast HV amplifiers (Trek 5/80). The ND₃ molecules are state-selectively ionized 20 mm above the traveling wave decelerator using a focused UV laser beam and counted by an ion detector. More details of the setup are given in Chapters 4 and 5. Compared to the setup used in our previous experiments, we have made a number of changes: (i) the General valve has been replaced by a Jordan valve; (ii) the distance between the decelerator and the detection region has been decreased from 40 mm to 20 mm; (iii) the suspension of the traveling wave decelerator has been altered such that the detection region is better pumped; (iv) the alignment of the ring electrodes with respect to each other as well as the alignment of the complete traveling wave decelerator with respect to the beam line has been improved.

6.3 Experimental Results

The upper panel of Fig. 6.2 shows the density of ND₃ molecules above the decelerator as a function of time when different waveforms are applied to the ring decelerator. In all cases, a packet of molecules is decelerated to 90 m/s using the conventional Stark decelerator and injected into the traveling wave decelerator at $t = 0$. The time-of-flight (TOF) trace labeled as '90' is recorded when a sinusoidal voltage with an amplitude of 5 kV and a constant frequency of 7.5 kHz is applied to the traveling wave decelerator. In this case, molecules at a velocity of 90 m/s are guided through the decelerator and arrive at the detection zone after 5.5 ms. The TOF traces that are labeled as '85' to '0' are recorded when the frequency is first linearly decreased to a certain value and subsequently increased to its original value. With these waveforms, molecules are decelerated to the indicated value (in m/s) before being accelerated back to their original velocity. Consequently, the molecules will spend a longer time in the decelerator and will arrive at the detection zone at later times. The

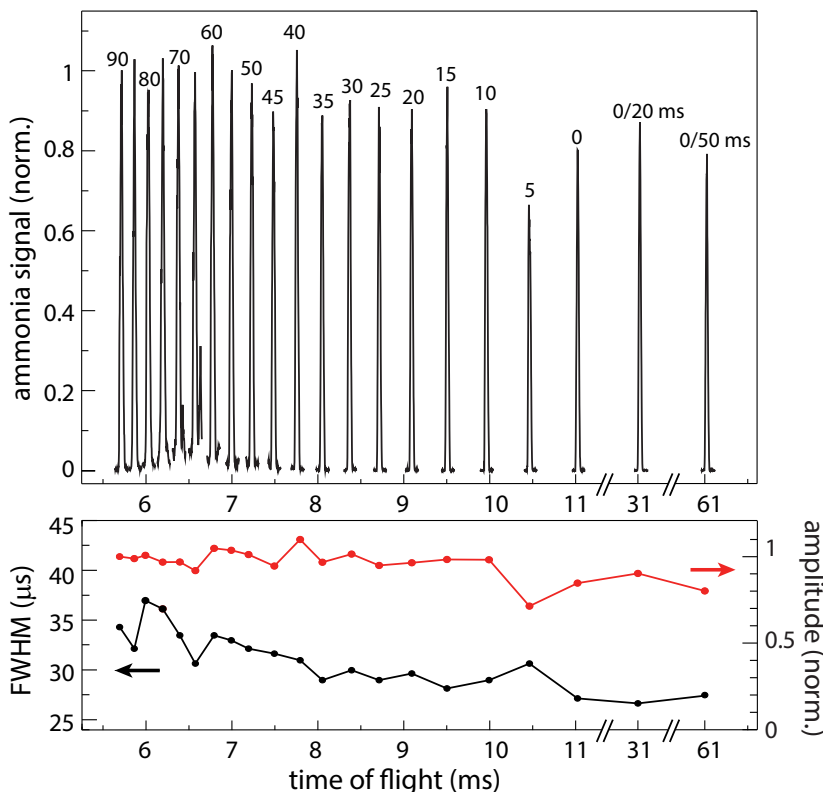


Figure 6.2 – Measured time-of-flight (TOF) profiles when ND_3 molecules are guided at 90 m/s, decelerated to 85-0 m/s and trapped for 20 and 50 ms before being accelerated back to 90 m/s and detected (upper graph). The lower graph shows the full-width at half-maximum, FWHM (black curve, left-hand side axis) and the amplitudes (red curve, right-hand side axis) of Gaussian fits to the TOF profiles.

TOF trace that is labeled as '0' corresponds to the situation in which molecules come to a complete standstill before being immediately accelerated back to 90 m/s and detected. As expected, the time the molecules spend in the decelerator is now approximately 2 times longer than when the molecules are guided. In these experiments the acceleration is changed from 0 m/s^2 , for guiding, to $\pm 17000 \text{ m/s}^2$, for deceleration and acceleration. Once the molecules come to a standstill, we can hold them for arbitrarily long times by keeping the voltages constant. The profiles that are labeled as '0/20' and '0/50' correspond to the situations in which molecules are trapped for 20 and 50 ms,

respectively.

The lower panel of Fig. 6.2 shows the full-width at half-maximum (FWHM) (black curve, left-hand side axis) and the amplitudes (red curve, right-hand side axis) of Gaussian fits to the TOF profiles. Since we detect molecules very close to the decelerator, the width of the TOF profiles mainly reflects the position spread of the guided molecules, i.e. the size of the trap in the z direction. The width of the TOF profile measured when the molecules are guided corresponds to a position spread of 3 mm. Deceleration of the molecules comes at the expense of the acceptance of the trap, which explains why the width of the TOF profiles decreases when the molecules are decelerated to lower velocities. The amplitudes of the Gaussian fits to the TOFs are normalized to that of the guided beam. As observed, the amplitude of the TOF profile measured after 50 ms of trapping is about 20% smaller than that of the guided beam. Note that in the experiments shown in Chapters 4 and 5 the ND_3 signal was reduced by 80%, which was attributed to mechanical misalignments in the traveling wave decelerator and a mismatch between the conventional Stark decelerator and the traveling wave decelerator. These issues have been resolved by realigning the decelerator. In addition, the various improvements have resulted in an increase of the signal of the guided molecules of a factor of 12.

It is observed in Fig. 6.2 that the amplitude of the TOF profile measured when molecules are decelerated to 5 m/s is smaller than expected while its width is larger than expected. We have repeated this measurement several times to ensure that it is not a statistical fluctuation, but this seems not to be the case. We attribute the observed heating to parametric amplification of the transverse motion when the transverse trapping frequency becomes similar to the inverse of the time that it takes molecules to move from one ring to the next. For ND_3 , strong, broad resonances are expected at 1.9 and 3 kHz, corresponding to a velocity of 2.8 and 4.5 m/s (see Chapter 4). These resonances do not lead to significant losses when the molecules are decelerated to a standstill, apparently because the resonance is passed sufficiently fast. When molecules are decelerated to 5 m/s, however, they spend a longer time near the resonance, leading to considerable heating.

As the waveforms applied to the decelerator are generated by a computer code and loaded into an arbitrary wave generator, we have complete control over the shape and depth of the trap. This is illustrated by the measurements presented in Fig. 6.3. In these measurements ND_3 molecules are again decelerated, trapped for a period of over 50 ms, and subsequently accelerated and detected. In this case, however, while the molecules are trapped, the voltages applied to the decelerator are ramped down in 10 ms, kept at a lower value for another 10 ms and then ramped back up to 5 kV over 10 ms (blue data points). Lowering the voltages of the trap has two effects: (i) the trap frequency is lowered, adiabatically cooling the molecules; (ii) the trap depth is

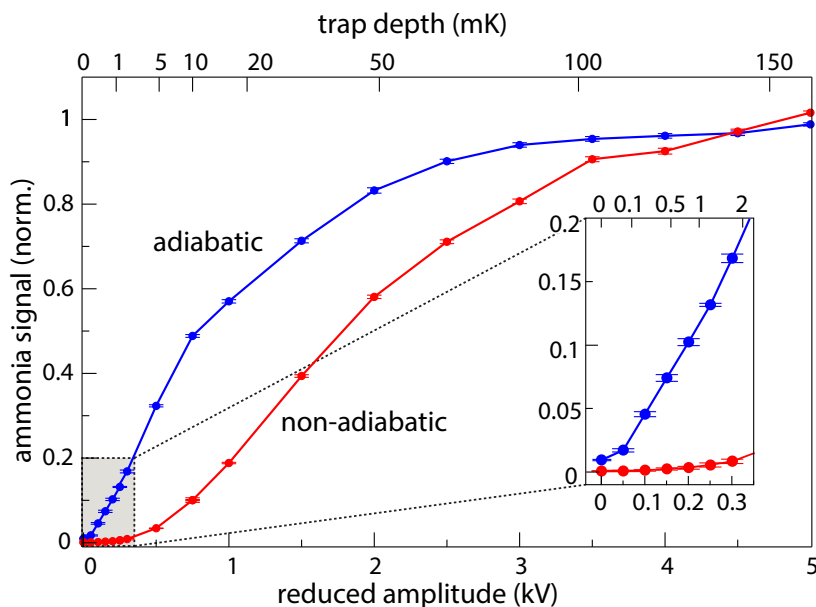


Figure 6.3 – Trapped ND_3 signal as a function of the amplitude of the waveform when, after deceleration and trapping, the voltages are slowly (blue curve labeled as ‘adiabatic’) or abruptly (red curve labeled as ‘non-adiabatic’) reduced to the indicated value. Each data point is the average of 600 shots; the error bars represent the one sigma statistical spread. The top axis shows the trap depth (in millikelvin) with this amplitude.

reduced, allowing the hottest molecules to escape the trap. The bottom axis of Fig. 6.3 shows the value to which the amplitude of the waveform is reduced, while the top axis shows the resulting trap depth in mK. For comparison, the signal is also shown when the trap voltages are abruptly ($10 \mu\text{s}$) lowered (red data points). In this case, no adiabatic cooling occurs and the signal decreases rapidly when the voltages are ramped down. The data presented in Fig. 6.3 is similar to that already presented in Chapters 4 and 5. However, as our signal is now much better than before, we can observe molecules even if the amplitude of the waveform is reduced to below 0.5 kV, as shown in the inset of the figure. It is seen that by reducing the trap depth to $200 \mu\text{K}$ we still have more than 5% of our signal left.

As discussed, the main motivation for our research on cold molecules is their potential for high-resolution spectroscopy. Ideally, one would like to perform spectroscopy on trapped molecules, for instance, by driving a tran-

sition between two states that have a similar Stark shift. However, a trap depth as low as $200 \mu\text{K}$ already corresponds to a Stark shift of 4 MHz. Thus, in order to measure this transition with high accuracy, the fractional difference between the Stark shifts of the levels involved should be very small. A more straight-forward approach is to switch off the trapping voltages completely.

In Fig. 6.4, we show the results of an experiment in which the trap is switched off for a variable period of time. The waveforms used in this experiment, shown in the inset of the figure, are similar to the ones used for obtaining the data of Fig. 6.3. In this case, however, after the voltages have been reduced to a certain value, V_{red} , we abruptly switch off the voltages for a variable period of time, Δt_{exp} . The y -axis shows the ion-current converted into the number of ions per shot on a logarithmic scale while the x -axis shows the expansion time in ms. The red, green and blue curves show the signal when the voltages are reduced to 2, 0.5 and 0.1 kV, respectively. The black curve is recorded when no adiabatic cooling has been performed. As observed, without adiabatically cooling, the signal is initially large, but it drops rapidly as the expansion time is increased. When the molecules are adiabatically cooled before they are released and adiabatically recompressed after they are recaptured, the initial signal is smaller but it decays more slowly as Δt_{exp} is increased. Consequently, molecules are detected even for expansion times over 10 ms. To understand the observations, it is important to realize that our signal is proportional to the number of molecules in the laser focus and *not* to the total number of molecules that are recaptured. For long expansion times, the number of molecules that are recaptured drops as $1/\Delta t_{\text{exp}}^3$; their density after re-compression, on the other hand, will stay approximately constant. As phase space density is conserved, this implies that the size of the trapped cloud shrinks. As our laser beam is tightly focused along the y and z -directions, but elongated along the x -direction, the signal is expected to be proportional to $1/\Delta t_{\text{exp}}$, as is indeed observed. The dashed black curve in Fig. 6.3 shows a $1/\Delta t_{\text{exp}}$ function to guide the eye.

For the sake of simplicity, we have chosen the voltage used for adiabatic cooling to be the same as the one used to recapture the molecules. However, it is probably better to optimize these separately – the voltage for adiabatic cooling should be chosen such that it satisfies the compromise between maximum cooling with a minimal loss of molecules, whereas the voltage applied to the trap when the molecules are recaptured should be chosen such that the phase space volume of the molecules after expansion is matched to the acceptance of the trap [22]. This implies that the optimal voltage used for recapturing the molecules actually depends on the expansion time.

The ability to observe molecules after switching off the trap voltages for times >10 ms is a promising prospect for future high-resolution experiments on molecules. The statistical uncertainty achieved in a spectroscopic experi-

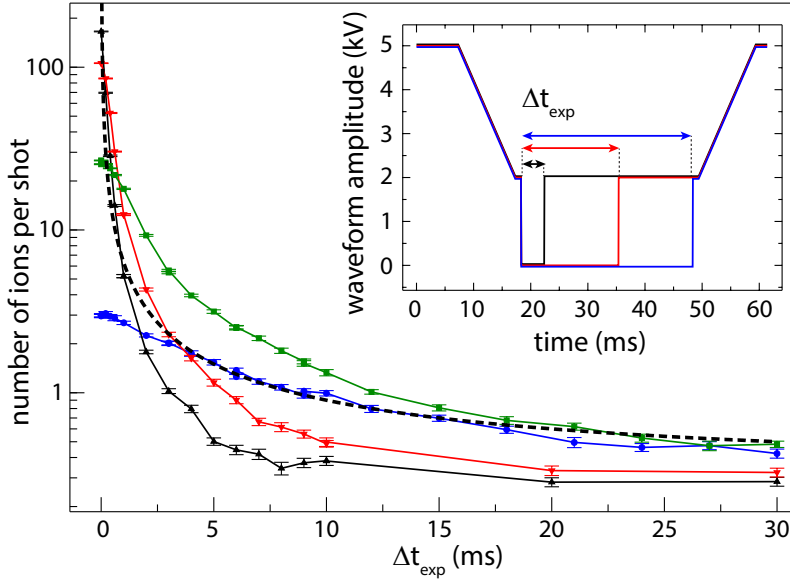


Figure 6.4 – Number of ND_3 molecules detected after release and recapturing as a function of the time that the molecules are allowed to expand. Example waveform amplitudes are shown in the inset. The black curve is recorded when no adiabatic cooling or re-compression is performed, while for recording the red, green and blue curves the waveform amplitudes are first slowly reduced to 2, 0.5 and 0.1 kV, respectively, before the molecules are released, and subsequently increased back from this value to 5 kV after the molecules have been recaptured. The dashed black curve shows a $1/\Delta t_{\text{exp}}$ function to guide the eye.

ment after a certain measuring time, τ , is given by the Allan deviation

$$\sigma_y(\tau) = \frac{1}{Q} \sqrt{\frac{\tau_c}{\tau N_c}}, \quad (6.1)$$

where $Q = f/\Delta f$ is the quality factor of the resonance, τ_c is the duration of one cycle, i.e., the inverse of the repetition frequency and N_c is the number of molecules that are detected per cycle. If the width of the transition is limited by the finite interaction time, Δt (i.e., $\Delta f \propto 1/\Delta t$), then the Allan deviation is proportional to $(\Delta t \sqrt{N_c})^{-1}$. If we performed a coherent measurement during the time that the molecules are freely expanding, we would expect from the data presented in Fig. 6.4 that the Allan deviation would decrease as $1/\sqrt{\Delta t_{\text{exp}}}$. We can check this conclusion by explicitly computing some

numbers; after an expansion time of 0.1, 1, 10 and 30 ms, we detected (at the optimal voltage settings and corrected for background signal) 117, 18, 1, and 0.2 ions per shot, respectively. This implies that the Allan deviation at 1, 10 and 30 ms is decreased by a factor of 4, 9 and 12, respectively, compared to the value at 0.1 ms. Thus, the increased interaction time indeed compensates the loss in signal.

6.4 Conclusion

As shown in Chapters 4 and 5, traveling wave decelerators are more efficient at low velocity and obviate the problem of loading molecules into a trap, that has led to large losses in earlier studies with Stark decelerators [38, 71]. Compared to the setup used in our previous experiments, we have made a number of improvements that have further reduced losses in the deceleration process. In the current experiments, the signal of molecules that are trapped for 50 ms is only 20% smaller than that of molecules that are guided by the traveling wave decelerator. Furthermore the guided signal was 12 times larger than that in our previous experiments. These improvements have allowed us to lower the voltages of the trap by a factor of 50, which corresponds to lowering the trap depth from 160 mK to 0.2 mK, while still having 5% of our original signal left. We have also performed experiments in which we switch off the trap completely and recapture the molecules more than 10 ms later – much longer than possible in a molecular beam machine of realistic size. We show that by performing adiabatic cooling before the molecules are released and adiabatic re-compression after the molecules are recaptured, the signal drops only as $1/\Delta t_{\text{exp}}$. This implies that the statistical error of a spectroscopic experiment performed during that time will decrease as $1/\sqrt{\Delta t_{\text{exp}}}$. Furthermore, the systematic errors are easier to control by the localised and well-controlled sample of cold molecules. The signal can be further increased by using larger rings, which will also improve the optical access. We are planning to perform precision measurements on the fundamental vibrations in ammonia using infrared lasers. As a first step, we plan to measure transitions in the $\nu_1 + \nu_3$ band of NH_3 near $1.5 \mu\text{m}$ [92].

Bibliography

- [1] W. Gerlach and O. Stern, "Der experimentelle Nachweis der Richtungsquantelung im Magnetfeld," *Zeitschrift für Physik*, vol. 9, no. 1, pp. 349–352, 1922.
- [2] I. I. Rabi, J. R. Zacharias, S. Millman, and P. Kusch, "A new method of measuring nuclear magnetic moment," *Phys. Rev.*, vol. 53, pp. 318–318, Feb 1938.
- [3] I. I. Rabi, S. Millman, P. Kusch, and J. R. Zacharias, "The molecular beam resonance method for measuring nuclear magnetic moments.," *Phys. Rev.*, vol. 55, pp. 526–535, Mar 1939.
- [4] N. F. Ramsey, "Experiments with separated oscillatory fields and hydrogen masers," *Nobel Lectures*, 1989.
- [5] W. Thomson and P. G. Tait, *Treatise on Natural Philosophy*, vol. 1 of 1. Cambridge, England: Cambridge University Press, 2 ed., 1879. page 227.
- [6] W. Ketterle and D. E. Pritchard, "Atom cooling by time-dependent potentials," *Phys. Rev. A*, vol. 46, pp. 4051–4054, Oct 1992.
- [7] A. Amy-Klein, L. Constantin, C. Daussy, C. Chardonnet, R. Butcher, P. Durand, and G. Nogues, "Slow molecule detection or Ramsey fringes in two-photon spectroscopy: which is better for high-resolution spectroscopy and metrology?," *Opt. Express*, vol. 4, pp. 67–76, Jan 1999.
- [8] N. F. Ramsey, *Molecular Beams*. Oxford University Press, 1956.
- [9] T. Hänsch and A. Schawlow, "Cooling of gases by laser radiation," *Optics Communications*, vol. 13, no. 1, pp. 68 – 69, 1975.
- [10] A. Ashkin, "Trapping of atoms by resonance radiation pressure," *Phys. Rev. Lett.*, vol. 40, pp. 729–732, Mar 1978.

- [11] S. Chu, L. Hollberg, J. E. Bjorkholm, A. Cable, and A. Ashkin, "Three-dimensional viscous confinement and cooling of atoms by resonance radiation pressure," *Phys. Rev. Lett.*, vol. 55, pp. 48–51, Jul 1985.
- [12] A. Aspect, E. Arimondo, R. Kaiser, N. Vansteenkiste, and C. Cohen-Tannoudji, "Laser cooling below the one-photon recoil energy by velocity-selective coherent population trapping," *Phys. Rev. Lett.*, vol. 61, pp. 826–829, Aug 1988.
- [13] M. A. Kasevich, E. Riis, S. Chu, and R. G. DeVoe, "rf spectroscopy in an atomic fountain," *Phys. Rev. Lett.*, vol. 63, pp. 612–615, Aug 1989.
- [14] S. Bize, P. Laurent, M. Abgrall, H. Marion, I. Maksimovic, L. Cacciapuoti, J. Grünert, C. Vian, F. P. dos Santos, P. Rosenbusch, P. Lemonde, G. Santarelli, P. Wolf, A. Clairon, A. Luiten, M. Tobar, and C. Salomon, "Cold atom clocks and applications," *J. Phys. B.*, vol. 38, no. 9, p. S449, 2005.
- [15] S. A. Diddams, J. C. Bergquist, S. R. Jefferts, and C. W. Oates, "Standards of time and frequency at the outset of the 21st century," *Science*, vol. 306, no. 5700, pp. 1318–1324, 2004.
- [16] J. Aarons, "Primary frequency standards, NIST F1 and F2," www.nist.gov/pml/div688/grp50/primary-frequency-standards.cfm 2009.
- [17] H. Katori, K. Hashiguchi, E. Y. Il'inova, and V. D. Ovsiannikov, "Magic wavelength to make optical lattice clocks insensitive to atomic motion," *Phys. Rev. Lett.*, vol. 103, p. 153004, Oct 2009.
- [18] B. J. Bloom, T. L. Nicholson, J. R. Williams, S. L. Campbell, M. Bishof, X. Zhang, W. Zhang, S. L. Bromley, and J. Ye, "An optical lattice clock with accuracy and stability at the 10^{-18} level," *Nature*, vol. 506, pp. 71–75, Feb 2014.
- [19] T. Rosenband, P. O. Schmidt, D. B. Hume, W. M. Itano, T. M. Fortier, J. E. Stalnaker, K. Kim, S. A. Diddams, J. C. J. Koelemeij, J. C. Bergquist, and D. J. Wineland, "Observation of the $^1S_0 \rightarrow ^3P_0$ clock transition in $^{27}\text{Al}^+$," *Phys. Rev. Lett.*, vol. 98, p. 220801, May 2007.
- [20] T. Rosenband, D. B. Hume, P. O. Schmidt, C. W. Chou, A. Brusch, L. Lorini, W. H. Oskay, R. E. Drullinger, T. M. Fortier, J. E. Stalnaker, S. A. Diddams, W. C. Swann, N. R. Newbury, W. M. Itano, D. J. Wineland, and J. C. Bergquist, "Frequency ratio of Al^+ and Hg^+ single-ion optical clocks; metrology at the 17th decimal place," *Science*, vol. 319, no. 5871, pp. 1808–1812, 2008.

-
- [21] C. W. Chou, D. B. Hume, J. C. J. Koelemeij, D. J. Wineland, and T. Rosenband, "Frequency comparison of two high-accuracy Al^+ optical clocks," *Phys. Rev. Lett.*, vol. 104, p. 070802, Feb 2010.
- [22] S. Y. T. van de Meerakker, H. L. Bethlem, N. Vanhaecke, and G. Meijer, "Manipulation and control of molecular beams," *Chem. Rev.*, vol. 112, no. 9, pp. 4828–4878, 2012.
- [23] M. Lemeshko, R. V. Krems, J. M. Doyle, and S. Kais, "Manipulation of molecules with electromagnetic fields," *Molecular Physics*, vol. 111, no. 12-13, pp. 1648–1682, 2013.
- [24] The ACME Collaboration, J. Baron, W. C. Campbell, D. DeMille, J. M. Doyle, G. Gabrielse, Y. V. Gurevich, P. W. Hess, N. R. Hutzler, E. Kirilov, I. Kozyryev, B. R. OLeary, C. D. Panda, M. F. Parsons, E. S. Petrik, B. Spaun, A. C. Vutha, and A. D. West, "Order of magnitude smaller limit on the electric dipole moment of the electron," *Science*, vol. 343, no. 6168, pp. 269–272, 2014.
- [25] J. J. Hudson, D. M. Kara, I. J. Smallman, B. E. Sauer, M. R. Tarbutt, and E. A. Hinds, "Improved measurement of the shape of the electron," *Nature*, vol. 473, pp. 493–6, May 2011.
- [26] M. R. Tarbutt, J. J. Hudson, B. E. Sauer, and E. A. Hinds, "Prospects for measuring the electric dipole moment of the electron using electrically trapped polar molecules," *Farad. Disc.*, vol. 142, p. 37, 2009.
- [27] D. DeMille, S. B. Cahn, D. Murphree, D. A. Rahmlow, and M. G. Kozlov, "Using molecules to measure nuclear spin-dependent parity violation," *Phys. Rev. Lett.*, vol. 100, pp. 1–4, Jan. 2008.
- [28] P. Jansen, L.-H. Xu, I. Kleiner, W. Ubachs, and H. L. Bethlem, "Methanol as a sensitive probe for spatial and temporal variations of the proton-to-electron mass ratio," *Phys. Rev. Lett.*, vol. 106, p. 100801, Mar 2011.
- [29] H. L. Bethlem and W. Ubachs, "Testing the time-invariance of fundamental constants using microwave spectroscopy on cold diatomic radicals," *Faraday Discuss.*, vol. 142, pp. 25–36, 2009.
- [30] H. L. Bethlem, M. Kajita, B. Sartakov, G. Meijer, and W. Ubachs, "Prospects for precision measurements on ammonia molecules in a fountain," *Eur. Phys. J. Spec. Top.*, vol. 163, pp. 55–69, 2008.
- [31] E. S. Shuman, J. F. Barry, and D. DeMille, "Laser cooling of a diatomic molecule," *Nature*, vol. 467, pp. 820–823, Oct 2010.

- [32] J. F. Barry, E. S. Shuman, E. B. Norrgard, and D. DeMille, "Laser radiation pressure slowing of a molecular beam," *Phys. Rev. Lett.*, vol. 108, p. 103002, Mar 2012.
- [33] M. T. Hummon, M. Yeo, B. K. Stuhl, A. L. Collopy, Y. Xia, and J. Ye, "2D magneto-optical trapping of diatomic molecules," *Phys. Rev. Lett.*, vol. 110, p. 143001, Apr 2013.
- [34] S. Y. T. van de Meerakker, H. L. Bethlem, and G. Meijer, "Taming molecular beams," *Nat. Phys.*, vol. 4, pp. 595–602, Aug. 2008.
- [35] C. H. Townes and A. L. Schawlow, *Microwave Spectroscopy*. Dover Publications, 1975.
- [36] P. Helminger, F. C. De Lucia, W. Gordy, H. W. Morgan, and P. A. Staats, "Microwave rotation-inversion spectrum of NT_3 ," *Phys. Rev. A*, vol. 9, pp. 12–16, Jan 1974.
- [37] J. van Veldhoven, J. Küpper, H. L. Bethlem, B. Sartakov, A. J. A. van Roij, and G. Meijer, "Decelerated molecular beams for high-resolution spectroscopy," *Eur. Phys. J. D*, vol. 31, pp. 337–349, 2004.
- [38] H. L. Bethlem, F. M. H. Crompvoets, R. T. Jongma, S. Y. T. van de Meerakker, and G. Meijer, "Deceleration and trapping of ammonia using time-varying electric fields," *Phys. Rev. A*, vol. 65, p. 053416, May 2002.
- [39] P. Jansen, *Polyatomic molecules for probing a possible variation of the proton-to-electron mass ratio*. PhD thesis, VU University Amsterdam, 2013.
- [40] H. L. Bethlem, G. Berden, and G. Meijer, "Decelerating neutral dipolar molecules," *Phys. Rev. Lett.*, vol. 83, pp. 1558–1561, Aug 1999.
- [41] F. M. Crompvoets, H. L. Bethlem, R. T. Jongma, and G. Meijer, "A prototype storage ring for neutral molecules," *Nature*, vol. 411, pp. 174–176, May 2001.
- [42] S. Y. T. van de Meerakker, N. Vanhaecke, H. L. Bethlem, and G. Meijer, "Transverse stability in a stark decelerator," *Phys. Rev. A*, vol. 73, p. 023401, Feb 2006.
- [43] H. L. Bethlem, G. Berden, F. M. Crompvoets, R. T. Jongma, A. J. A. van Roij, and G. Meijer, "Electrostatic trapping of ammonia molecules," *Nature*, vol. 406, pp. 491–494, Aug 2000.

-
- [44] L. P. Parazzoli, N. J. Fitch, P. S. Żuchowski, J. M. Hutson, and H. J. Lewandowski, "Large effects of electric fields on atom-molecule collisions at millikelvin temperatures," *Phys. Rev. Lett.*, vol. 106, p. 193201, May 2011.
- [45] P. A. Franken, A. E. Hill, C. W. Peters, and G. Weinreich, "Generation of optical harmonics," *Phys. Rev. Lett.*, vol. 7, pp. 118–119, Aug 1961.
- [46] G. H. C. New and J. F. Ward, "Optical third-harmonic generation in gases," *Phys. Rev. Lett.*, vol. 19, pp. 556–559, Sep 1967.
- [47] K.S.E Eikema and W. Ubachs, "Precision laser spectroscopy in the Extreme Ultraviolet," in *Handbook of Spectroscopy* (M. Quack and F. Merkt, eds.).
- [48] R. Hilbig and R. Wallenstein, "Tunable vuv radiation generated by two-photon resonant frequency mixing in xenon," *IEEE Journal of Quantum Electronics*, vol. 19, no. 2, pp. 194–201, 1983.
- [49] G. Hilber, A. Lago, and R. Wallenstein, "Broadly tunable vacuum-ultraviolet/extreme-ultraviolet radiation generated by resonant third-order frequency conversion in krypton," *J. Opt. Soc. Am. B*, vol. 4, pp. 1753–1764, Nov 1987.
- [50] J. P. Marangos, N. Shen, H. Ma, M. H. R. Hutchinson, and J. P. Connerade, "Broadly tunable vacuum-ultraviolet radiation source employing resonant enhanced sum-difference frequency mixing in krypton," *J. Opt. Soc. Am. B*, vol. 7, pp. 1254–1263, Jul 1990.
- [51] M. N. R. Ashfold, R. N. Dixon, N. Little, R. J. Stickland, and C. M. Western, "The \tilde{B}^1E'' state of ammonia: sub-doppler spectroscopy at vacuum ultraviolet energies," *J. Chem. Phys.*, vol. 89, no. 4, pp. 1754–1761, 1988.
- [52] H. L. Bethlem, M. Kajita, B. Sartakov, G. Meijer, and W. Ubachs, "Prospects for precision measurements on ammonia molecules in a fountain," *Eur. Phys. J. Spec. Top.*, vol. 163, pp. 55–69, 2008.
- [53] E. R. Hudson, H. J. Lewandowski, B. C. Sawyer, and J. Ye, "Cold molecule spectroscopy for constraining the evolution of the fine structure constant," *Phys. Rev. Lett.*, vol. 96, pp. 1–4, Apr. 2006.
- [54] A. T. J. B. Eppink and D. H. Parker, "Velocity map imaging of ions and electrons using electrostatic lenses: Application in photoelectron and photofragment ion imaging of molecular oxygen," *Review of Scientific Instruments*, vol. 68, no. 9, 1997.

- [55] D. W. Chandler and P. L. Houston, "Two-dimensional imaging of state-selected photodissociation products detected by multiphoton ionization," *J. Chem. Phys.*, vol. 87, no. 2, p. 1445, 1987.
- [56] B. J. Whitaker, *Imaging in Molecular Dynamics: Technology and Applications*. Cambridge: Cambridge University Press, 2003.
- [57] M. L. Lipciuc, J. B. Buijs, and M. H. M. Janssen, "High resolution slice imaging of a molecular speed distribution.," *Phys. Chem. Chem. Phys.*, vol. 8, pp. 219–23, Jan. 2006.
- [58] C. E. Heiner, H. L. Bethlem, and G. Meijer, "Molecular beams with a tunable velocity," *Phys. Chem. Chem. Phys.*, vol. 8, pp. 2666–2676, 2006.
- [59] H. L. Offerhaus, C. Nicole, F. Lepine, C. Bordas, F. Rosca-Pruna, and M. J. J. Vrakking, "A magnifying lens for velocity map imaging of electrons and ions," *Rev. Sci. Instrum.*, vol. 72, no. 8, p. 3245, 2001.
- [60] D. A. Dahl, J. E. Delmore, and A. D. Appelhans, "SIMION PC/PS2 electrostatic lens design program," *Rev. Sci. Instrum.*, vol. 61, no. 1, p. 607, 1990.
- [61] B. Y. Chang, R. C. Hoetzlein, J. A. Mueller, J. D. Geiser, and P. L. Houston, "Improved two-dimensional product imaging: The real-time ion-counting method," *Rev. Sci. Instrum.*, vol. 69, no. 4, pp. 1665–1670, 1998.
- [62] W. E. Conaway, R. J. Morrison, and R. N. Zare, "Vibrational state selection of ammonia ions using resonant 2 + 1 multiphoton ionization," *Chem. Phys. Lett.*, vol. 113, no. 5, pp. 429 – 434, 1985.
- [63] R. Ruede, H. Troxler, C. Beglinger, and M. Jungen, "The dissociation energies of the positive ions NH_3^+ , NF_3^+ , PH_3^+ , PF_3^+ and PCl_3^+ ," *Chem. Phys. Lett.*, vol. 203, no. 56, pp. 477 – 481, 1993.
- [64] C. E. Heiner, D. Carty, G. Meijer, and H. L. Bethlem, "A molecular synchrotron," *Nat. Phys.*, vol. 3, pp. 115–118, Jan. 2007.
- [65] P. C. Zieger, S. Y. T. van de Meerakker, C. E. Heiner, H. L. Bethlem, A. J. A. van Roij, and G. Meijer, "Multiple packets of neutral molecules revolving for over a mile," *Phys. Rev. Lett.*, vol. 105, pp. 1–4, Oct. 2010.
- [66] L. D. Carr, D. DeMille, R. V. Krems, and J. Ye, "Cold and ultracold molecules: science, technology and applications," *New J. Phys.*, vol. 11, no. 5, p. 055049, 2009.

-
- [67] S. D. Hogan, M. Motsch, and F. Merkt, "Deceleration of supersonic beams using inhomogeneous electric and magnetic fields," *Phys. Chem. Chem. Phys.*, vol. 13, pp. 18705–18723, 2011.
- [68] E. Narevicius and M. G. Raizen, "Toward cold chemistry with magnetically decelerated supersonic beams," *Chemical Reviews*, vol. 112, no. 9, pp. 4879–4889, 2012.
- [69] H. L. Bethlem, G. Berden, A. J. A. van Roij, F. M. H. Crompvoets, and G. Meijer, "Trapping neutral molecules in a traveling potential well," *Phys. Rev. Lett.*, vol. 84, pp. 5744–5747, Jun 2000.
- [70] B. C. Sawyer, B. L. Lev, E. R. Hudson, B. K. Stuhl, M. Lara, J. L. Bohn, and J. Ye, "Magneto-electrostatic trapping of ground state OH molecules," *Phys. Rev. Lett.*, vol. 98, p. 253002, Jun 2007.
- [71] J. J. Gilijamse, S. Hoekstra, N. Vanhaecke, S. Y. T. van de Meerakker, and G. Meijer, "Loading stark-decelerated molecules into electrostatic quadrupole traps," *Eur. Phys. J. D*, vol. 57, pp. 33–41, 2010.
- [72] S. A. Meek, H. L. Bethlem, H. Conrad, and G. Meijer, "Trapping molecules on a chip in traveling potential wells," *Phys. Rev. Lett.*, vol. 100, p. 153003, Apr 2008.
- [73] A. Osterwalder, S. A. Meek, G. Hammer, H. Haak, and G. Meijer, "Deceleration of neutral molecules in macroscopic traveling traps," *Phys. Rev. A*, vol. 81, p. 051401, May 2010.
- [74] S. A. Meek, M. F. Parsons, G. Heyne, V. Platschkowski, H. Haak, G. Meijer, and A. Osterwalder, "A traveling wave decelerator for neutral polar molecules," *Rev. Sci. Instrum.*, vol. 82, no. 9, p. 093108, 2011.
- [75] N. E. Bulleid, R. J. Hendricks, E. A. Hinds, S. A. Meek, G. Meijer, A. Osterwalder, and M. R. Tarbutt, "Traveling-wave deceleration of heavy polar molecules in low-field-seeking states," *Phys. Rev. A*, vol. 86, p. 021404, Aug 2012.
- [76] J. van den Berg, S. Turkesteen, E. Prinsen, and S. Hoekstra, "Deceleration and trapping of heavy diatomic molecules using a ring-decelerator," *Eur. Phys. J. D*, vol. 66, no. 9, p. 235, 2012.
- [77] L. D. Landau and E. M. Lifshitz, *Mechanics*, vol. 1. Pergamon, Oxford, 1976.

- [78] M. Zeppenfeld, B. Englert, R. Glockner, A. Prehn, M. Mielenz, C. Sommer, L. D. van Buuren, M. Motsch, and G. Rempe, "Sisyphus cooling of electrically trapped polyatomic molecules," *Nature*, vol. 491, pp. 570–573, Nov 2012.
- [79] B. K. Stuhl, M. T. Hummon, M. Yeo, G. Quemener, J. L. Bohn, and J. Ye, "Evaporative cooling of the dipolar hydroxyl radical," *Nature*, vol. 492, pp. 396–400, Dec 2012.
- [80] S. Ospelkaus, K.-K. Ni, D. Wang, M. H. G. de Miranda, B. Neyenhuis, G. Qumner, P. S. Julienne, J. L. Bohn, D. S. Jin, and J. Ye, "Quantum-state controlled chemical reactions of ultracold potassium-rubidium molecules," *Science*, vol. 327, no. 5967, pp. 853–857, 2010.
- [81] M. Kirste, X. Wang, H. C. Schewe, G. Meijer, K. Liu, A. van der Avoird, L. M. C. Janssen, K. B. Gubbels, G. C. Groenenboom, and S. Y. T. van de Meerakker, "Quantum-state resolved bimolecular collisions of velocity-controlled oh with no radicals," *Science*, vol. 338, no. 6110, pp. 1060–1063, 2012.
- [82] D. DeMille, "Quantum computation with trapped polar molecules," *Phys. Rev. Lett.*, vol. 88, p. 067901, Jan 2002.
- [83] A. Micheli, G. K. Brennen, and P. Zoller, "A toolbox for lattice-spin models with polar molecules," *Nat Phys*, vol. 2, pp. 341–347, 2006.
- [84] A. Andre, D. DeMille, J. M. Doyle, M. D. Lukin, S. E. Maxwell, P. Rabl, R. J. Schoelkopf, and P. Zoller, "A coherent all-electrical interface between polar molecules and mesoscopic superconducting resonators," *Nat Phys*, vol. 2, pp. 636–642, 2006.
- [85] A. Shelkovernikov, R. J. Butcher, C. Chardonnet, and A. Amy-Klein, "Stability of the proton-to-electron mass ratio," *Phys. Rev. Lett.*, vol. 100, p. 150801, Apr 2008.
- [86] S. Truppe, R. J. Hendricks, S. K. Tokunaga, H. J. Lewandowski, M. G. Kozlov, C. Henkel, E. A. Hinds, and M. R. Tarbutt, "A search for varying fundamental constants using hertz-level frequency measurements of cold CH molecules," *Nat Commun*, vol. 4, 2006.
- [87] B. Sawyer. PhD thesis, University of Colorado, 2010.
- [88] B. G. U. Englert, M. Mielenz, C. Sommer, J. Bayerl, M. Motsch, P. W. H. Pinkse, G. Rempe, and M. Zeppenfeld, "Storage and adiabatic cooling of polar molecules in a microstructured trap," *Phys. Rev. Lett.*, vol. 107, p. 263003, Dec 2011.

- [89] C. W. Chou, D. B. Hume, T. Rosenband, and D. J. Wineland, "Optical clocks and relativity," *Science*, vol. 329, no. 5999, pp. 1630–1633, 2010.
- [90] T. W. Hänsch, "Nobel lecture: Passion for precision," *Rev. Mod. Phys.*, vol. 78, pp. 1297–1309, Nov 2006.
- [91] C. Daussy, T. Marrel, A. Amy-Klein, C. T. Nguyen, C. J. Bordé, and C. Chardonnet, "Limit on the parity nonconserving energy difference between the enantiomers of a chiral molecule by laser spectroscopy," *Phys. Rev. Lett.*, vol. 83, pp. 1554–1557, Aug 1999.
- [92] G. Berden, R. Peeters, and G. Meijer, "Cavity-enhanced absorption spectroscopy of the 1.5 μm band system of jet-cooled ammonia," *Chemical Physics Letters*, vol. 307, no. 3-4, pp. 131–138, 1999.

Publications

- *Velocity map imaging of a slow beam of ammonia molecules inside a quadrupole guide*
Marina Quintero-Pérez, Paul Jansen and Hendrick L. Bethlem
Physical Chemistry Chemical Physics **14**, 9630-9635 (2012).
- *Static trapping of polar molecules in a traveling wave decelerator*
Marina Quintero-Pérez, Paul Jansen, Thomas E. Wall, Joost E. van den Berg, Steven Hoekstra and Hendrick L. Bethlem
Physical Review Letters **110**, 133003 (2013).
- *Deceleration and trapping of ammonia molecules in a traveling wave decelerator*
Paul Jansen, Marina Quintero-Pérez, Thomas E. Wall, Joost E. van den Berg, Steven Hoekstra and Hendrick L. Bethlem
Physical Review A **88**, 043424 (2013).
- *Preparation of an ultra-cold sample of ammonia molecules for precision measurements*
Marina Quintero-Pérez, Thomas E. Wall, Steven Hoekstra and Hendrick L. Bethlem
Journal of Molecular Spectroscopy **300**, 112-115 (2014).

Summary

"Physics is really nothing more than a search for ultimate simplicity, but so far all we have is a kind of elegant messiness."

– Bill Bryson, *A Short History of Nearly Everything*

In my opinion, the main task of physics research is to delve deeper into that elegant messiness and try to unravel it a little more, carefully deciphering the code of Nature until it can be presented to our minds with ultimate simplicity. To this end, a wise approach is to measure or observe physical phenomena that are already known but with a new perspective, more detailed and scrupulous, in such a way that a whole new level of information can be extracted. High-resolution spectroscopic measurements are a very powerful tool used by experimental groups around the world for obtaining new information from an experiment. The task is mainly to obtain as much information as possible about the structure of atoms and molecules and the physics behind them by making them interact with radiation (light) that is contained inside a cavity. A beam of molecules will cross this cavity and will be interrogated by the radiation during the time they spend inside it. If the molecules move very fast, the time spent inside the cavity, and therefore the time they are interrogated, will be short, and a limited amount of information can be extracted. To make this time longer, the solution used in this thesis is to reduce the velocity of the molecules by manipulating them with electric fields. Very slow molecules will spend a much longer time crossing the cavity and being interrogated by the radiation, and therefore a greater amount of information can be obtained. With this technique, even fundamental physics theories to which certain atomic or molecular species are specially sensitive can be tested.

The main experimental problem with the achievement of long interaction times is that particles spread out over time due to their temperature and velocities, causing a decrease in density and, hence, a substantial decrease of the number of particles that reach the detector. This directly decreases the resolution of Ramsey spectroscopy, technique which we ultimately want to perform

with slow molecules. To achieve the highest resolution, the target particles must be cooled so they don't spread out during the measurement. Cooling techniques that are effective for manipulating atoms, like laser cooling, are highly inefficient or impossible in the case of molecules due to the complexity of their energy level structure. Hence, other techniques for manipulating and cooling molecules are needed. A method that has been proven very efficient is to exploit the Stark effect of a molecule using time-varying inhomogeneous electric fields. When a polar molecule is placed in an inhomogeneous electric field, the uneven distribution of charges gives rise to a net force that can be used to manipulate its overall velocity, temperature and trajectory.

The work shown in this thesis is in summary focused on obtaining a signal of slow molecules that is as large as possible on the detector to be able to reach unprecedented interaction times in molecules. Chapter 1 introduces the importance of slow atomic and molecular species for high-resolution spectroscopic measurements and gives an overview of our efforts on building a molecular fountain to measure the inversion frequency of ammonia. In the fountain, molecules would fly upwards, falling back under gravity and allowing for interaction times in the order of the second. Unfortunately, the low efficiency of usual Stark deceleration techniques did not allow for enough density of slow molecules to be able to see them falling back. In Chapter 2, we try to compensate for the low densities by testing whether a new ionization scheme for the molecules would be more efficient, giving us the possibility to detect more of them. This new scheme uses vacuum-ultraviolet light instead of the ultraviolet light used in the previous scheme. In Chapter 3, we build an unique ion lens that is able to separate the ions corresponding to different velocities of the molecules onto a CCD camera, giving us the possibility to eliminate the background of fast molecules from our signal of slow molecules. Chapters 4 and 5 show the implementation and testing of a new kind of Stark decelerator, a traveling-wave decelerator, which has practically no losses. Via computer control of the varying voltages applied to the traveling-wave decelerator, full manipulation of the molecules can be reached; this is shown in experiments in which we decelerate, trap and cool molecules. Finally, in Chapter 6 we are able to create an ultra-cold sample of ammonia molecules that is released from the trap and recaptured after a variable time. In this experiment, it is possible to observe molecules even after more than 10 ms of free expansion. A spectroscopic measurement could be performed during that time, offering interesting prospects for high-resolution spectroscopy and precision tests of fundamental physics theories.

Samenvatting

"Physics is really nothing more than a search for ultimate simplicity, but so far all we have is a kind of elegant messiness."

– Bill Bryson, *A Short History of Nearly Everything*

Naar mijn mening is het de taak van een natuurkundige om dieper in deze elegante wanorde te duiken, en een klein beetje meer orde te brengen, geduldig de puzzle van het heelal te ontwarren totdat het kan worden gevat in enkele simpele principes. Een goede strategie om dit doel te bereiken is om al bekende natuurkundige verschijnselen opnieuw te bestuderen, maar vanuit een nieuwe invalshoek, met hogere nauwkeurigheid en vollediger, zodat informatie wordt verkregen op een nieuw niveau. Hoge resolutie spectroscopie is een effectieve methode toegepast door onderzoeksgroepen overal in de wereld. Het doel is om kennis over de structuur van atomen en moleculen te verkrijgen door hun wisselwerking met licht te bestuderen. Moleculen worden door een lichtveld een laserbundel of microgolf cavity gezonden, en zullen, gedurende de tijd dat het ze zich in het veld bevinden, interactie hebben met het licht. Als de moleculen een hoge snelheid hebben is de interactietijd kort en, als gevolg daarvan, de precisie van het experiment beperkt.

Het onderzoek beschreven in dit proefschrift richt zich op het gebruik van technieken om moleculen af te remmen en hun beweging te controleren met als doel om nauwkeurigere metingen aan moleculen mogelijk te maken. Langzame moleculen zullen een gedurende een langere tijd interactie hebben met het lichtveld waardoor ze nauwkeurig kunnen worden bestudeerd. Op deze wijze kan een zo hoge precisie worden behaald, dat fundamentele natuurkundige theorieën kunnen worden getest. Het voornaamste obstakel om lange interactietijden te verkrijgen is dat de moleculen een eindige temperatuur en snelheidsspreiding hebben waardoor ze zullen uitwaaieren en maar enkele van hen de detector zullen bereiken. Voor een hoge precisie is het nodig om veel moleculen te detecteren. Hiervoor is het nodig om de moleculen tot lage temperatuur te koelen. Helaas kan laserkoeling, een methode die

met veel succes toegepast wordt op atomen, niet effectief worden toegepast op moleculen omdat hun structuur hiervoor te complex is. In dit onderzoek wordt gebruik gemaakt van het zogenaamde *Stark* effect, de interactie van elektrische velden met het elektrische dipoolmoment van moleculen, om moleculen af te remmen en af te koelen.

Het doel van het onderzoek, beschreven in dit proefschrift, is om een zo groot mogelijk signaal van langzame moleculen te genereren zodat ongeëvenaard lange interactietijden verkregen worden. In hoofdstuk 1 wordt in detail het belang van langzame atomen en moleculen voor hoge resolutie spectroscopie besproken en geef ik een samenvatting van onze inspanning om een moleculaire fontein te creëren. In deze fontein bewegen moleculen met een langzame snelheid omhoog, worden vertraagd en vallen uiteindelijk terug door de zwaartekracht. Op deze manier is het mogelijk om interactietijden van typisch een seconde te verkrijgen. Helaas zijn we er niet in geslaagd om moleculen te zien terugvallen, voornamelijk doordat de efficiëntie van conventionele Stark afremmers snel afvalt bij de lage snelheden die nodig zijn. In hoofdstuk 2 wordt een nieuwe detectiemethode voor langzame ammoniak moleculen die gebruikmaakt van VUV laserlicht met een golflengte van 159 nm vergeleken met de "standaard" detectie methode die gebruik maakt van laserlicht bij 322 nm. In hoofdstuk 3 wordt een ionenlens gepresenteerd waarmee we erin zijn geslaagd om ionen afhankelijk van hun snelheid af te beelden op een CCD camera. Op deze manier kunnen wij het signaal van langzame moleculen scheiden van achtergrond signaal van snelle moleculen afkomstig van de niet-afgeremde bundel. In hoofdstukken 4 en 5 wordt een nieuwe Stark afremmer – een lopende golf afremmer – gepresenteerd die in staat is om moleculen vrijwel zonder verlies af te remmen en tot stilstand te brengen. Omdat de benodigde voltages gegenereerd worden door een arbitrary wave generator en vervolgens worden versterkt met HV-versterkers, hebben we complete controle over de vorm en diepte van de potentialen en dus over de afgeremde moleculen. Dit wordt geïllustreerd door metingen waarbij moleculen worden afgeremd, opgesloten en vervolgens afgekoeld. Tenslotte worden in hoofdstuk 6 metingen gepresenteerd aan een ultrakoud wolkje ammoniak moleculen die worden losgelaten uit de val en vervolgens worden teruggevangen na een variabele tijd. In dit experiment zijn wij erin geslaagd om moleculen na meer dan 10 milliseconde vrije vlucht te detecteren. Dit maakt het mogelijk om spectroscopische metingen te doen met een uniek hoge resolutie die het mogelijk maakt om fundamentele natuurkunde theorieën te testen.

Acknowledgments

And, at the end of this thesis, I feel honored to dedicate a little space to be grateful to the people who have been accompanying me during these four years, and some others all my life, helping me make my path through life and science enjoyable and unique.

Y qué menos que empezar por mis padres. Gracias a mis padres, por todo. Mamá, papá; sin vosotros, nada de esto hubiese sido posible. Gracias por traerme al mundo, por educarme con estos valores, y por brindarme un sinfín de oportunidades. Este es el resultado. Os quiero. Also, special thanks to my father for the beautiful watercolor painting of an Alhambra mosaic he made for the cover of this thesis.

Thanks to my brother, brother in the most profound sense of the word. Manuel, Nani, you are my best friend, a companion in life to learn with, to walk along with, to ask for help when I fall, to rise above and stand higher than before. Thanks for being there.

After my family, I want to thank the person who, for some reason, put his eye on me and wanted me here for four years. My dear boss, Rick Bethlem. Rick, thanks for believing in me since the beginning, for your patience and care. Despite our discrepancies about Spanish football players or politics, I have the feeling that we really enjoyed these four years and we had a lot of fun together. I certainly learned a whole lot from a scientist like you.

Julija, the brightest light source of the LaserLab. Thanks for being next to me in the good and the bad times, for your understanding and your kindness. Without you, this experience would not have been the same.

Dear Jonas, dr. Morgenweg, the day I met you I had a great feeling about us, and I wasn't wrong. Since that day I gained a true friend, a listener, a confident, a person whose words always help to put things in perspective. You and your lovely Astrid are by far my favorite Germans.

Thomas Wall, you spiced up my PhD times, and you know what I mean. I must have at least 106 reasons to thank you for. I would highlight so many laughs and fun times (and also, of course, hard work), multiple conversations

in real and invented nederlands, a shared true love for cats... Thanks for popping up, you have been a wonderful gift.

Thanks to Itan for the nice lunches, barbecues, and the many times working on our theses together and playing with your lovely son Jonathan.

Thanks to César for all those nice conversations that made me think and grow, and for that positive vision of life that inspires people.

Thanks to Alan for the support and for the boring task of proof-reading my thesis.

Huge thanks to Jacques Bouma, my Dutch father, the person who has been next to me since I was a young and clumsy master student, and has always been so caring and great to me. You are a great technician and a great friend. I wish you all the best.

Special thanks to Wim Ubachs, for giving me the opportunity of being part of this group, and for his great job as head of the department.

I would also like to thank my companion on the complex task of “mastering the molecular fountain”, Paul Jansen. Even though our big experiment gave us some hard times, we managed to get something great out of it. Thanks for the laughs and for turning the knots that I could not reach.

Also, thanks to many other people of the Atoms and Molecules crew, who contributed to make everyday lab life enjoyable: Ziyu (it was nice to share the lab with you), Remy, Aernout, Adrian, Bob, Robert, Mario, Tjeerd, Steven, Stefan, Kjeld, Wim V., Edcel, Ming Li, Jeroen, Jurriaan, Daniel, Ali, Adonis, Hari and Congseng. Thanks to Marja, for her efficient work and assistance, and Rob Kortekaas, for his efficient technical support. I would also like to thank some former members of the group: Gareth, Toncho, Ofelia, Anne Lisa, Rob van Rooij and Joost, who was of great help for programming issues. I am also grateful to our collaborators from the NKI in Groningen, Steven and Joost, for the construction of the traveling wave decelerator and the nice work together.

Thanks to the several Spanish ladies who appeared at the VU at different times, all of them fun, smart and beautiful. Adorable Patricia, thanks for all the support, and for Azores, which has taken me to so many places, and so many to come. Thanks to María, Alicia and Ingeborg, the cool chemists, for so many good times.

It is important for me to thank some of my people from Granada, my hometown. Ínsaf, you are here with me every single day, despite the distance. I always feel you so close, and I know you will always be here. Diego, Juan, Manu, Rafa, Jordi, Maria, Manu, Víctor, Pepe, Ángel, Mari, María del Mar, Marina, my dear cousins, aunts, uncles, my grandma... and many others, also the ones that are not with us anymore. Thanks so much for making me come back with the biggest smile and new energy every time I visit Spain.

Thanks to my band, The Many Wildes, for giving me the chance and honor of playing with them and learn from such good musicians, and for all the fun and the music. Special thanks to Thijs, for several reasons, among which is his great work on the design of the final look of the cover of this thesis.

Thanks to Doppler and Kaila for the everyday pleasure of their presence.

And thanks to the challenges that life puts in front of us to make us grow, to make us stronger, to make us learn a little bit more about ourselves and the world.